Title of Thesis

Measurment of J/ψ meson and b-hadron
production cross section at $\sqrt{s} = 1.96$ TeV

Date of conferring

2006, January

Tomohiro Yamashita

The Graduate School of

Natural Science and Technology

OKAYAMA UNIVERSITY

Abstract

A new measurement of the inclusive and differential production cross sections of J/ψ mesons and b-hadrons in proton-antiproton collisions at $\sqrt{s} = 1960$ GeV is presented. The data correspond to an integrated luminosity of 39.7 pb^{-1} collected by the CDF Run II detector. The integrated cross section for inclusive J/ψ production for all transverse momenta from 0 to 20 GeV/c in the rapidity range $|y| < 0.6$ is found to be $4.08 \pm 0.02(stat)^{+0.36}_{-0.33}(syst)$ μb. The fraction of J/ψ events from the decay of the long-lived b-hadrons is sperated by using the lifetime distribution in all events with $p_T(J/\psi) > 1.25$ GeV/c. The total cross section for b-hadrons, including both hadrons and anti-hadrons, decaying to J/ψ with transverse momenta greater than 1.25 GeV/c in the rapidity range $|y(J/\psi)| < 0.6$, is found to be $0.330 \pm 0.005(stat)^{+0.036}_{-0.033}(syst)$ μb. Using a Monte Carlo simulation of the decay kinematics of b-hadrons to all final states containing a J/ψ, the first measurement of the total single b-hadron cross section down to zero transverse momentum is extracted at $sqrts$ =1960 GeV. The total single b-hadron cross section integrated over all transverse momenta for b-hadrons in the rapidity range $|y| < 0.6$ is found to be $17.6 \pm 0.4(stat)^{+2.5}_{-2.3}(syst)$ μb.

Contents

List of Figures

List of Tables

Chapter 1

Introduction

1.1   The Standard Model

The standard model is fundamental theory which tell us from what this world is made of, and how they are hold together. In the context of the standard model, all matters are composed from three kinds of elementary particles: leptons, quarks and guage bosons.

There are 6 "flavors" of quarks ,"up(u)", "down(d)", "charm(c)", "strange(s)", "bottom(b)" and "top(t)". They fall into three generations (Table 1.1). Each quarks is assigned a baryon number, $B = 1/3$. Also, each quark is assigned quantum number charmness, strangeness, bottomness and topness. For u and d quarks, $c = s = t = b = 0$, and for c quark, $c = 1$ and $s = t = b = 0$. For s quark, $s = -1$ and $c = t = b = 0$. There are also antiquarks for each 6 flavors, all signs

are reversed.

	flavor	charge	charmness	strangeness	topness	bottomness
1st generation {	u	$+\frac{2}{3}$	0	0	0	0
	d	$-\frac{1}{3}$	0	0	0	0
2nd generation {	c	$+\frac{2}{3}$	1	0	0	0
	s	$-\frac{1}{3}$	0	-1	0	0
3rd generation {	t	$+\frac{2}{3}$	0	0	1	0
	b	$-\frac{1}{3}$	0	0	0	-1

Table 1.1: 6 flavors of quarks. Each quark has fragment charge $+\frac{2}{3}$ or $-\frac{1}{3}$

.

Similar to the quarks, there are six leptons, e, ν_e, μ, ν_{mu}, τ and ν_{tau} (Table 1.1). They fall into three generations. The number of leptons of the same type, L_e for e and ν_e, are conserved in any interaction. There are also six antileptons, all signs are reversed. Because of the conservation of the lepton number, a muon decays as $\mu^+ \rightarrow e^+ \nu_e \bar{\nu}_\mu$, but $\mu^+ \rightarrow e^+ \gamma$ is not allowed.

Besides above leptons and quarks, there are particles which mediate interactions. Unlike leptons and quarks, these particles have spin 1 and called gauge boson. There are 4 interactions and each interaction has its mediate boson. The intermediator for the electromagnetic interaction is the photon. The weak interaction is mediated by 3 bosons $W^\pm$ and Z. The strong interaction is mediated by

		charge	L_e	L_μ	L_τ
1st generation {	e	-1	1	0	0
	ν_e	0	1	0	0
2nd generation {	μ	-1	0	1	0
	ν_μ	0	0	1	0
3rd generation {	τ	-1	0	0	1
	ν_τ	0	0	0	1

Table 1.2: 6 types of leptons. L_e, L_μ and L_τ are electron number, muon number and tauon number, respectively.

8 gluons, and involves only quarks but not leptons. The gravity is mediated by graviton, but the gravity is too weak and not included in the standard model.

Within the electroweak and strong interaction, the quark flavors are conserved, while weak interaction mediated by the $W^\pm$ can change the flavors. That is, a quark can decay into lighter quark plus W, for example $b \rightarrow cW$ where W decay to quark-antiquark pair or lepton and its neutrino.

1.1.1   Strong Interaction

In strong interaction, "color" plays the role of charge. Whereas there one kind of electric charge in electromagnetic interaction (positive or negative), there are three kind of color charges in strong interaction, red, green and blue. Each quark

has one of the three colors and anti quark has anti color charge. The color charge is conserved like electric charge is conserved. Strong interaction works only between quarks, but not with leptons since leptons do not carry color. Strong interaction bind quarks into hadrons, such as proton or pion. Also, force between nucleons is strong force, and strong interaction is responsible for binding protons and neutrons into a nucleus.
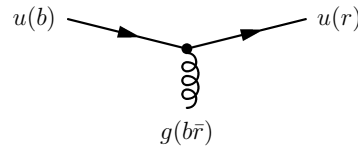
Figure 1.1: Primitive vertex of quark plus gluon.

Quarks interact each other by exchanging the gluons. A primitive vertex of Feynman diagram is depicted in Fig. 1.1. The strength of the interaction is represented by a strong coupling constant α_s. In the figure, a blue up quark converted into a red up quark. The color of the quark may change while the flavor of the quark stay unchanged. Because the color is conserved, the gluon involved must have carry the color ($b\bar{r}$ in Fig. 1.1). Gluons carry one color and one anti color, and there are 8 gluons. Force between quarks is described by combining the primitive vertices, for example Fig. 1.2. Since the gluons themselves carry the color unlike the photon in electromagnetic interaction, they couple each other and there are other primitive vertices shown in Fig 1.3. This leads to anti-screening, and

4
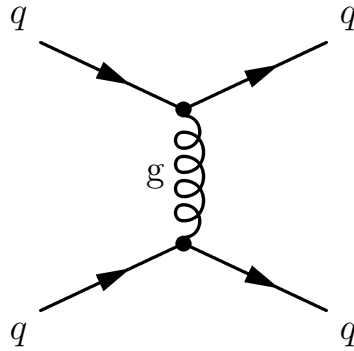
Figure 1.2: Quarks interact each other by exchanging a gluon.
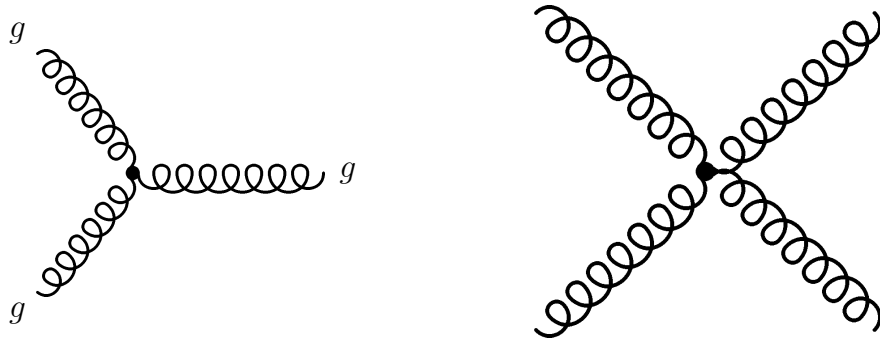
Figure 1.3: Gluons coupling themselves.

confinement of quarks into hadrons. The quark probed at long distance has more color charge by cloud of gluons and bigger α_s, while quark probed at small distance has less color charge by cloud of gluons and smaller α_s. This weaking of strong coupling constant is called "asymptotic freedom".

1.1.2 Quark Production Cross Section

Factorization theorem [16] allows to calculate quark production cross section in $p\bar{p}$ collisions, and b-hadron production cross section can be schematically described as

$$\frac{\sigma(p\bar{p} \to H_b X)}{dp_T(H_b)} = f^{p,\bar{p}} \otimes \frac{\sigma(qq/gg/qg \to bX)}{dp_T(b)} \otimes D^{b \to H_b}, \qquad (1.1)$$

where $f^{p,\bar{p}}$ denotes proton structure, $\sigma(qq/gg/qg \to bX)/dp_T(b)$ denotes patoronic cross section which is calculable in terms of perturbative QCD, and $D^{b \to H_b}$ denotes fragmentation of b quark to b-hadron, respectively. In Fig. 1.4, example of Feynman diagrams involved in patoronic cross section calculation at Leading Order (LO), are shown. At Next-to-Leading Order calculation (NLO), in addition
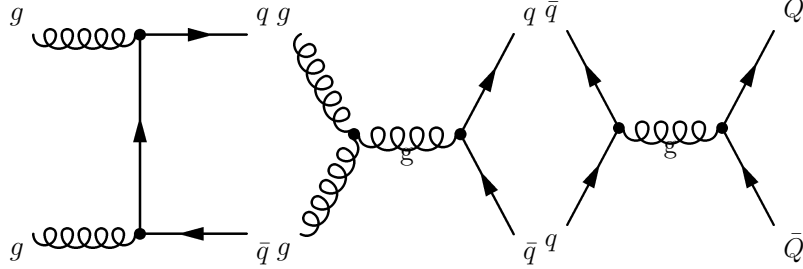
Figure 1.4: Feynman diagrams for $q\bar{q}$ production at Leading Order.

to the LO diagrams, real gluon radiation, virtual gluon exchange and gluon splitting diagrams are involved. The example of NLO diagrams are shown in Fig. 1.5.
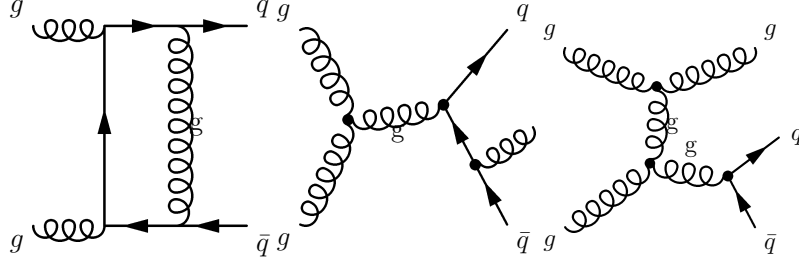
Figure 1.5: Feynman diagrams for $q\bar{q}$ production at Next-to-Leading Order.

1.2 History

The b cross section measurements in hadron collider was started by UA1 experiment at the $S\bar{p}pS(\sqrt{S} = 630$ GeV) collider [17, 18]. Their result was in good agreement with next-to-leading order (NLO) QCD calculations [4, 8, 19].

In 1992, CDF Run I reported exclusive B-meson cross section through the decay chain $B^{\pm} \rightarrow J/\psi K^{\pm}$ [20]. The results were

$$\sigma(p\bar{p} \rightarrow B^- X; p_T > 9.0\text{GeV}/c, |y| < 1.0)$$

$$= 2.8 \pm 0.9(\text{stat}) \pm 1.1(\text{syst})\mu\text{b}, \tag{1.2}$$

and b-quark cross section was

$$\sigma(p\bar{p} \rightarrow bX; p_T > 11.5\text{GeV}/c, |y| < 1.0)$$

$$= 6.1 \pm 1.9 \pm 2.4\mu\text{b}, \tag{1.3}$$

while the theory prediction of b-quark cross section is [4, 19]

$$\sigma(p\bar{p} \rightarrow bX; p_T > 11.5\text{GeV}/c, |y| < 1.0) = 1.1^{+0.5}_{-0.4}\mu\text{b}. \tag{1.4}$$

The ratio of the measurement to the theory is factor of 6 and this was as a surpprising result, although the error on the measurement was big. Later, CDF published *b*-quark cross section measurement from inclusive $J\psi$, $\psi(2S)$ [3] and inclusive leptons [1, 2]. The results are shown Fig. 1.6. The results were constantly higher than prediction. CDF measured *b*-quark cross section in exclusive decay mode $\bar{B}^0 \rightarrow J/\psi \bar{K}^{*0}(892)$ [21] and reported the cross section

$$\sigma(p\bar{p} \rightarrow bX; p_T > 11.5 \text{GeV}/c, |y| < 1.0)$$

$$= 3.7 \pm 1.6(\text{stat}) \pm 1.5(\text{syst})\mu\text{b}. \tag{1.5}$$

The result was lower than previous *b*-quark cross section measurement in exclusive decay mode [20] but higher than the prediction [4,19]. In 1995, CDF reported the measurement of differential *B* meson cross section in exclusive decay mode $B^+ \rightarrow J/\psi K^+$ and $B^0 \rightarrow J/\psi K^{*0}(892)$ with 19.3 ± 0.7 pb^{-1} of data [5]. The result is shown in Fig. 1.7 and the results are higher than the prediction. In 2001, CDF reported another differential *B* meson cross section measurement in exclusive decay mode $B^+ \rightarrow J/\psi K^+$ with increased data of 98.4 ± 4 pb^{-1} [7], and the result is shown in Fig. 1.8. The measurement was still higher than the theoritical prediction.

From the Tevatron, D0 experiment also published the measurements of *b* cross section [11, 22–25]. Their results were also higher than the prediction as shown in Fig. 1.9. The result [24] of the measurement of *b* production at large rapidity showed larger disagreement than central region between the measurement and the

theory as shown in Fig.1.10.

Several theoretical explanations were suggested: higher-order corrections are large, intrinsic k_T effects are large [26], extreme values of the renormalization scales are needed, or new methods of resummation and fragmentation are required [12, 13, 27, 27]. Theories of new and exotic sources of b-hadrons have also been proposed [28]. Although, new calculation method FONLL [12, 13] showed decreased discrepancy between theory prediction and CDF Run I as shown in Fig. 1.11, the problem is not yet solved, also affected the earlier Tevatron experiments covers only a part of the inclusive p_T spectrum.

An inclusive measurement of b-hadron production over all transverse momenta can help resolve this problem. Bottom hadrons have long lifetimes, on the order of picoseconds [29], which correspond to flight distances of several hundred microns at CDF. The measured distance between the J/ψ decay point and the beamline is used to separate prompt production of charmonium from b-hadron decays. The b-hadron cross section is then extracted from the measurement of the cross section of J/ψ mesons from long-lived b-hadrons. In this paper, the first measurement of the inclusive b-hadron cross section at $\sqrt{s} = 1960$ GeV measured over all transverse momenta in the rapidity range $|y| < 0.6$ is presented.
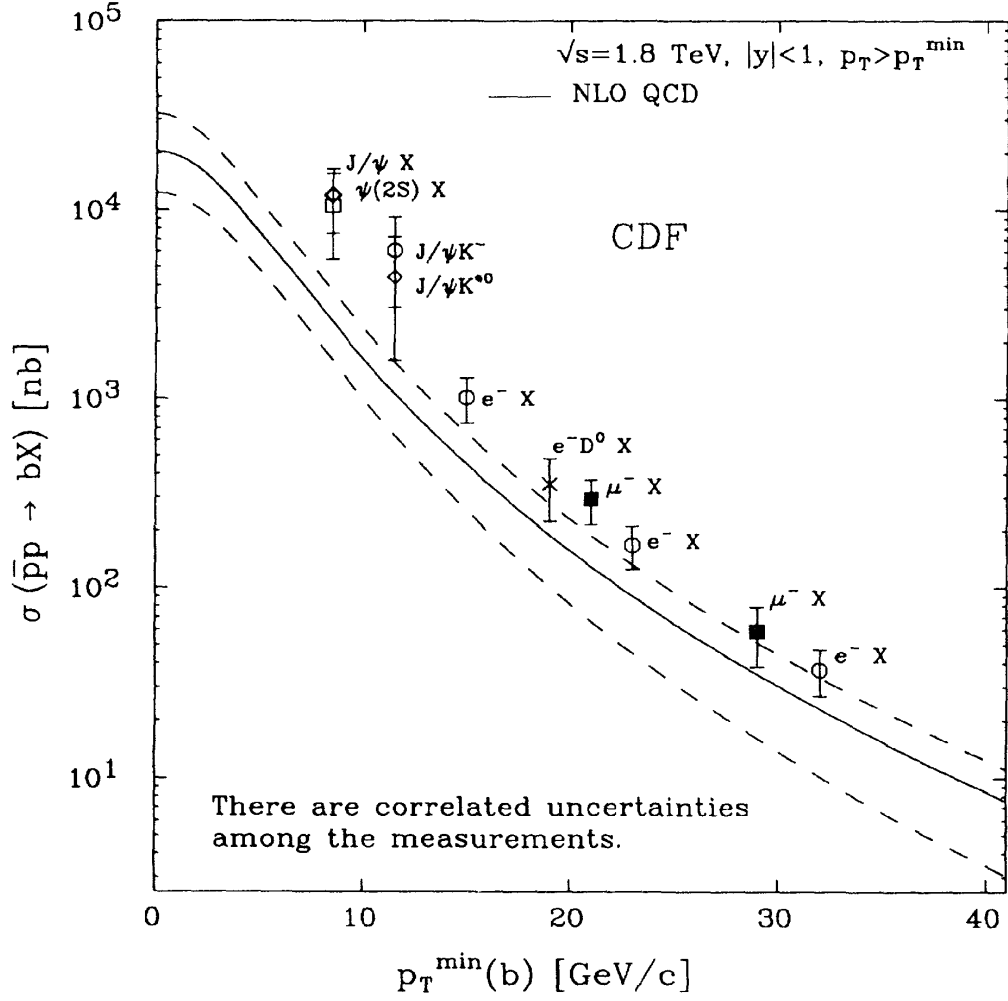
Figure 1.6: CDF Run I results of *b*-quark cross section by inclusive leptons [1, 2] and, inclusive ψ and ψ' [3], together with comparison to the prediction of NLO QCD calculation [4]. Dashed lines indicate the uncertainties in the prediction. Measured cross sections are higher than the prediction, though still consistent within the uncertainties.
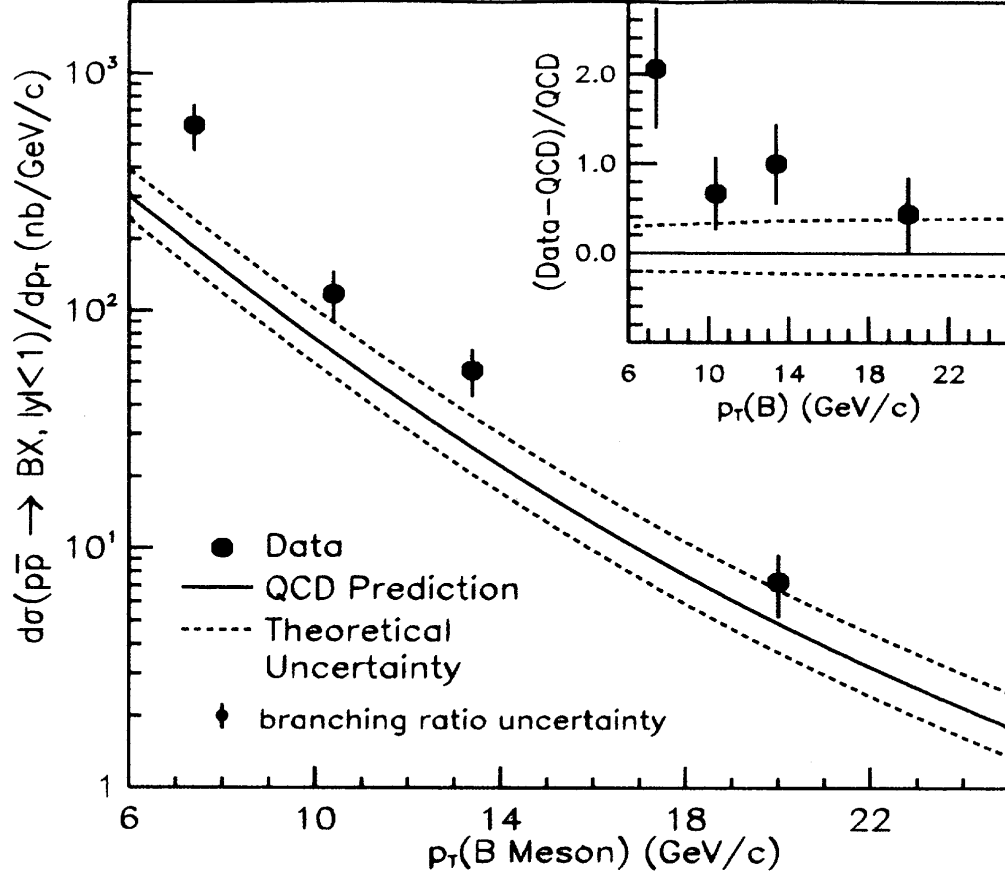
Figure 1.7: *B* meson differential cross section measured by CDF Run I [5] using 19.3 ± 0.7 pb^{-1} of data, with comparison to NLO QCD [4, 6] based Monte Carlo simluation. Dashed lines indicate the uncertainties in the prediction. Measured cross section is again higher than the prediction, though still consistent within the uncertainties.
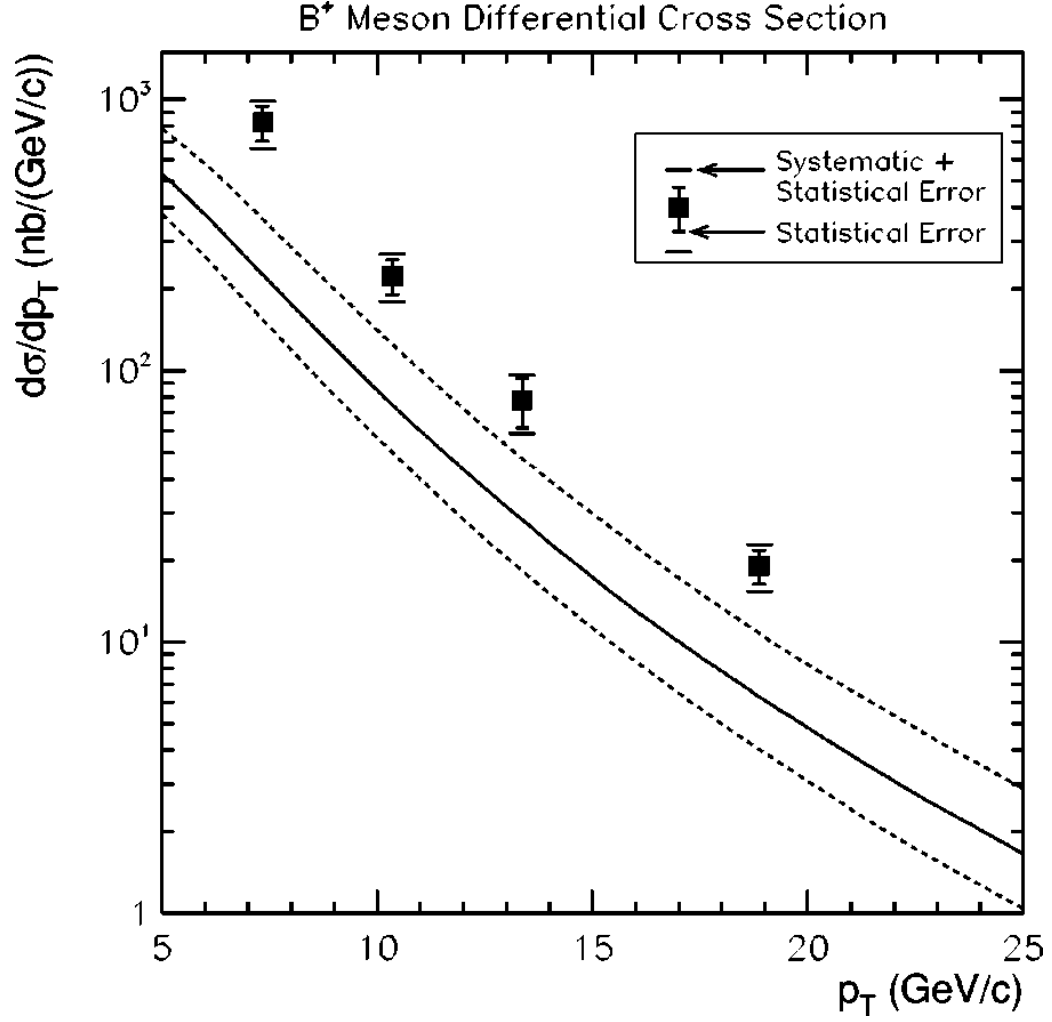
Figure 1.8: B^+ meson differential cross section measured by CDF Run I [7] using 98.4 ± 4 pb^{-1} of data, with NLO QCD calculation [4, 8] using the MRST parton density function [9, 10, 10]. Data points are constantly higher than the prediction.
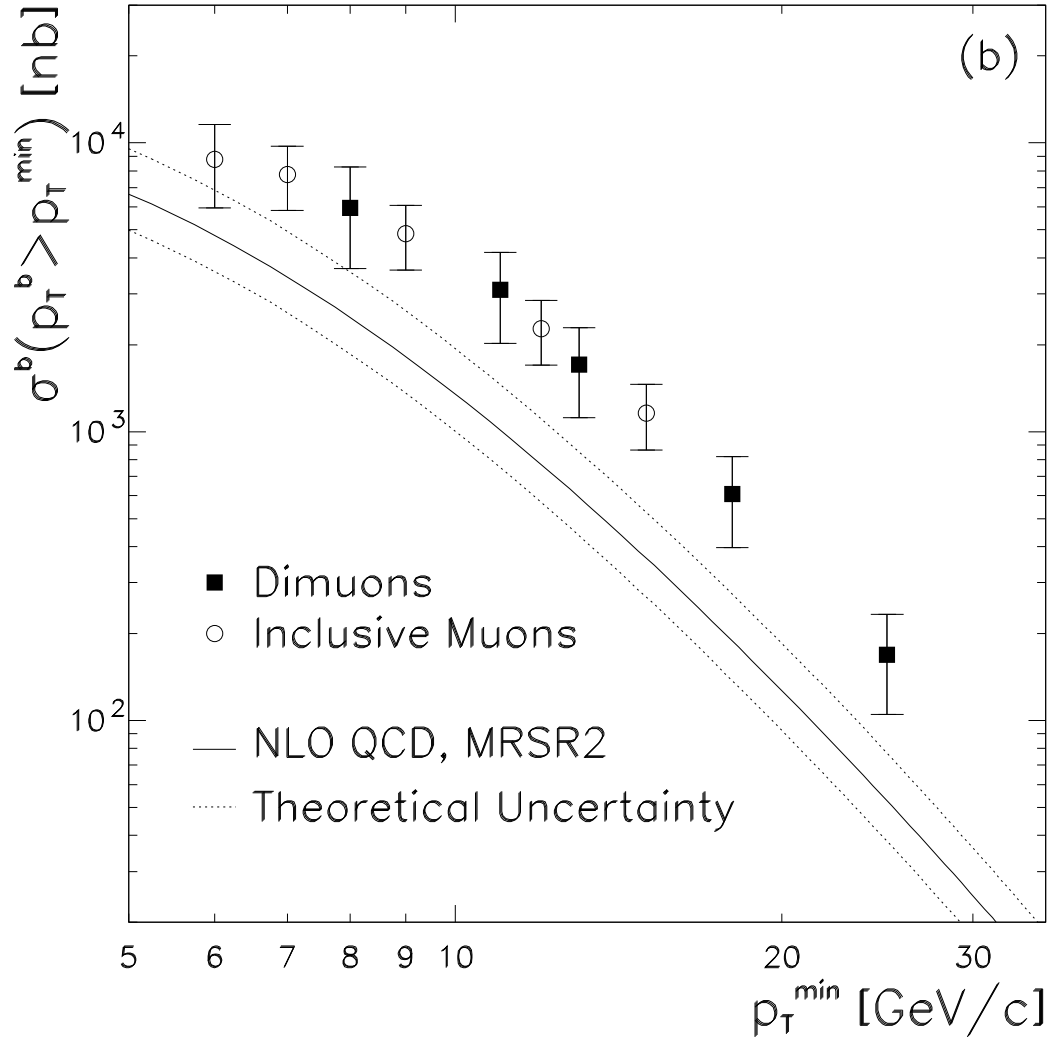
Figure 1.9: *b* quark production cross section measured by D0 [11] measured by D0, with comparison to the NLO QCD prediction computed using Ref. [6].
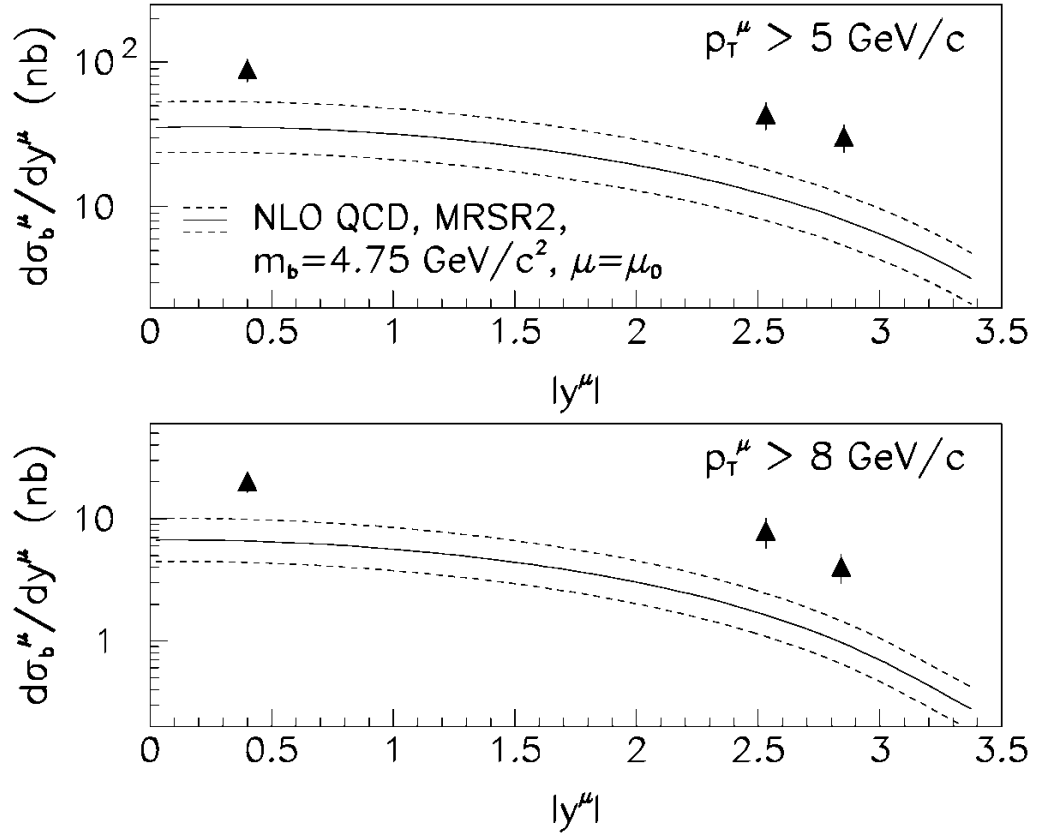
Figure 1.10: The cross section of muons from b quark decay as a function of $|y^\mu|$ measured by D0, with NLO QCD prediction.
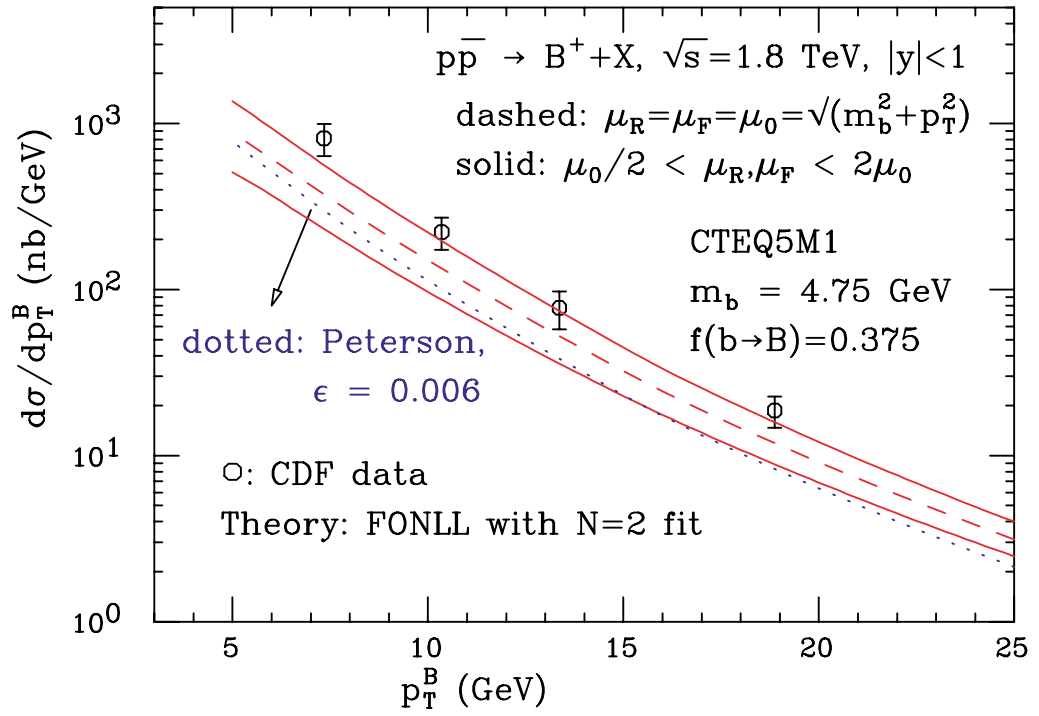
Figure 1.11: Prediction by FONLL [12] with comparison to CDF Run I measurement [7].

Chapter 2

The experimental apparatus

The data used for this analysis is collected by the CDF (Collier Detector at Fermilab), located in the Fermilab. The CDF is a general purpose detector to study events of collisions of proton-antiproton accelerated by the Tevatron. The Tevatron is highest-energy proton-antiproton accelerator in the world. Besides the CDF, the Tevatron has another collision point and the data is collected and analyzed by the D0 experiment.

Both the accelerator and the detector are undergone major upgrades between 1997 and 2001. The energy in the cms is increased to 1.96 TeV, instantaneous luminosity is increased and number of bunches is increased to 36 which correspond to 396 ns crossings. The CDF must accomplish maximum response time shorter than that for dead-time-less data acquisition. In the following sections, more detailed description of the accelerator and the detector is given.

2.1 Acceleration and creation of proton and antiproton

At two interaction points B0 and D0 of the Tevatron, a beam of 980 GeV protons collides head-on with a beam of 980 GeV antiprotons. Acceleration of the proton and antiproton beams need five steps, and show in Fig. 2.1.

2.1.1 Proton

At first, a beam of proton begins as H^- ions produced in a magnetron. Then, the ions are accelerated to 750 keV by Cockcroft-Walton [30] accelerator, which is a two legs capacitor-diode voltage multiplier.

Next, the ions are sent to a linear accelerator (Linac), and accelerated from 750 keV kinetic energy to 400 MeV. The acceleration in the Linac is done by a series of RF cavities. Because of the oscillating electric field, the ions become grouped into bunches.

Next, the ions are injected into the Booster, which is a circular proton synchrotron of 151 m in diameter. At injection, a carbon foil strips the electrons from the H$^-$ ions, leaving only protons. It accelerates 400 MeV protons obtained from the Linac to 8 GeV. This is done by a series of electromagnetic kicks applied by RF cavities, about 500 keV per turn.

Next, the protons are transferred to the Main Injector and accelerated to 150

GeV for injection into the Tevatron, or 120 GeV for use in antiproton production. The Main Injector is a part of upgrade to the Run II accelerator complex, and is capable of higher proton currents than its predecessor, Main Ring. The higher proton currents results in a higher rate of antiproton production.

2.1.2 Antiproton

To create antiprotons the protons of 120 GeV extracted from Main Injector are used. The protons are directed into a nickel target and create a spray of particles which contains antiprotons. The spray contains 20 antiprotons on average per million protons, and the antiprotons have mean energy of about 8 GeV. The antiprotons are focused by a cylindrical lithium lens, and other particles in the spray are separated.

Then, the antiprotons are directed to the Debuncher synchrotron. The antiprotons must be cooled for the later acceleration and collision. The cooling is done by the Debuncher synchrotron at first. Next, the antiprotons are transferred to the 8 GeV Accumulator synchrotron and further cooled, and stored. When enough antiprotons are circulating in the Accumulator, 36 bunches of antiprotons are transferred back into the Main Injector for a new store, and accelerated together with 36 bunches of protons. Then transffered to the Tevatron, for the final acceleration stage of Fermilab accelerator complex. Antiproton availability is the most limiting factor for attaining high luminosities.

2.1.3 Tevatron

The Tevatron is a superconducting synchrotron of radius approximately 1 km, and has 8 acceleration cavities. It receives 150 GeV protons and antiprotons from Main Injector, and accelerates them to 980 GeV. The protons and antiprotons circle the Tevatron in opposite directions. In Run II the Tevatron operates with a 36 on 36 bunch structure (protons on antiprotons) with 396 ns spacing between bunches, compared with 3.5 μs in the Run I 6 bunch mode. The beams are brought to two collision points B0 and D0, for the CDF and D0 experiments.

The Luminosity can be expressed as:

$$L = \frac{fBN_pN_{\bar{p}}}{2\pi(\sigma_p^2 + \sigma_{\bar{p}}^2)}F(\frac{\sigma_l}{\beta^*}),
\qquad (2.1)$$

where, f is the revolution frequency, B is the number of bunches, $N_{p/\bar{p}}$ are the number of protons/antiprotons per bunch, and $\sigma_{p/\bar{p}}$ are the rms beam sizes at the interaction point. F is a form factor which depends on the ratio of σ_l, the bunch length, to β^*, the beta function, at the interaction point. The beta function is a measure of the beam width, and is proportional to the beam's x and y extent in phase space. Antiproton availability is the most limiting factor for attaining high luminosities [31].

19

2.2 CDF

The Collider Detector at Fermilab (CDF) is a multi purpose detector designed to study $p\bar{p}$ events at CMS energy of $\sqrt{s}$ = 1.96 TeV. The design of the detector is not specialized for one particular physics goal, but rather for many variety of topics. An elevation view of the CDF detector is shown in Fig. 2.2.

CDF can be separated into sub detector systems as follows. The innermost system is the tracking system. It has a cylindrical shape and is concentric with the beam. It detects charged particle, and provides momentum and vertex information of the particle. One quarter of the tracking system is shown in Fig. 2.3. The detectors closest to the interaction point are the silicon detectors. It consists of 3 detectors, and its innermost detector is Layer 00 which is mounted on the beam pipe. It's followed by the five layers silicon sensonrs, Silicon Vertex Detector (SVX II). Outermost silicon detector is Intermediate Silicon Layers (ISL), which covers larger rapidity than SVX II. Outside the silicon detectors, the Central Outer Tracker (COT) is placed.

The tracking system is surrounded by the Time of Flight (TOF) system. Its purpose is identification of low momentum charged particles.

Both the tracking system and TOF are inside a superconducting solenoid which provides 1.4 T magnetic field parallel to the beam.

Outside the solenoid there are calorimetry systems which are segmented in ϕ and η. Each segmented "tower" points the interaction region, and has an elec-

tromagnetic calorimeter followed by a hadron calorimeter. The electromagnetic calorimeters are separated in η into CEM (central ElectroMagnetic), PEM (plug) and FEM (forward). The hadron calorimeters in the central region are CHA (central) and WHA (endwall). The plug and forward region are PHA (plug) and FHA (forward).

Outermost system is muon identification systems. It consists of 3 parts, central muon system (CMU), central muon upgrade (CMP), central muon extension (CMX) and Intermediate Muon Detector (IMU). IMU is not used in this analysis.

2.2.1 Cordinate system

Since CDF has approximately cylindrical shape, the origin of the coordinate system is set to the center of the detector, and the z direction is defined to be along the direction of the protons. The y axis is set to be upward. The x axis is also defined by this, because the right handed coordinate system is used. The polar angle θ is measured from positive z direction, and the azimuthal angle is measured around the z axis. The pseudorapidity η is often used instead of the *theta*, and defined as

$$\eta = -\ln\tan(\frac{\theta}{2}).\qquad(2.2)$$

Fig. 2.4 show the definition of the coordinate system.

2.2.2 Tracking system

Since the solenoid provides uniform magnetic field along z axis, trajectory of the charged particles from $p\bar{p}$ interaction form the helices, and called tracks. At CDF, 5 parameters are used to describe the track: impact parameter d_0, z_0, ϕ_0, half curvature C and $\lambda = \cot\theta$. From the half curvature, the transverse momentum p_T is calculated as

$$p_T = (B/2cC), \tag{2.3}$$

where B is the magnitude of the magnetic field and c is the speed of light. The sign of the curvature is the charge of the particle. From $\cot\theta$, p_z is calculated as

$$p_z = p_T \times \cot\theta. \tag{2.4}$$

ϕ_0 is the direction at the point of closest approach of the track to the origin. z_0 is the z position of the point of closest approach of the track to the origin. The absolute value of the impact parameter d_0 is the distance of closest approach of the track to the origin in $r - \phi$ plane. The sign of d_0 is defined by following,

$$\hat{z} \cdot (\hat{d}_0 \times \hat{p}_T), \tag{2.5}$$

where $\hat{z}$, $\hat{d}_0$ and $\hat{p}_T$ are the unit vectors in the direction of the z axis, d_0 and p_T.

COT

The COT, Central Outer Tracker plays main role in CDF tracking system.

It's a cylindrical open cell drift chamber, and its active volume is 310 cm long in z, and from 40 cm to 137 cm in radius. The COT has 96 sense wire layers which are grouped into 8 "superlayers" as shown in Fig. 2.5. Each superlayer is divided in ϕ into "supercells", and each supercell has 12 sense wires. Fig. 2.6 shows the geometry of the 3 supercells for superlayer 2. As shown in Fig. 2.6, each supercell consist of sense and potential wires, and cathode field panel. 1.6 mil gold-plated tungsten wire is used for both sense and potential wire. The field panel is gold on a 0.25 mil thick Mylar sheet. The superlayers alternate between stereo (the wires are tilted $\pm 3°$ with respect to the z axis) and axial (the wires are parallel to the z axis), and superlayer 1 is stereo layer. The super cell is tilted by $35°$ with respect to the radial direction. This is because the electrons drift with a Lorentz angle of $\approx 35°$ due to the solenoidal magnetic field. The COT is filled with an Argon-Ethane-CF4(50:35:15) gas mixture.

Silicon detectors

CDF has three silicon detectors and they are from innermost, Layer 00 (L00), the Silicon Vertex Detector (SVX II) and the Intermediate Silicon Layers (ISL). Fig. 2.7 and 2.8 show the end view and the side view of the silicon detectors, respectively.

Silicon sensors of SVX II are microstrip detectors of either single or double-sided. The single-sided sensors provide only ϕ information, and double-

sided sensors provide both ϕ and z. On ϕ measurement side, the p-type strips are axially implanted near the surface of lightly doped n-type bulk, and the readout pitch is 60 to 65 mum depending on the layer. On the z side, n$^+$ strips are implanted with either 90° or small stereo angle of 1.2° with respect to the axial strips. Four silicon sensors assemble a "ladder" which is 29 cm long. Readout electronics are mounted on each ends of the ladders. The ladders are arranged in an approximately cylindrical configuration, which is called "barrel". A barrel is segmented into 12 wedges in $r - \phi$, and each wedge contains 5 layers. SVX II is built from 3 barrels adjacent to each other along the z axis.

Innermost detector L00 is mounted on the beam pipe, consist of single-sided sensors and provides only ϕ measurements. ISL consists of small stereo angle double-sided silicon sensors similar to SVX II. ISL covers $|\eta| \leq 2.0$.

Table 2.1 shows design parameters of the COT and SVX II.

2.2.3 Muon identification

The muon identification systems are located behind the calorimetry systems, which serve as absorbers for particle which are not muon. Most of particles which penetrate the calorimetry systems are muons. Pions and Kaons which reach the muon systems are source of background and called "punch through".

COT	
Number of superlayers	8
Measurements per superlayer	12
Stereo Angle	+3 0 -3 +3 0 -3 0°
Cell/Layer	168 192 240 288 336 384 432 480
Radius at Cener of SL	46 58 70 82 94 106 119 131 cm
Tilt Angle	35°
Length of Active Region	310 cm
Number of channels	30,240
Material thickness	1.3%X_0

SVX II	
Readout coordinates	$r - \phi$; $r - z$
Number of barrels	3
Number of layers per barrel	5
Number of wedges per barrel	12
Ladder length	29.0 cm
Combined barrel length	87.0 cm
Radius at axial layers	2.545 4.120 6.520 8.220 10.095 cm
Radius at stereo layers	2.995 4.570 7.020 8.720 10.645 cm
number of ϕ strips	256 384 640 768 896
number of Z strips	256 576 640 512 896
ϕ strip pitch	60 62 60 60 65 μm
Z strip pitch	141 125.5 60 141 65 μm
Cell/Layer	168 192 240 288 336 384 432 480
Number of channels	405,504
Material thickness	3.5%X_0

Table 2.1: Design parameters of the tracking system.

CMU The CMU is located in the central calorimeter at a radius of 347 cm, and covers $|\eta| < 0.6$. Fig. 2.9 shows the location of the CMU. CMU is segmented into wedges in ϕ. As shown in the figure, since each tower of the calorimeter has $15°$ in ϕ and the CMU wedge has $12.6°$, there is a gap of $2.4°$ between wedges. There are three modules in each wedge, and each module consists of 4 layers of 4 rectangular single-wire drift cells as shown in Fig. 2.10. A unit called "stack" is formed from 4 drift cells, one cell from each layer. From a pair of adjacent stacks, a tower is formed. Each cell is 6.35 cm $\times 2.68$ cm, and 226 cm long in z and parallel to z axis.

CMP The CMP is located behind an additional 60 cm of steel which purpose is to reduce the background by punch through, and its coverage is also $|\eta| < 0.6$. The drift cells are similar to CMU but its dimension is 2.5 cm $\times 15$ cm and typically 640 cm long in z, with some shorter sections on the bottom of the detector to avoid obstructions. A layer of scintillation counters (CSP) is also installed on outside the surface of the CMP.

CMX The CMX covers $0.6 < |\eta| < 1.0$. It consists of conical sections of drift tubes (CMX) and scintillation counters (CSX). There is a $30°$ gap of the azimuthal coverage of CMX/CSX. The dimension of its drift cell is different with CMP only in z and is 180 cm long.

Table 2.2 shows design parameters of the central muon detectors, and Fig. 2.11 shows the coverage of the three detectors.

From the timing information of the drift cells in a module, short tracks called "stubs" are reconstructed. If a stub is matched to an extrapolated track reconstructed in the COT, a muon is reconstructed in the CDF. To estimate the track-stub match, χ_ϕ^2 of the match is computed based on the distance between the track and stub, the difference in direction of the track and stub, and the covariance matrix of the track.

2.2.4 Triggering

At a hadron collier, particularly the Tevatron, it is impossible to record all the collisions since the collision rate is much higher than the rate at data can be recorded. And only the interesting events which occupy only small part of all the collisions are recorded. Hence, the trigger system plays important role in CDF. There are three trigger levels in CDF, they are simply referred as Level 1, Level 2 and Level 3. Each trigger level reduces the size of data, and subsequent level uses more complicated information and takes more time. Collision rate is roughly 2.5 MHz, and acceptable rates at each level are kHz, 300 Hz and 30-50 Hz, respectively. The block diagram for the Run II trigger system is presented in Fig. 2.12.

Level 1

The Level 1 trigger uses custom designed hardware to find physics objects.

	CMU	CMP/CSP	CMX/CSX	IMU
Pseudo-rapidity coverage	$|\eta| \leq \sim 0.6$	$|\eta| \leq \sim 0.6$	$\sim 0.6 \leq |\eta| \leq \sim 1.0$	$\sim 1.0 \leq |\eta| \leq \sim 1.5$
Drift tubes:				
thickness	2.68 cm	2.5 cm	2.5 cm	2.5 cm
width	6.35 cm	15 cm	15 cm	8.4 cm
length	226 cm	640 cm	180 cm	363 cm
Max drift time	800 ns	1.4 μs	1.4 μs	800 ns
Total drift tubes	2304	1076	2208	1728
Scintillators:				
thickness		2.5 cm	1.5 cm	2.5 cm
width		30 cm	30 40 cm	17 cm
length		320 cm	180 cm	180 cm
Total counters		269	324	864
Pion interaction lengths	5.5λ	7.8λ	6.2λ	6.2 - 20λ
Min. muon p_T	1.4 GeV	2.2 GeV 1.4 GeV	1.4 - 2.0 GeV	
Multiple scattering res.	12 cm/p (GeV/p)	15 cm/p (GeV/p)	13 cm/p (GeV/p)	13 - 25 cm/p (GeV/p)

Table 2.2: Design parameters of the CDF II Muon Detectors. Pion interaction lengths and multiple scattering are computed at a reference angle of $\theta = 90°$ in CMU and CMP/CSP, at an angle of $\theta = 55°$ in CMX/CSX, and show the range of values for the IMU.

The hardware consists of three parallel synchronous processing streams which feed inputs of the single Global Level-1 decision unit. One stream finds calorimeter based objects, another finds muons while the third finds tracks in the COT. An eXtremely Fast Tracker (XFT) is used at Level-1, to reconstruct tracks in $r - \phi$ plane to be used at this level. An extrapolation unit (XTRP) matches a track to an electromagnetic calorimeter energy cluster for electron identification or to a stub in the muon system for muon identification.

Level 2

The Level 2 trigger uses custom hardware to do a limited event reconstruction which can be processed in programmable processors. The Level 2 trigger consists of several asynchronous subsystems which provide input data to programmable Level 2 Processors in the Global Level2 crate. The $r - \phi$ information from the silicon detector are used at this level.

Level 3

The Level 3 trigger is a farm of about 200 Linux PCs. There complete events are built and more sophisticated algorithms classify events. Events passing the Level-3 trigger criteria are sent to mass storage or online monitoring processes by the Data Logger system.

2.2.5 Luminosity

Luminosity is measured by Cerenkov Luminosity Counters (CLC) [32–34] which are located inside 3 degree holes inside the endplug calorimeters in the forward and backward region. The rate of inelastic $p\bar{p}$ interactions is given by

$$\mu \cdot f_{\text{BC}} = \sigma_{\text{in}} \cdot L, \qquad (2.6)$$

where L is the instantaneous luminosity, μ is the average number of inelastic $p\bar{p}$ interactions per bunch crossing, and f_{BC} is the rate of bunch crossings. The number of $p\bar{p}$ interactions in a bunch crossing follows Poisson statistics where the probability of empty crossings is given by $P_0(\mu) = e^{-\mu}$. An empty crossing is observed when there are fewer than two counters with signals above threshold in either module of the CLC. The measured fraction of empty bunch crossings is corrected for the CLC acceptance and the value of μ is calculated. The measured value of μ is combined with the inelastic $p\bar{p}$ cross section to determine the instantaneous luminosity using Equation 2.6. Because this method depends only weakly on the CLC thresholds, it functions particularly well at low luminosities where the probability of empty bunch crossings is large. The systematic error on the luminosity measurement is estimated to be 6%. In CDF Run II, only runs with greater than 10 nb^{-1} integrated luminosity are considered for analysis. Runs with good operating conditions in the detector are tagged by the online shift crews. Data from those runs are examined to exclude ones with COT, muon or trigger hard-

ware problems. For this analysis, the data collected from February to July 2002 was used. This sample corresponds to a total integrated luminosity of 39.7 ± 2.3 pb^{-1}. For J/ψ candidates with transverse momenta in the range 0 to 2 GeV/c, we use 14.8 ± 0.9 pb^{-1} of our data sample, which corresponds to that fraction of the data collected when no cut on the di-muon opening angle in the Level 3 trigger was used.
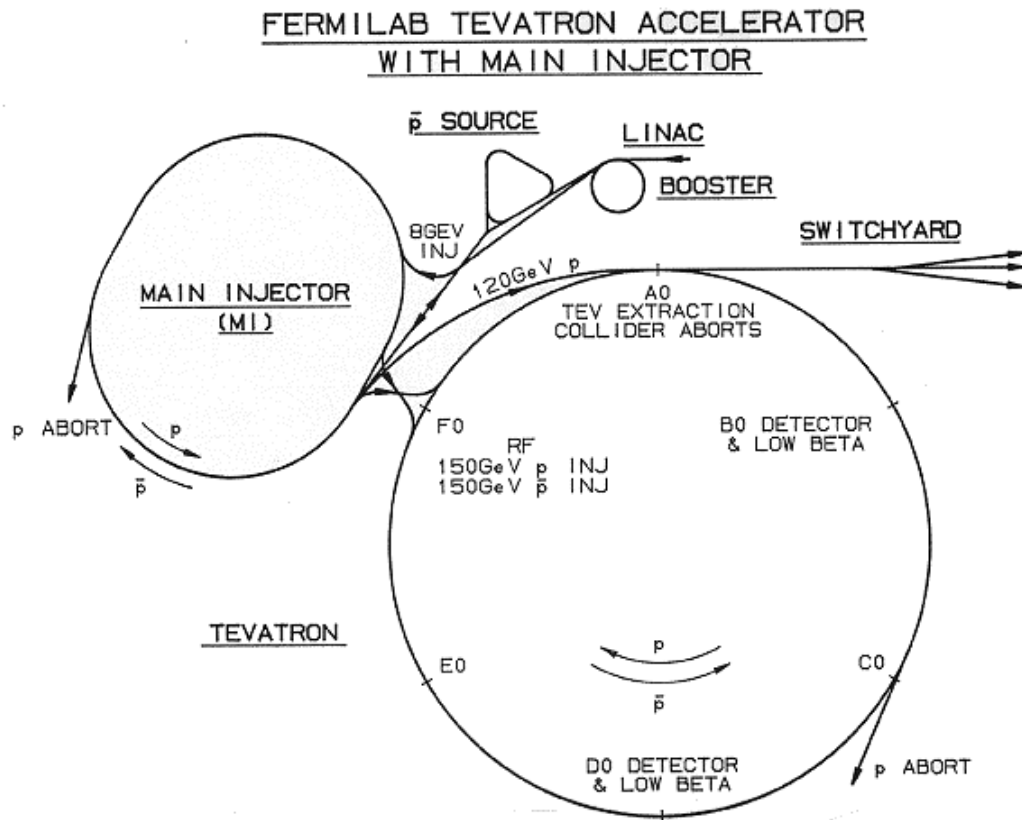
Figure 2.1: A schematic view of the Run II Tevatron accelerator complex at Fermilab. The new Main Injector is shown in the left side of the Tevatron Ring. The CDF detector is located at one of the collision points at B0 on the Tevatron Ring.

CENTRAL DRIFT CHAMBER

ELECTROMAGNETIC
CALORIMETER

EM SHOWER
MAXIMUM CHAMBER

HADRONIC CALORIMETER

MUON DRIFT CHAMBERS

STEEL SHIELDING

MUON SCINTILLATOR
COUNTER

ISL (3 LAYERS)

SVX II (3 BARRELS)

INTERACTION POINT (B0)

SOLENOID COIL

PRESHOWER DETECTOR

SHOWERMAX DETECTOR

EL - 745 FT.

UPPER NOTCH STEEL

END
PLUG
PMT
BOX

END
PLUG
PMT
BOX

Q4

EL - 706 FT.

0	1m	2m	3m	4m	5m
0	2	4	6	8	10	12	14	16	ft.

Figure 2.2: Elevation view of the CDF II detector.

CDF Tracking Volume
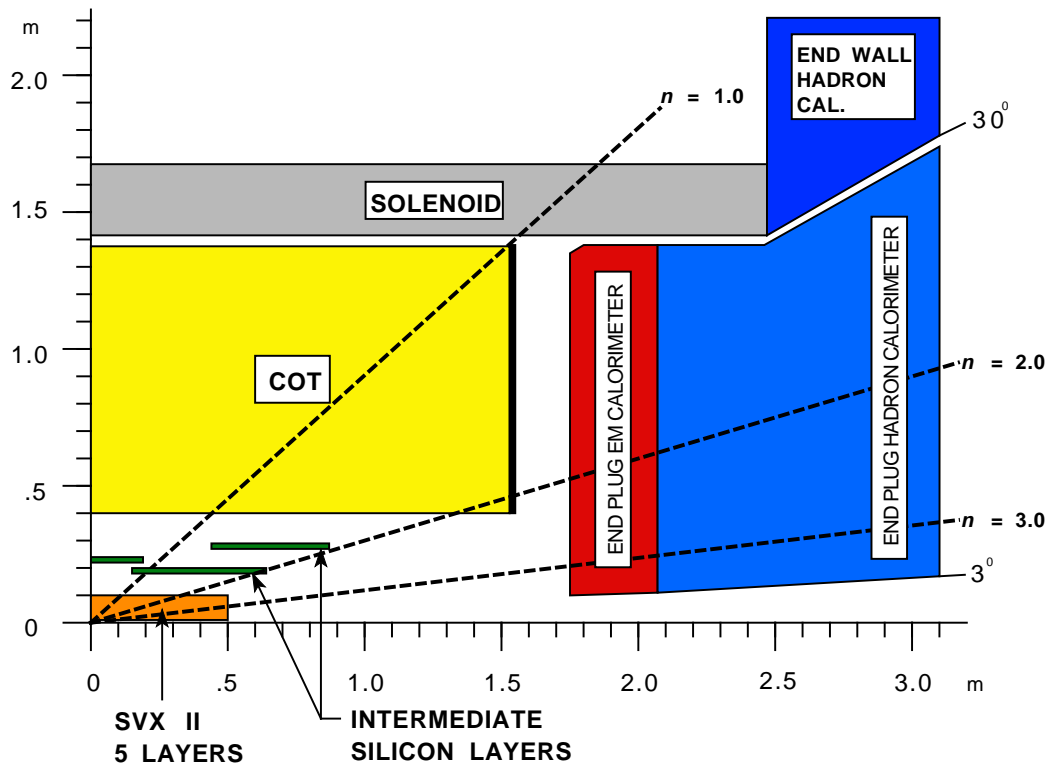
Figure 2.3: A cut-away view of one quadrant of the CDF Tracking Volume.
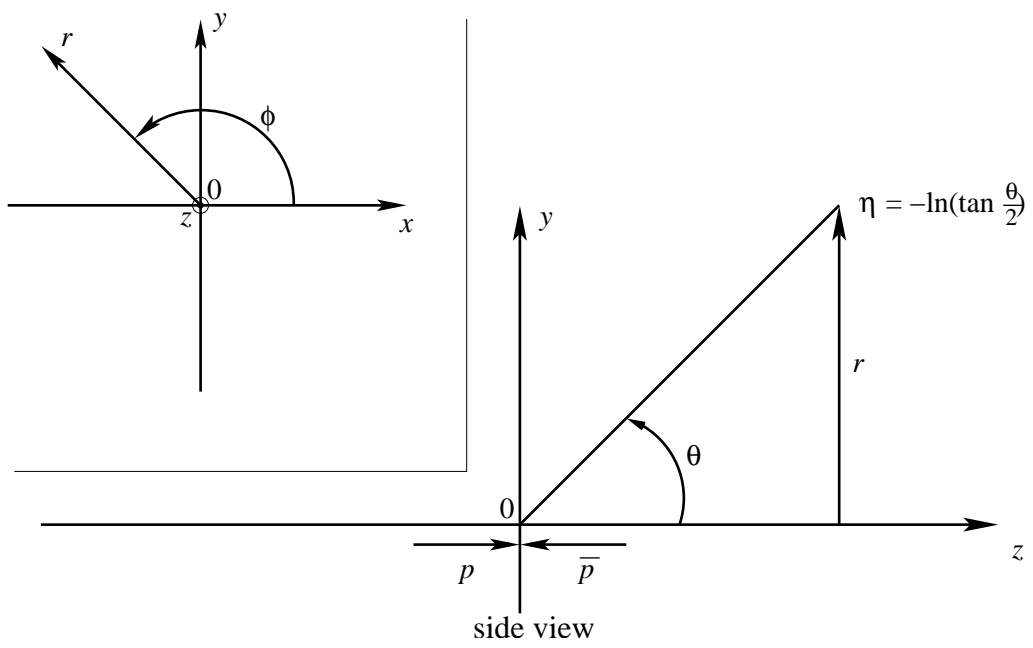
Figure 2.4: Definition of coordinates used with the CDF Run II detector.

1/6th East Endplate(s)
Units: centimeters [inches]

46.976 [18.494]
58.534 [23.045]
70.295 [27.675]
82.055 [32.305]
93.815 [36.935]
105.580 [41.567]
117.340 [46.197]
129.100 [50.827]

Layer #	1	2	3	4	5	6	7	8
Cells	168	192	240	288	336	384	432	480
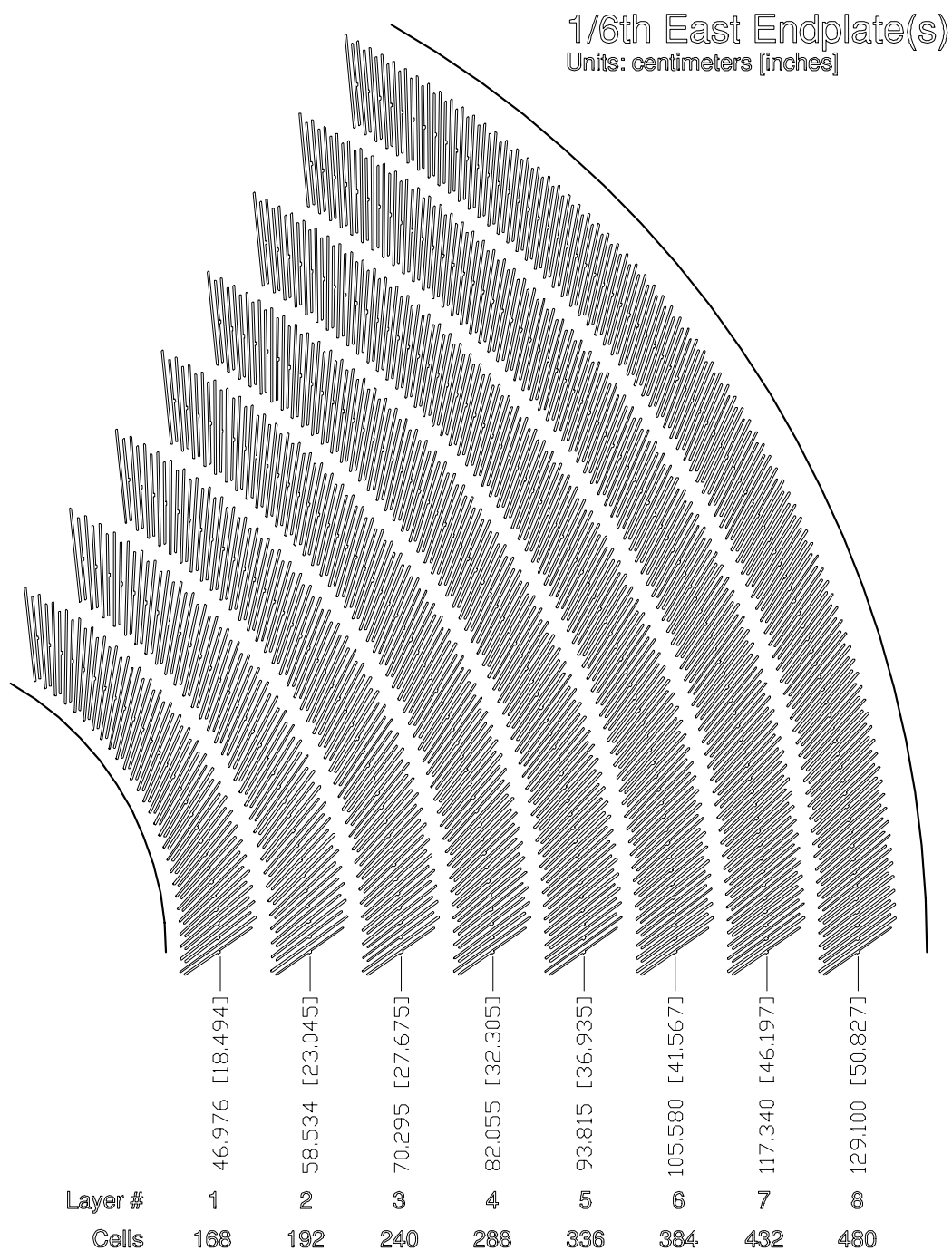
Figure 2.5: End view of a portion of the COT, showing superlayer structure.

36
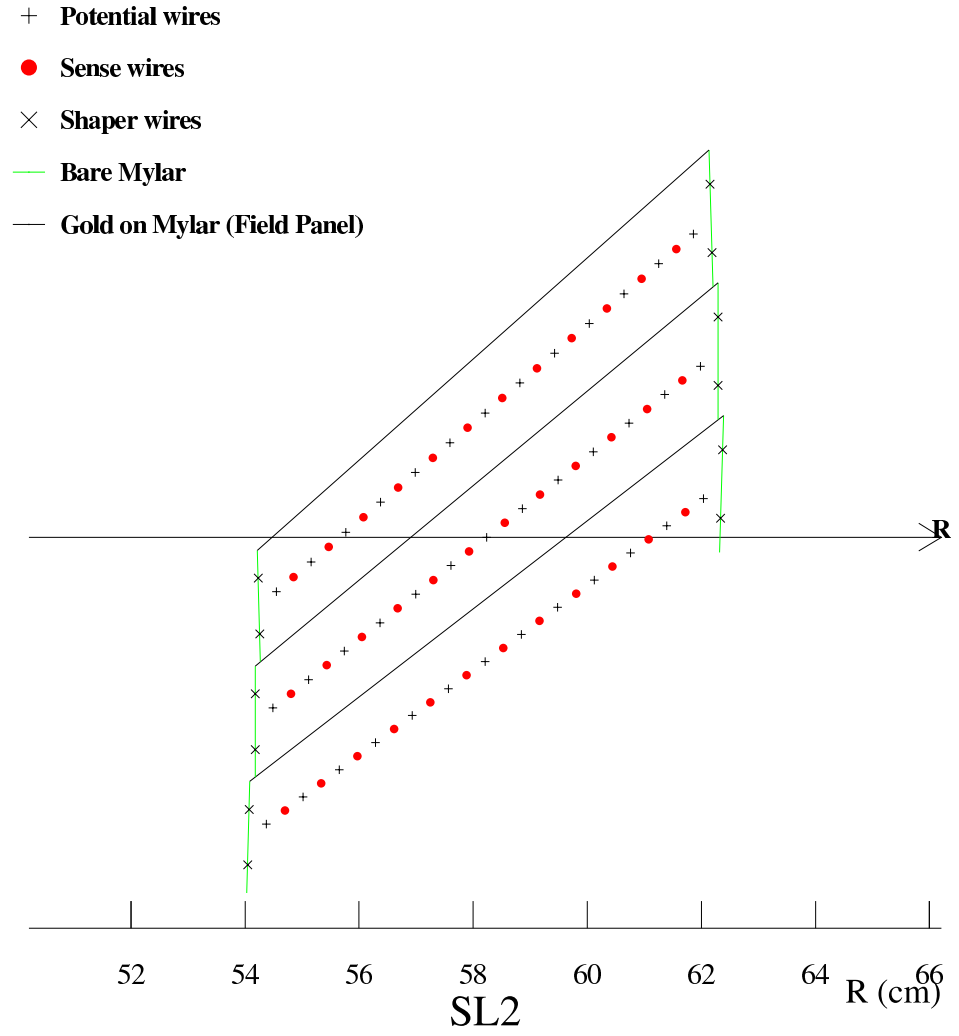
Figure 2.6: Close-up view of three COT cells within a superlayer, which illustrates the position of the wires with respect to the field sheets.
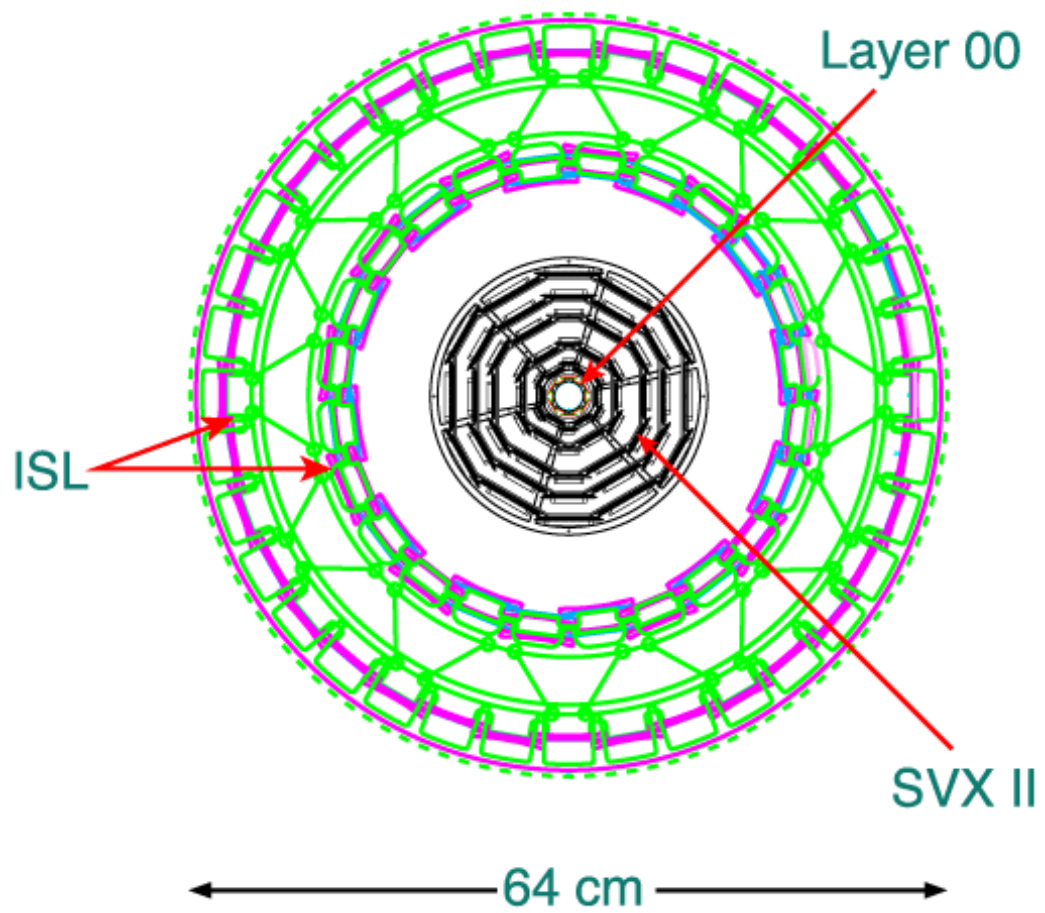
Figure 2.7: An end view of the silicon system, Layer00, SVX II and ISL.
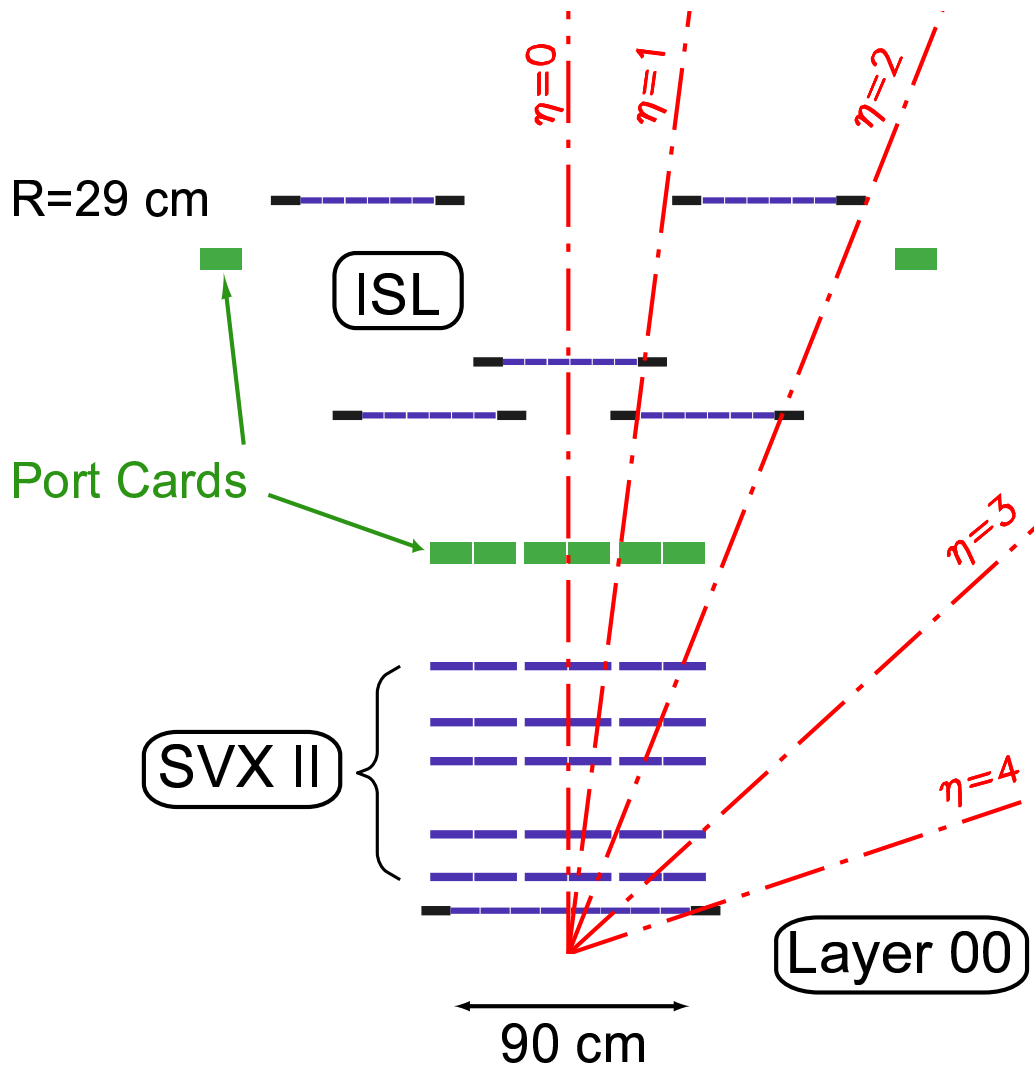
Figure 2.8: A side view of the silicon system. (Scale in z is compressed.)
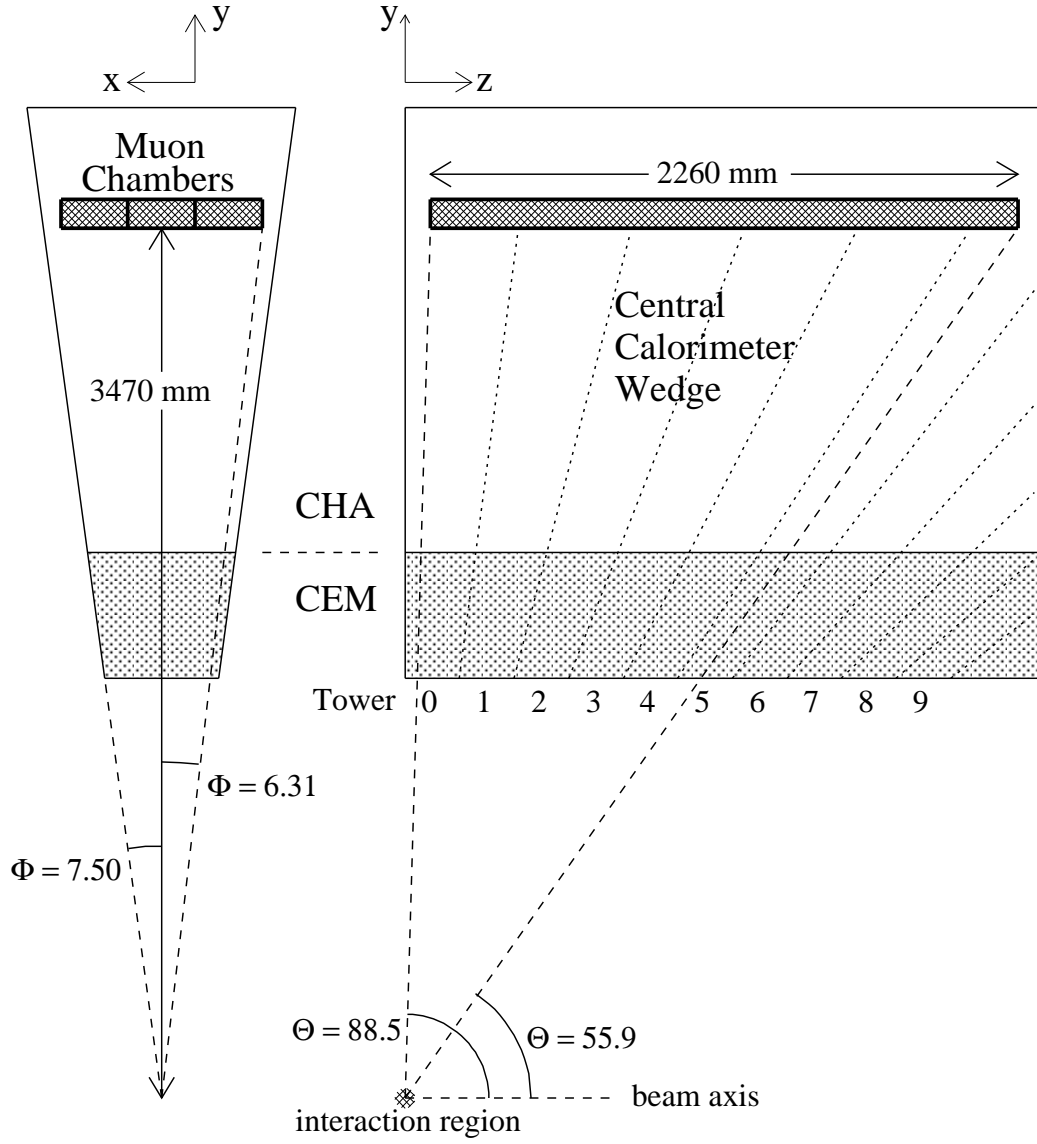
Figure 2.9: Location of Central Muon Detector(CMU), inside of central calorime-

ter.

Muon track   Radial centerline

t_4

t_2

55 mm

To p̄p interaction vertex
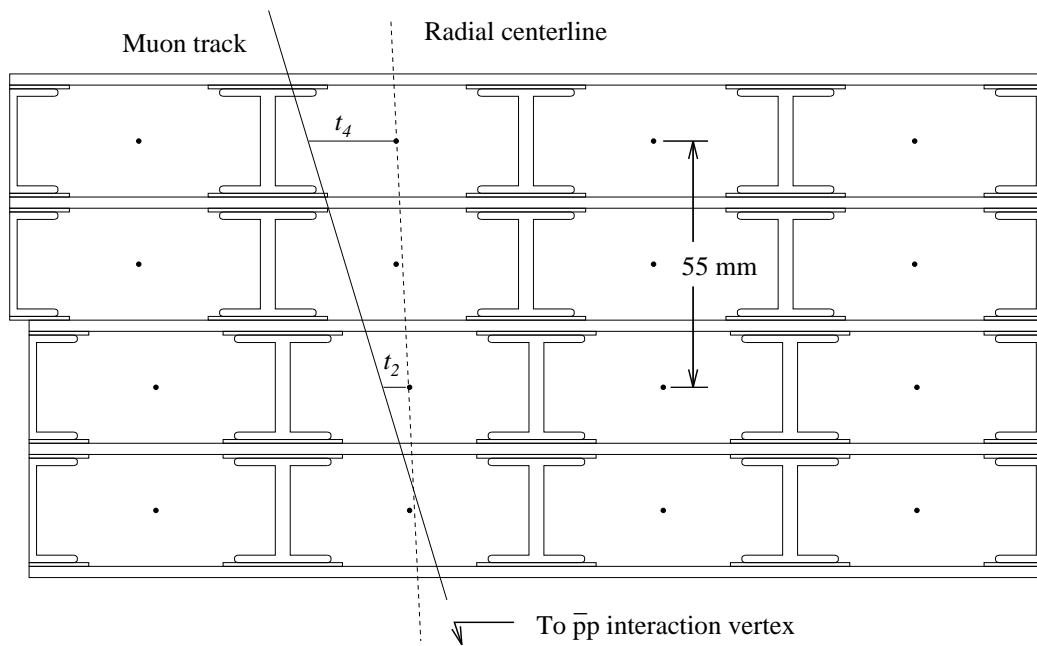
Figure 2.10: An end view of a CMU module, with 4 layers of 4 rectangular single-wire drift cells.
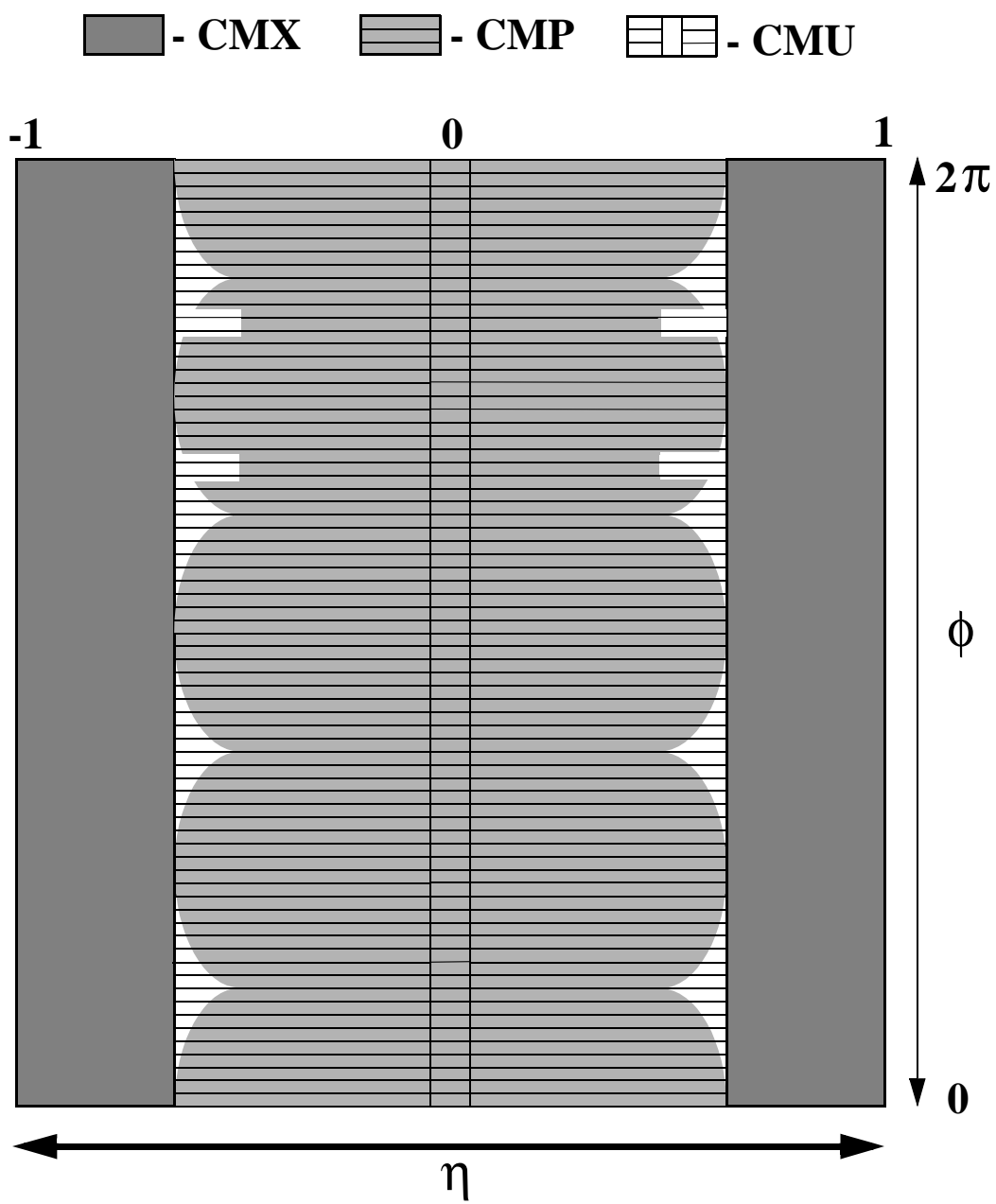
Figure 2.11: Map of the muon coverage.

Dataflow of CDF "Deadtimeless" Trigger and DAQ

Detector

7.6 MHz Crossing rate
132 ns clock cycle

L1 Storage Pipeline:
42 Clock Cycles Deep

L1 trigger

Level1:
7.6 MHz Synchronous pipeline
5544ns latency
<50 kHz Accept rate

L1 Accept

L2 Buffers:
4 Events

L2 trigger

Level 2:
Asynchronous 2 stage pipeline
~20μs latency
300 Hz Accept Rate

L2 Accept

L1+L2 rejection: 20,000:1

DAQ Buffers

L3 Farm

Mass Storage

PJW 10/28/96

Figure 2.12: The readout functional block diagram of the three level system.

Chapter 3

Di-muon selection and

reconstruction

The data sample used for this analysis is $J/\psi \rightarrow \mu^+\mu^-$ sample. It is collected by specific trigger requirements at Level 1 and Level 3. There is no trigger requirement added at Level 2 for this data sample.

At Level 1, two CMU muons are required to exist. For that, there must be two muon stubs in the CMU, and they must be in the search windows set by the XTRP, which receives information of the tracks from the XFT and extrapolates the tracks taking into account the magnetic field and the multiple scattering. The XFT finds tracks in $r - \phi$ plane using the four axial superlayers of the COT, for $p_T \approx$ 1.5GeV/c or above. At this Level, the charges of di-muons are not considered and they can be same sign. As noted above there's no requirement at Level 2 for

this data sample, the events which passed Level 1 are passed to Level 3 trigger automatically.

At Level 3, the two muons are required to have opposite charge, and two muon tracks are required to have $\Delta z < 5$ cm at the point of closest approach to the origin in $r - \phi$ plane. In addition, the invariant mass of the two muons must be between 2.7 and 4.0 GeV/c^2. Two Level 3 trigger paths are used for the data sample of this analysis. For one path, it is required that the dimuon opening angle in the $r - \phi$ plane to be $> 128.90°$, and there's no opening angle requirement for the other path. The data sample triggered without the opening angle requirement is used to the measurement of the cross section for the J/ψs which have transverse momentum range of 0 - 2 GeV/c, because of the masses of J/ψ and muon, $m_{J/\psi} = 3.097$ GeV/c^2 and $m_\mu = 0.106$ GeV/c^2 and the trigger requirement of $p_T \geq 1.5$ by the XFT.

3.1   Offline reconstruction

The data passed all three levels of triggers are

3.2   Good run selection

To make the measurement robust, only "good runs" which are considered good enough for the measurement, are analyzed. To be a good run, the run must be

tagged by online shift operators and offline production operators. Also, for this analysis, COT, muon identification system and trigger system are required to be in good status for the good run. And runs only with greater than 10 nb^{-1} integrated luminosity are used for this analysis.

3.3 J/ψ event selection

Events passed the trigger requirements are reconstructed offline. Further requirements are added after the offline reconstruction besides Level 1 and Level 3 trigger requirements.

Both muons are required to have $p_T > 1.5$ GeV/c as measured offline in the COT. There was a known hardware problem in the di-muon trigger. Events which both two muon stubs fall into 240 - 270° in ϕ are excluded. This problem was fixed after run 150143, but for the uniformity, all the events which have two muon stubs in the region are excluded in this analysis. The muon reconstruction efficiencies for each 48 CMU wedges are measured. The efficiency of the CMU wedge covering 240 - 255° in the west side is found to be lower because of a known hardware trouble. Events in which one of two muon stubs are in the region are excluded in this analysis. Both offline reconstructed muons are required to match the Level 1 and Level 3 trigger requirement.

Table 3.1 shows the selection criteria at each stage of event selection.

Level 1	$p_T(\mu)_{\mathrm{XFT}} > 1.5$ GeV/c
	Muon stubs matched triggered stubs
	Di-muon candidate stubs are seperated by 2 CMU 2.4° towers
	Muon tracks matched to XFT tracks and XTRP projections
	Exclude tracks which pass within 1.5 cm of the center of the COT wire planes in any of the 4 axial layers
	Exclude events where both muon stubs fall in the range 240 - 270° (matchbox 8 problem [35])
Level 2	none
Level 3	CMU muons
	$p_T(\mu)_{\mathrm{COT}} > 1.5$ GeV/c
	Opposite sign muons
	$|z_0(\mu_1) - z_0(\mu_2)| < 5$ cm
	$2.7 < M(\mu\mu) < 4.0$GeV/c^2
	$\Delta\phi(\mu\mu) < 130°$ when $p_T(J/\psi) > 2.0$ GeV/c
	stub-track match: $\Delta(r\phi)_{\mathrm{CMU}} < 30$ cm
Offline	Explicitly require CMU-only or CMUP muons
	$\chi^2(\Delta r\phi)_{\mathrm{CMU}} < 9$
	$|y(J/\psi)| < 0.6$
	COT hits: axial ≥ 20, stereo ≥ 16
	$|z_0(\mu)| < 90$ cm
	Exclude muons in CMU wedge 17W

Table 3.1: Selection criteria at different event selection stages.

47

3.4 J/ψ yield

Differential cross section of the J/ψ is calculated for each divided J/ψ p_T bin. The yield in each J/ψ p_T bin is need to be calculated for the differential cross section calculation. Single gaussian is not good enough to fit the di-muon invariant mass distribution because of the radiative tail. To estimate the J/ψ yield in each p_T bin properly, the di-muon invariant mass distribution in each p_T bin is fitted using MC (Monte Carlo) invariant mass line shapes from including the radiative tail from internal bremsstrahlung obtained from a tuned hit-level COT simulation. To have the invariant mass line shapes, the simulated J/ψ events are decayed using the J/ψ radiative decay model in the QQ decay package [36]. The COT hit multiplicity per track is tuned to match the data as closely as possible, as shown in Fig. 3.1. Then, the COT hit resolution is tuned to find the best χ^2 in a binned fit to the data using the Monte Carlo invariant mass line shape for the signal and a polynomial shape for the background. Finally, energy loss and multiple scattering in material encountered before the COT are modeled. The energy loss in the silicon material is scaled until the peaks of the di-muon invariant mass distribution in different p_T ranges in data and from the simulation match. The order of the background polynomial used varies with the background shape in each J/ψ p_T range. A third-order polynomial is used for the momentum range 0 - 0.25 GeV/c, a second-order polynomial is used for the range 0.25 - 2.25 GeV/c, and a first-order polynomial (linear background) for transverse momenta greater than 2.25 GeV/c. The fits to

the invariant mass distributions in four J/ψ p_T ranges are shown in Figs. 3.2, 3.3, 3.4 and 3.5. The J/ψ yields and the statistical uncertainties obtained from the fits in each p_T range are listed in the first column of Table 3.2. The mass fitting qualities over the whole p_T bins are good as indicated from the fit probability shown in these Figures. The differences ranging from +9% in the lowest p_T bin to -1.3% in the high p_T bin are used very conservatively as the systematic uncertainties from the mass fitting.

3.4.1 Systematic uncertainties and Goodness-of-Fit

A qualitative estimate of the goodness-of-fit is be obtained by defining a quality factor R such that

$$R = \Sigma_i(N_i - N_f) \tag{3.1}$$

where N_i is the number of data events in the ith invariant mass bin and N_f is the fit prediction. For perfect fits, this factor should be consistent with 0. The summation is performed over bins in the invariant mass signal region from 3.02 to 3.15 where the J/ψ signal dominates the background. Deviations from 0 indicate a discrepancy in the yield that is a good estimate of the systematic error on the yield in each p_T bin.

p_T range GeV/c	Yield (N^i)	Acceptance ($\mathcal{A}^i$)	Level 1 Trigger Efficiency(ϵ^i_{L1})	Track-stub matching Efficiency($\epsilon^i_{\chi^2}$)	Luminosity ($\mathcal{L}^i$) nb^{-1}
0.0 - 0.25	365 ± 25	0.0153 ± 0.0007	0.857 ± 0.013	0.9963 ± 0.0009	14830 ± 870
0.25 - 0.5	605 ± 30	0.0069 ± 0.0004	0.860 ± 0.013	0.9963 ± 0.0009	”
0.5 - 0.75	962 ± 38	0.0070 ± 0.0004	0.865 ± 0.013	0.9962 ± 0.0009	”
0.75 - 1.0	1592 ± 49	0.0087 ± 0.0005	0.871 ± 0.014	0.9961 ± 0.0009	”
1.0 - 1.25	2500 ± 62	0.0116 ± 0.0006	0.877 ± 0.014	0.9960 ± 0.0009	”
1.25 - 1.5	3549 ± 74	0.0151 ± 0.0008	0.885 ± 0.014	0.9957 ± 0.0009	”
1.5 - 1.75	4517 ± 84	0.0190 ± 0.0009	0.892 ± 0.014	0.9955 ± 0.0009	”
1.75 - 2.0	5442 ± 93	0.0232 ± 0.0011	0.899 ± 0.015	0.9953 ± 0.0009	”
2.0 - 2.25	16059 ± 167	0.0271 ± 0.0013	0.905 ± 0.015	0.9960 ± 0.0009	39700 ± 2300
2.25 - 2.5	18534 ± 252	0.0317 ± 0.0015	0.911 ± 0.015	0.9946 ± 0.0009	”
2.5 - 2.75	18437 ± 253	0.0367 ± 0.0017	0.916 ± 0.015	0.9943 ± 0.0009	”
2.75 - 3.0	18858 ± 259	0.0415 ± 0.0019	0.920 ± 0.015	0.9939 ± 0.0009	”
3.0 - 3.25	18101 ± 253	0.0467 ± 0.0021	0.924 ± 0.015	0.9935 ± 0.0009	”
3.25 - 3.5	17597 ± 250	0.0532 ± 0.0024	0.927 ± 0.015	0.9931 ± 0.0009	”
3.5 - 3.75	16400 ± 241	0.0576 ± 0.0025	0.930 ± 0.015	0.9927 ± 0.0009	”
3.75 - 4.0	14863 ± 226	0.0628 ± 0.0029	0.932 ± 0.015	0.9923 ± 0.0009	”
4.0 - 4.25	14056 ± 218	0.0694 ± 0.0031	0.934 ± 0.015	0.9918 ± 0.0010	”
4.25 - 4.5	12719 ± 212	0.0768 ± 0.0034	0.936 ± 0.015	0.9913 ± 0.0010	”
4.5 - 4.75	12136 ± 201	0.0840 ± 0.0037	0.937 ± 0.014	0.9909 ± 0.0010	”
4.75 - 5.0	10772 ± 188	0.0904 ± 0.0039	0.939 ± 0.014	0.9904 ± 0.0010	”
5.0 - 5.5	18478 ± 241	0.1006 ± 0.0042	0.940 ± 0.014	0.9897 ± 0.0010	”
5.5 - 6.0	14616 ± 210	0.1130 ± 0.0046	0.942 ± 0.014	0.9887 ± 0.0011	”
6.0 - 6.5	11388 ± 180	0.1257 ± 0.0051	0.946 ± 0.014	0.9876 ± 0.0011	”
6.5 - 7.0	8687 ± 154	0.1397 ± 0.0055	0.945 ± 0.014	0.9865 ± 0.0012	”
7.0 - 8.0	12409 ± 139	0.1561 ± 0.0068	0.946 ± 0.014	0.9850 ± 0.0012	”
8.0 - 9.0	6939 ± 107	0.1723 ± 0.0075	0.947 ± 0.014	0.9827 ± 0.0013	”
9.0 - 10.0	3973 ± 78	0.1807 ± 0.0079	0.948 ± 0.014	0.9804 ± 0.0014	”
10.0 - 12.0	3806 ± 74	0.1938 ± 0.0074	0.949 ± 0.014	0.9772 ± 0.0016	”
12.0 - 14.0	1566 ± 49	0.2163 ± 0.0081	0.960 ± 0.014	0.9726 ± 0.0017	”
14.0 - 17.0	935 ± 40	0.238 ± 0.011 0.	951 ± 0.014	0.9671 ± 0.0018	”
17.0 - 20.0	350 ± 25	0.247 ± 0.012 0.	951 ± 0.014	0.9600 ± 0.0020	”

Table 3.2: Summary of the inclusive J/ψ cross-section analysis components. The values of the yield and statistical uncertainty from the fits are listed in the 2nd column. The acceptance values and the combined systematic and statistical uncertainties on the acceptance are listed in the 3rd column. In the 4th and 5th columns the trigger and track-stub matching efficiencies obtained from the mean of the distribution in each bin and the corresponding systematic uncertainties are listed. The sixth column lists the integrated luminosity used for each measurement.

50

ID	IDB	Symb	Date/Time	Area	Mean	R.M.S.
4000	0	1	030110/1429	2.1152E+05	84.81	7.790
1	0	-31	030109/2213	2.1152E+05	85.50	7.658
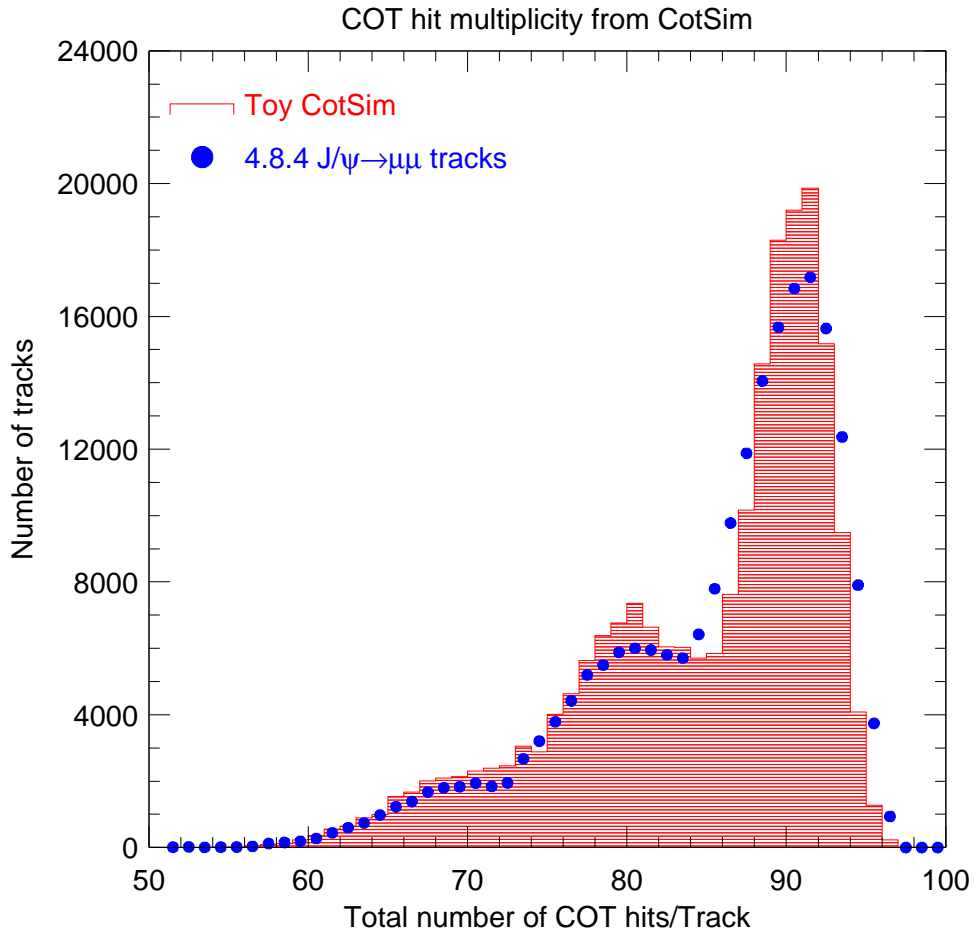
Figure 3.1: COT hit multiplicity distributions on *J/ψ* muon tracks obtained using the simple hit level simulation (shaded histogram) as compared to data. (points with error bars.)
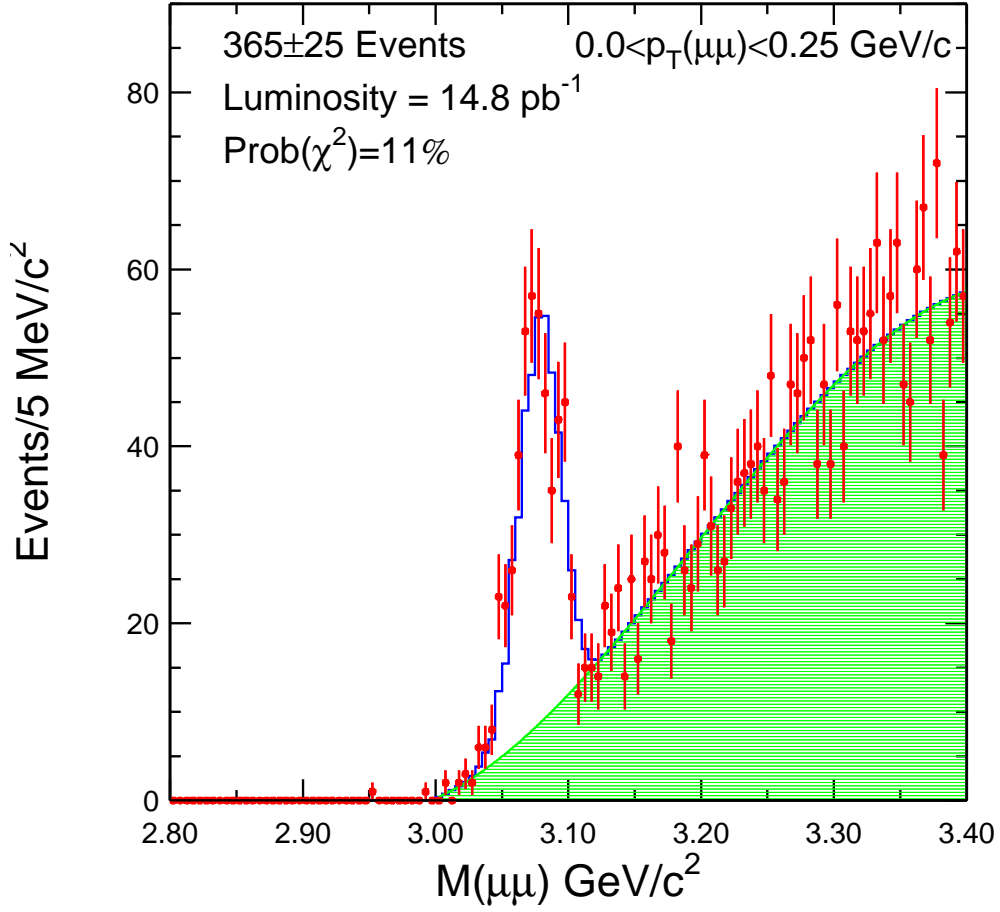
Figure 3.2: Invariant mass distribution of reconstructed $J/\psi \rightarrow \mu\mu$ events in the range $p_T(\mu\mu) < 0.25$ GeV/c. The points with error bars are data. The solid line is the fit to the signal shape from the simulation and a third order polynomial for the background. The shaded histogram is the fitted background shape. The number of signal events and the fit probability of the binned χ^2 fitting are also provided.
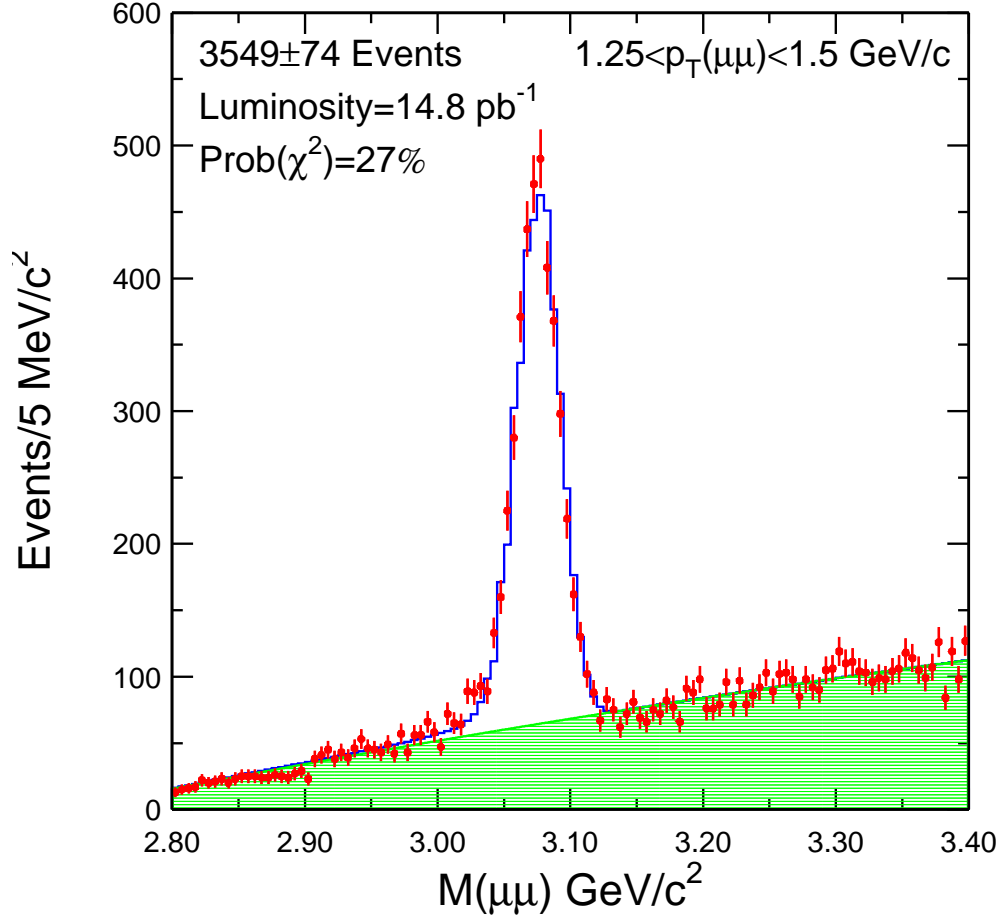
Figure 3.3: Invariant mass distribution of reconstructed $J/\psi \to \mu\mu$ events in the range $1.25 < p_T(\mu\mu) < 1.5$ GeV/c. The points with error bars are data. The solid line is the fit to the signal shape from the simulation and a second order polynomial for the background. The shaded histogram is the fitted background shape.
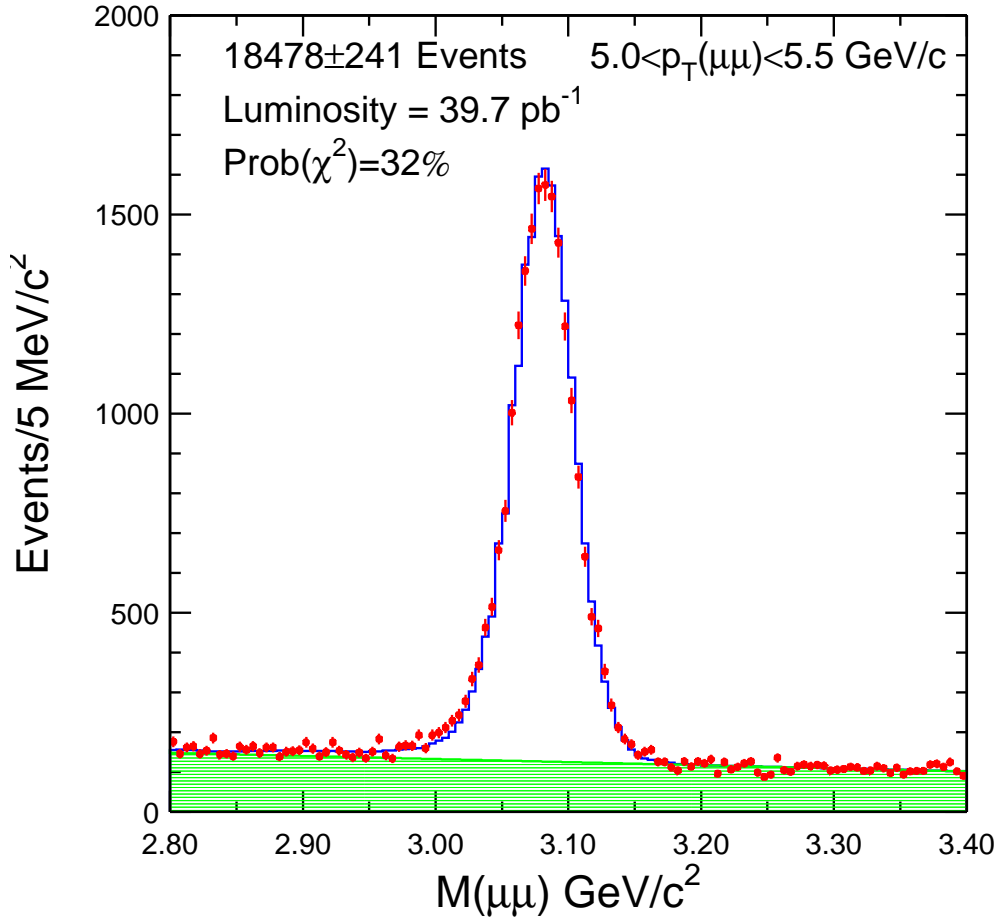
Figure 3.4: Invariant mass distribution of reconstructed $J/\psi \rightarrow \mu\mu$ events in the range $5.0 < p_T(\mu\mu) < 5.5$ GeV/c. The points with error bars are data. The solid line is the fit to the signal shape from the simulation and a linear background. The shaded histogram is the fitted background shape.
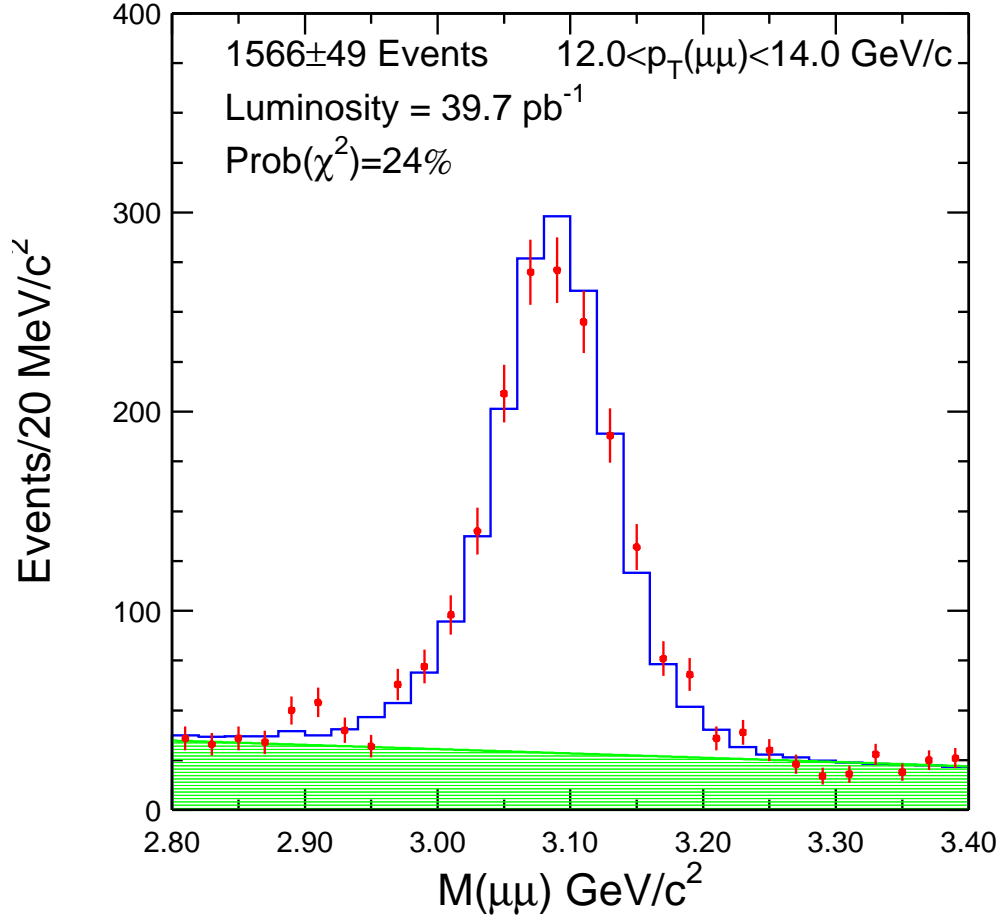
Figure 3.5: Invariant mass distribution of reconstructed $J/\psi \to \mu\mu$ events in the range $12.0 < p_T(\mu\mu) < 14.0 \, \text{GeV}/c$. The points with error bars are data. The solid line is the fit to the signal shape from the simulation and a linear background. The shaded histogram is the fitted background shape.

Chapter 4

Acceptance and efficiencies

4.1 Acceptance

Only a fraction of the J/ψs events produced by $p\bar{p}$ collisions are triggered and reconstructed offline because of the limited geometrical and kinematical acceptance and the incomplete efficiencies of the detectors. The acceptances and the efficiencies must be estimated correctly for the cross section measurement.

4.1.1 Monte Carlo Description

The geometrical and kinematical acceptances are computed from Monte Carlo. Generated J/ψ events are decayed by QQ decay package and processed with GEANT [37] for full detector simulation. The position and slope of the $p\bar{p}$ beams, or SVX II coverage may vary between runs. To take into account for these vari-

ation of the conditions, they are set in the simulation to match the used data used for this analysis. J/ψ events are generated starting with a kinematic distribution that is flat in rapidity and with a p_T distribution selected to best match the reconstructed data. The events are fully simulated. After the differential cross section is measured, the acceptances and the central value of the cross section are recalculated using the measured p_T distribution. The GEANT simulation is validated by comparing the resulting distributions of various kinematic quantities such as η, p_T, the track-stub matching distance, and the z vertex distribution in reconstructed data and reconstructed Monte Carlo events. Differences in the data and Monte Carlo distributions are used to estimate the systematic uncertainties on the modeling of the CDF detector geometry in the simulation.

4.1.2   Acceptance

The detector acceptance is needed for the cross section measurement to correct the yield of J/ψ. For this analysis, since J/ψ is reconstructed in the decay mode $Jpsi \rightarrow \mu^+\mu^-$, the acceptance of muon is concerned. The CMU muon detector covers $-0.6 < \eta < 0.6$. And it is segmented into 24 wedges in ϕ, each wedge covers $12.6°$ and $2.4°$ separation between each wedge, as shown in Fig. 2.11. For this region, the COT covers 100 % and the geometrical acceptance is determined only by the CMU. Besides the geometrical acceptance, the kinematical acceptance must be estimated too. The calorimeter systems, which are placed inside

the CMU, work as an absorber for the CMU, and muons which have $p_T < 1.35$
GeV/c cannot reach the CMU. Also, the CMU set a lower limit for the p_T of
muons, by calculating the difference of drift times in sense wires on alternating
layers. The $\Delta t \leq 396$ ns timing window is selected to be fully efficient for muons
with $p_T > 1.5$.

The acceptance is modeled as a function of both the reconstructed $p_T(J/\psi)$
and rapidity $y(J/\psi)$ and is defined as the ratio between the number of generated
events N^{gen} and reconstructed events N^{rec},

$$\mathcal{A}(p_T, y) = \frac{N^{\text{rec}}(p_T(J/\psi), |y(J/\psi)| < 0.6)}{N^{\text{gen}}(p'_T(J/\psi), |y'(J/\psi)| < 0.6)} \tag{4.1}$$

where $p'_T(J/\psi)$ and $y'(J/\psi)$ are the true value of momentum and rapidity of the
generated $Jpsi$, respectively. $p_T(J/\psi)$ and $y(J/\psi)$ may differ from $p'_T(J/\psi)$ and
$y'(J/\psi)$ because of the detector resolution. The acceptance as a function of p_T and
y is shown in Fig. 4.1.

The acceptance increases rapidly from 0.7% at $p_T = 0.25$ GeV/c to 10% at
5 GeV/c and 25% at 20 GeV/c. The acceptance in the range 0.0-0.25 GeV/c is
rapidly varying as a function of $p_T(J/\psi)$ and increases with decreasing momenta
from 0.7% at $p_T(J/\psi) = 0.25$ GeV/c to 4% for J/ψ mesons almost at rest ($p_T < 50$
MeV/c). The muon transverse momentum is required to be greater than or equal
to 1.5 GeV/c, which is close to one-half of the J/ψ mass, therefore when the J/ψ
is at rest both muons are likely to be above the p_T threshold. As soon as the J/ψ
receives a small boost, the probability is greater that at least one muon will be

below the p_T acceptance threshold and the acceptance starts to decrease until the J/ψ transverse momentum exceeds 0.25 GeV/c.

Acceptance $\mathcal{A}$ at $|y| = 0.6$ is not 0, though the value is small. This is because of detector resolution and the size of the interaction region. To estimate this effect, J/ψ Monte Carlo events are generated flat distribution in η of the range $|y| < 1.0$, and the p_T distribution selected to best match the reconstructed data as above. The relative acceptance $\mathcal{A}'$, for events generated with $|y(J/\psi)| > 0.6$ and reconstructed with $|y(J/\psi)| < 0.6$, is calculated as

$$\mathcal{A}' = \frac{N^{\text{rec}}(|y(J/\psi)|_{\text{gen}} > 0.6, |y(J/\psi)|_{\text{rec}} < 0.6)}{N^{\text{gen}}(|y(J/\psi)|_{\text{gen}} < 0.6)}, \tag{4.2}$$

where $N^{\text{rec}}(|y(J/\psi)|_{\text{gen}} > 0.6, |y(J/\psi)|_{\text{rec}} < 0.6)$ is the number of J/ψ events in the Monte Carlo sample, which are generated $|y(J/\psi)|_{\text{gen}} > 0.6$ and reconstructed $|y(J/\psi)|_{\text{rec}} < 0.6$, and $N^{\text{gen}}(|y(J/\psi)|_{\text{gen}} < 0.6)$ is the total number of events generated with $|y(J/\psi)| < 0.6$. The value of $\mathcal{A}'$ is found to be very small: $\mathcal{A}' = 0.00071 \pm 0.00006\text{(stat)}$. A correction factor of $(1 - \mathcal{A}') = 99.93\%$ is applied to the J/ψ yield calculated in each $p_T(J/\psi)$ bin.

A 2-dimensional acceptance function is used for an event-by-event correction for the calculation of the J/ψ cross section. In Table 3.2, the acceptance values averaged for the y, and the combined statistical and systematic uncertainties for each p_T bin are listed. J/ψ spin alignment, p_T spectrum, CMU simulation and detector material description in GEANT simulation are considered as the source of the systematic uncertainties and described in following section.

4.1.3 Systematic uncertainties of acceptance

Since the J/ψ spin alignment affect the p_T of muons from the J/ψ decay, kinematic acceptance as a function of p_T depends on the J/ψ spin alignment. The normalized spin alignment distribution is given by

$$I(\theta) = \frac{3}{2(\alpha + 3)}(1 + \alpha \cos^2 \theta), \tag{4.3}$$

where θ is the angle between the direction of the muon in the J/ψ rest frame and the direction of the J/ψ in the lab frame [15], and α quantifies the spin alignment. The parameter α must lie in the range -1 to 1 and $\alpha = 0$ indicates no preferred spin alignment. The CDF Run I measurements of the J/ψ spin alignment parameter [15] are consistent with zero but could also be as large as 50% in some p_T regions. The weighted mean of α measured in different p_T ranges in [15] is used to determine the central value of the parameter α to be used for the acceptance. The value of $\alpha = 0.13 \pm 0.15$ is used for the final acceptance values where the uncertainty is chosen to accommodate the variation in the previous CDF measurements and the extrapolation to $p_T = 0$ where α is expected to be zero. The uncertainty on acceptance due to spin alignment is largest in the lower momentum bins for it affects to transverse momentum of muons from J/ψ decay and they have more chance to have p_T lower than 1.5 GeV/c, and decreases with increasing transverse momentum. The uncertainty from this source is found to be $\sim$ 5% near $p_T = 0$ and 2% in the region $17 < p_T < 20$ GeV/c. The values of α obtained from the

Run I measurement [15] are listed in Table 4.1.

p_T bin	inclusive α	σ syst.	σ total
4-5	0.236 ± 0.097	0.13	0.162
5-6	-0.001 ± 0.073	0.07	0.101
6-8	0.209 ± 0.054	0.04	0.067
8-10	0.266 ± 0.065	0.02	0.068
10-12	0.084 ± 0.084	0.02	0.086
12-15	0.14 ± 0.11	0.02	0.112
15-20	-0.30 ± 0.12	0.05	0.130

Table 4.1: Value of the inclusive J/ψ spin alignment parameter α, measured in Run I [15].

Though true J/ψ p_T spectrum is not known (it's the subject of this analysis), a p_T spectrum is needed for the generation of J/ψ events. To estimate the uncertainty from variations of the input transverse momentum spectrum of the generated J/ψ , the acceptance is recalculated using a Monte Carlo sample generated using a flat distribution in p_T. The flat distribution is an extreme alternative from the nominal spectrum which is a fast falling function of p_T. The fractional change in acceptance is taken as the uncertainty on the input transverse momentum distribution. The uncertainty is about 3% in the lowest momentum bin, less than 1%

in the 0.25 to 3 GeV/c bins, 1 - 2% in the 3 to 4GeV/c bins, and 2 - 4% in the 4 to 20 GeV/c bins.

The modeling of the CMU in the GEANT detector simulation can have sources of the uncertainty in the acceptance calculation. The major sources of the GEANT simulation related to the CMU are, the CMU coverage in $r - z$ plane, the wire efficiency differences between wedges in east and west and in different ϕ sections, and beam position in z. The uncertainties are estimated by comparing event distributions in data and in the Monte Carlo, and total uncertainty for the CMU modeling in the simulation is found to be 1.0%.

There is a gap between the east and west arches of the CMU, that is in the center of the CMU in $r - z$ plane ($\eta = 0$). The size of the gap is approximately ± 11 cm, measured at $r = 347$ cm. A muon, which is extrapolated to the gap region, may be detected in the CMU because of the multiple scattering in the detector. The fraction of the muons extrapolated to the gap region but detected by the CMU is estimated in both the data and the Monte Carlo. And the difference of the fractions between the data and the Monte Carlo is taken as the uncertainty on the acceptance from this source. It is found to be 0.20%. The fraction of data and MC events falling in the gap region is shown in Fig. 4.2.

The number of observed $J/\psi \rightarrow \mu^+\mu^-$ events are different in east and west part of the CMU due to several sources, including the shift in the average primary vertex location towards positive z (east), the exclusion of the low efficiency wedge on

62

the west side of the detector 17W, and the uncertainty in the modeling of the z extent of the CMU detector, as well as the differences in the east and west chambers. East-west asymmetries in the CMU are calculated from the number of observed events in east and west part of the CMU, for both the data and the Monte Carlo. The uncertainty in the modeling of the east and west CMU part is defined as the difference between asymmetries of the data and the Monte Carlo.

Each CMU wedge has different gain and efficiency for muons, but this difference is not included in the GEANT simulation. This can be source of the systematic uncertainty for the acceptance calculation. To study this source the number of events reconstructed in each wedge in Monte Carlo is normalized to match the data, and the number of events reconstructed in both data and Monte Carlo are investigated. The standard deviation of the difference in number of events reconstructed in each wedge in data and MC is taken as the uncertainty of the GEANT CMU ϕ acceptance. And it is found to be 0.55%. The number of events reconstructed in each wedge in data and MC is shown in Fig. 4.3. The total number of events in MC is normalized to match the data.

Interaction points of the generated J/ψ events in the Monte Carlo are distributed as to match that of the data. And muons from J/ψ are required to have the z_0 position to be within 90 cm of the center of the detector, $|z_0(\mu)| < 90$ cm. Comparing the $z_0(\mu)$ distribution of the Monte Carlo and the data shows a small disagreement between them as shown in Fig. 4.4. This is because of inadequate

modeling of the interaction region in the Monte Carlo. This contributes to the acceptance calculation as the source of the systematic uncertainty, and the contribution is estimated from the difference in the ratio of data and MC tracks with $|z_0(\mu)| < 90$ cm compared to all CMU muons. It is found to be 0.28%.

The muons pass through all the detector component inside the CMU and lose part of its energy. The material description of the detector in GEANT determines the amount of energy loss according to the pass of the muons in the detector. Inside the tracking volume, the silicon system has biggest influence to the energy loss, and it effects particularly to J/ψ of low transverse momenta. To estimate the systematic uncertainty on the acceptance from the inaccurate detector material description, the SVX II material used in the GEANT detector simulation is varied by 10 % to 20%. The systematic uncertainty is taken as the difference between the acceptance values measured with different material scale factors and the nominal. The uncertainty is largest in the low momentum bins as expected, and it is around 5%.

The systematic uncertainties on acceptance calculation are summarized in Table 4.2. The size of the uncertainties from J/ψ spin alignment, J/ψ p_T spectrum and detector material description depends on the muon p_T range as expected, while the uncertainty from muon detector simulation is same for all p_T ranges of interests in this analysis.

	Source	Size
Acceptance	J/ψ spin alignment	$\pm(2 \rightarrow 5)\%(p_T)$
Acceptance	p_T spectrum	$\pm(0 \rightarrow 5)\%(p_T)$
Acceptance	Detector material	$\pm(0.4 \rightarrow 5)\%(p_T)$
Yield	Mass fits	$(-1.3 \rightarrow +9)\%(p_T)$
Yield	Momentum scale	$(-0.1 \rightarrow +0.7)\%(p_T)$
Luminosity	CLC	$\pm6.0\%$
Reconstruction	Table II	$\pm2.8\%$
Acceptance	CMU simulation	$\pm1.0\%$
Yield	Data quality	$\pm1.0\%$
L1 trigger efficiency	Table I	$\pm1.5\%$
Total	$\pm6.9\% \oplus \delta(p_T)$	

Table 4.2: Summary of systematic uncertainties in the inclusive J/ψ cross section measurement. The p_T dependent uncertainties are listed in the top section of the table. In general, the p_T dependent uncertainties increase with decreasing p_T. The total is calculated from the p_T independent sources only.

4.2 Data Quality

Although the only "good runs" described in 3.2 are analyzed, the analyzed data sample may include hardware problems. To investigate detector performance, the yield, mean, and resolution of the J/ψ invariant mass peak are monitored during the period of the data taking. Runs which have J/ψ yield different by 4σ from the average are identified as outlying runs, where σ is the standard deviation of the yield of the run in a given run range. There are two such runs identified, out of 457 considered. The integrated luminosities of these two runs are 14.3 nb and 258.3 nb, respectively. Further investigations of online operational conditions during these runs do not revealed any obvious hardware or trigger problem. On the other hand, since the probability which a data subsample of 258.3 nb out of a total sample of 39.7 pb would have a yield different by $> 4\sigma$, is 1%, both runs are not excluded. Instead, the measurement is repeated without the outlying runs included, and the difference in the measurements is taken as a systematic uncertainty. The uncertainty on the total cross section is found to be less than 1%.

4.2.1 Level 1 trigger efficiency

The Level 1 di-muon trigger efficiency is measured by using J/ψ events, which are collected with a high p_T single-muon trigger [35]. At Level 1, this trigger requires

a muon which have p_T grater than 4.0 GeV/c. At Level 3, a J/ψ is reconstructed with the muon passed the Level 1 requirement and the muon which is not required to pass the Level 1 trigger. This second muon which is not required to pass at Level 1, is used to measure the Level 1 single-muon efficiency.

The denominator for the efficiency calculation is the number of J/ψ reconstructed with Level 3 track and muon information. These J/ψ candidates must have an invariant mass between 2.7 and 3.6 GeV/c^2, a opening angle of di-muon $\Delta\phi_0$ is less than 130°, and a difference of the two muon tracks in z_0 is less than 5 cm. The probe muon are required to satisfy following:

- To have at least 20 COT axial-layer hits and 16 COT stereo-layer hits.

- z_0 of the track is within 90 cm of the detector center, $|z_0| < 90$ cm.

- Matching between the track and the CMU stub in $r - \phi$ is $\chi^2(\Delta r\phi) < 9$.

- Do not pass within 1.5 cm of the center of any of the COT wire planes in any of the axial layers in order to avoid the inefficient region caused by wire supports.

- The associated Level 3 track must be matched to an XFT track and the Level 3 CMU stub must be matched to a Level 1 CMU stub that lies within XTRP window, to pass the Level 1 tirgger.

Measured Level 1 CMU efficiency is shown in Fig. 4.5. To correct the J/ψ yield

67

later, the measured efficiency is fit with a function:

$$\epsilon_{L1}^{\mu}(p_T^{\mu}) = E \cdot \text{freq}\left(\frac{A - 1/p_T}{R}\right),$$ (4.4)

where freq is the normal frequency function:

$$\text{freq}(x) = \frac{1}{\sqrt{2\pi}} \int_{-\infty}^{x} e^{-\frac{1}{2}t^2} dt.$$ (4.5)

E is the plateau efficiency, A is associated with the p_T at which the efficiency is half the peak value, and R is the effective Gaussian resolution, and from the fit, $E = 0.977 \pm 0.002$, $A = 1.1 \pm 0.1$ (GeV/c)$^{-1}$, and $R = 0.28 \pm 0.06$ (GeV/c)$^{-1}$, respectively.

Next, the uncertainty in the Level 1 trigger efficiency must be estimated. To estimate the uncertainty, the range of the uppermost and lowermost fluctuations supported by the data are computed as follows: $x'(p_T) = \bar{x} \pm (|x - \bar{x}| + 1\sigma)$ where x is the data value, $\bar{x}$ is the value returned by the fit and σ is the uncertainty on the data, while also taking into account the data fluctuations around the central fit. The $x'(p_T)$ distribution is also fitted with the same function in Equation 4.4, and is shown in Fig. 4.5 as dashed lines.

The di-muon Level 1 trigger efficiency is calculated as:

$$\epsilon_{L1}^{J/\psi}(p_T^{J/\psi}) = \epsilon_{L1}^{\mu}(p_T^{\mu_1}) \cdot \epsilon_{L1}^{\mu}(p_T^{\mu_2})$$ (4.6)

where, $\epsilon_{L1}^{\mu}(p_T^{\mu})$ is the single muon Level 1 trigger efficiency given by Equation 4.4, and $p_T^{\mu_{1,2}}$ are the transverse momenta of the two muons. The trigger's exclusion

of pairs with nearby stubs is included as part of the geometric acceptance. The mean of the Level 1 di-muon trigger efficiency distribution in each J/ψ transverse momentum bin is listed in Table 3.2. The maximum difference from varying the trigger efficiencies by one standard deviation independently for the two muons is listed as the uncertainty on the di-muon trigger in Table 3.2. The variation is found to be within ±1.5% in all bins.

4.2.2 Level 3 trigger efficiency

The Level 3 reconstruction efficiency is dominated by the difference between the online and offline tracking efficiency. A fast tracking algorithm is used for pattern recognition in the COT at Level 3. In the offline reconstruction a more accurate tracking algorithm is combined with the result of the Level 3 algorithm to give a higher overall COT tracking efficiency. The Level 3 single-muon reconstruction efficiency as measured versus the offline reconstruction algorithm is found to be constant for $p_T(\mu) > 1.5$ GeV/c and is

$$\epsilon^{\mu}_{\text{L3/Offline}} = 0.997 \pm 0.001(\text{stat}) \pm 0.002(\text{syst}). \tag{4.7}$$

At the Level 3 trigger, the muons are required to be separated in z_0 by less than 5 cm. The efficiency $\epsilon_{\Delta_{z0}}$ of this cut is measured using J/ψ candidates reconstructed in single-muon-trigger data samples where a Level 3 di-muon trigger was not required to acquire the data. The numbers of events that passed the z_0-

separation criterion in the mass signal and sideband regions are examined. The cut is found to be 100% efficient with an uncertainty of 0.1%. The uncertainty is driven by the statistical limitations of the small data samples obtained from the single-muon triggers.

4.2.3 COT offline reconstruction efficiency

The COT tracking efficiency is measured using a Monte Carlo track embedding technique [38]. Hits from simulated muon tracks are embedded into CDF Run II di-muon data sample, and muon tracks are reconstructed same way with the data sample. The denominator for the track reconstruction efficiency is the number of embedded tracks, and the numerator is the number of tracks which are reconstructed from embedded hits. The distance resolution and hit-merging distance are adjusted so the embedded track has residuals and hit distributions matched to muon tracks in J/ψ data events. The efficiency of COT track reconstruction in di-muon events is found to be

$$\epsilon_{\text{COT}}(p_T^\mu > 1.5\text{GeV}/c) = 0.9961 \pm 0.0002(\text{stat})_{-0.0091}^{+0.0034}(\text{syst}). \tag{4.8}$$

4.2.4 CMU offline reconstruction efficiency

The offline reconstruction efficiency of muons, including stub reconstruction and matching between stubs and tracks is measured using $J/\psi \rightarrow \mu^+\mu^-$ events. J/ψs

are reconstructed from single-muon trigger samples, where one of the two muons is a triggered, fully reconstructed muon and second muon is a track [39]. Second muon tracks which are in the di-muon mass signal region, are extrapolated to the muon chambers, and the efficiency of finding a matched stub is measured. For muons in the CMU fiducial region with $p_T(\mu) > 1.5$ GeV/c, the offline reconstruction efficiency is found to be independent of p_T and is measured to be [40]:

$$\epsilon_{\text{CMU}} = 0.986 \pm 0.003(\text{stat}) \pm 0.010(\text{syst}). \tag{4.9}$$

To select clean CMU muons, the track-stub matching in the $r - \phi$ plane is required to have $\chi^2(\Delta r\phi) < 9$. The efficiency of this cut is found to have a weak dependence on p_T^μ and:

$$\epsilon_{\chi^2} = (1.0018 \pm 0.0003) - (0.0024 \pm 0.0001)p_T^\mu. \tag{4.10}$$

The efficiency of the track-stub matching criterion ($\chi^2(\Delta r\phi) < 9$) as a function of J/ψ transverse momentum, obtained using an event-by-event weighting is listed in Table 3.2. The systematic uncertainty on the weighted-average matching-cut efficiency is obtained by varying the normalization and slope in Equation 4.10 by one standard deviation. The change in the weighted average efficiency in each J/ψ transverse momentum bin is found to be $\leq 0.2\%$.

4.2.5 J/ψ offline reconstruction efficiency

Since the two muons originate from a common decay point, the efficiency of the track z_0 cut is fully correlated for the two muons and is counted only once. The combined p_T independent COT-tracking, muon and Level 3 reconstruction efficiencies for J/ψ mesons is calculated to be

$$\epsilon_{\text{rec}} = \epsilon_{\text{L3}} \cdot \epsilon_{\text{COT}} \cdot \epsilon_{\text{CMU}} \cdot \epsilon_{z_0} \cdot \epsilon_{\Delta_{z_0}} = 95.5 \pm 2.7\%. \tag{4.11}$$

Table 4.3 summarizes the p_T-independent reconstruction efficiencies and those of the various muon selection cuts.

J/ψ Selection	Efficiency
Level 3 muon reconstruction	$\epsilon_{\text{L3}} = 0.997 \pm 0.001 \pm 0.002$
COT offline tracking	$\epsilon_{\text{COT}} = 0.9961 \pm 0.0002^{+0.0034}_{-0.0091}$
Muon offline reconstruction	$\epsilon_{\text{CMU}} = 0.986 \pm 0.003 \pm 0.010$
Muon z_0 position less than ± 90 cm	$\epsilon_{z_0} = 0.9943 \pm 0.0016$
Di-muon z_0 separation less than 5 cm	$\epsilon_{\Delta_{z_0}} = 1.0 \pm 0.001$
Total reconstruction	$\epsilon_{\text{rec}} = \epsilon^2_{\text{L3}} \cdot \epsilon^2_{\text{COT}} \cdot \epsilon^2_{\text{CMU}} \cdot \epsilon_{z_0} \cdot \epsilon_{\Delta_{z_0}} = 95.5 \pm 2.7\%$

Table 4.3: Summary of J/ψ reconstruction efficiencies.
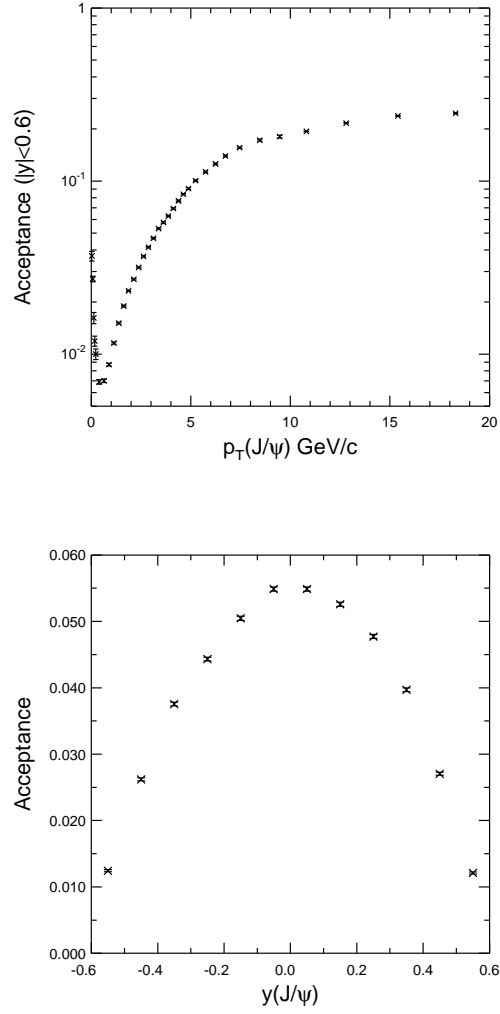
Figure 4.1: Acceptance of $J/\psi \rightarrow \mu\mu$ events measured using a GEANT simulation of the CDF II detector. The acceptance is shown as a function of $p_T(J/\psi)$ and $y(J/\psi)$.

Data: trk1zatcmu minus

Data: trk1zatcmu minus

Data: trk1zatcmu plus
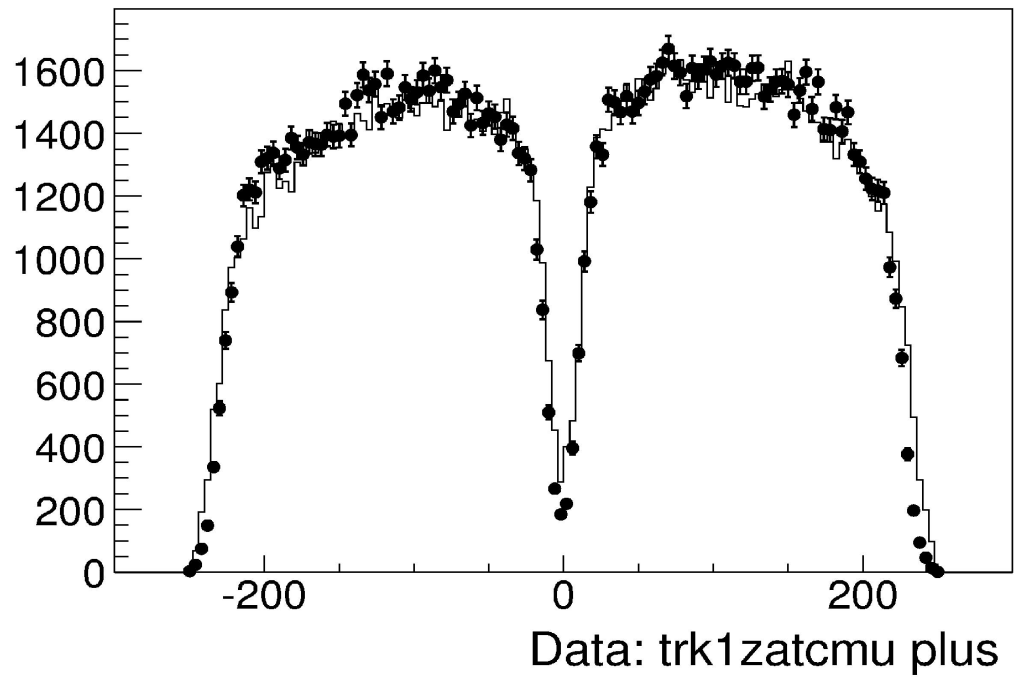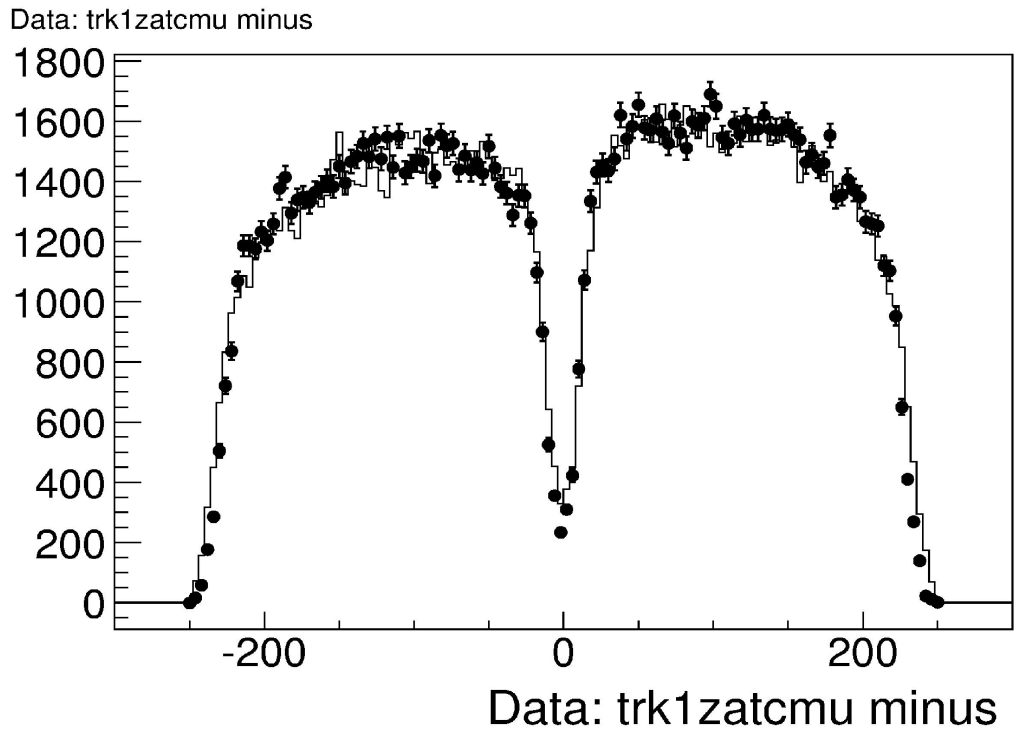
Figure 4.2: Data/MC comparison of the μ track z co-ordinate measured at R = 347 cm. Histograms are GEANT MC from cdfsoft v4.9.1, black circles are data processed with cdfsoft v4.8.4. COT only tracks is used.
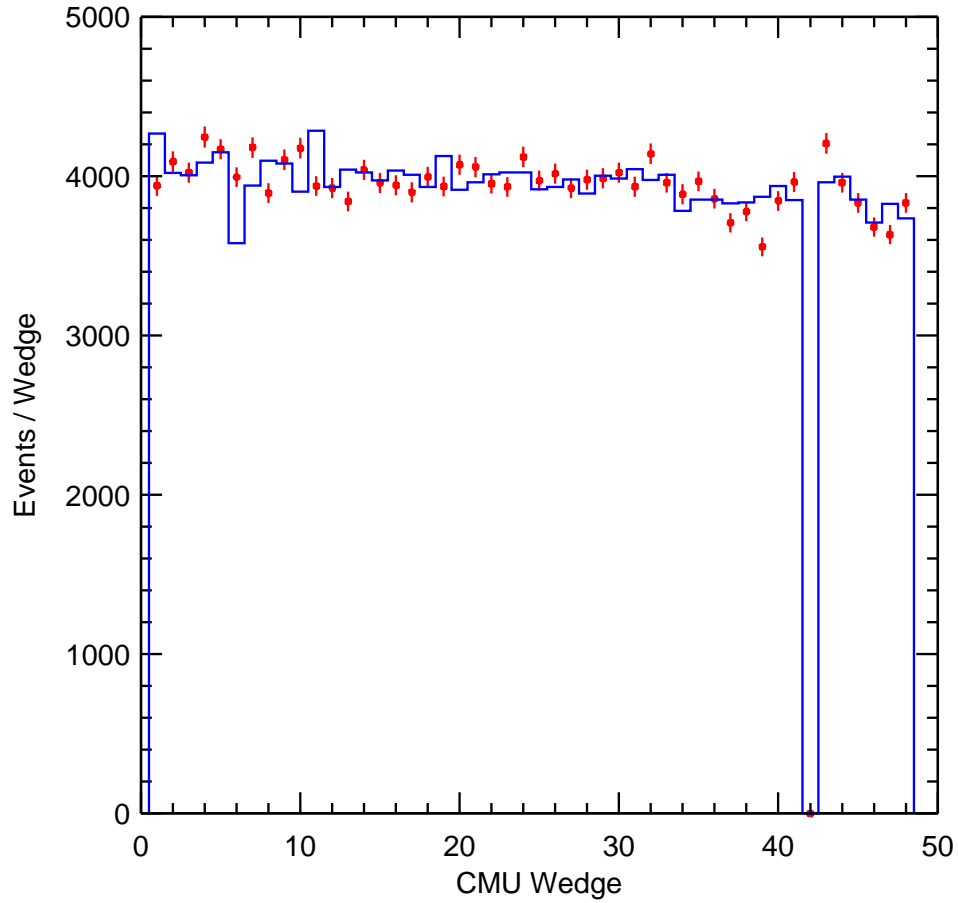
Figure 4.3: Data/MC comparison of the number of events in each of the 48 muon wedges. The total number of events in the MC is normalized to data. Wedges on the east are numbered 0-23 and wedges on the west are numbered from 24-47. Histograms are GEANT MC from cdfsoft v4.9.1, black circles are data processed with cdfsoft v4.8.4.
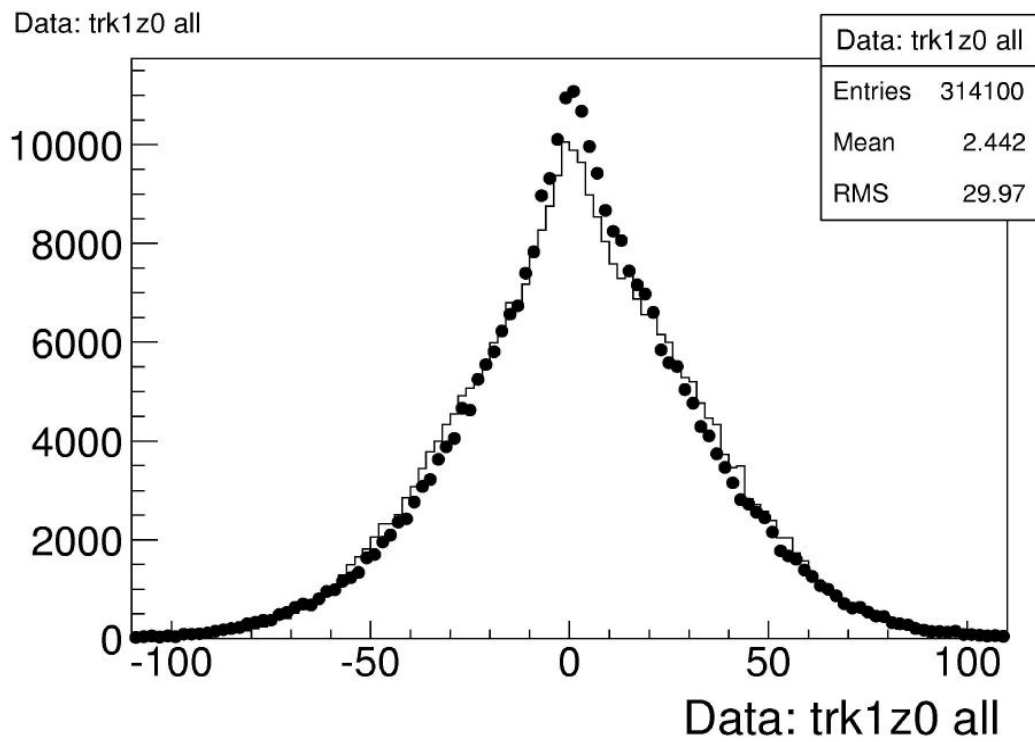
Figure 4.4: Data/MC comparison of the μ track z_0 coordinate Histograms are GEANT MC from cdfsoft v4.9.1, black circles are data processed with cdfsoft v4.8.4.

76
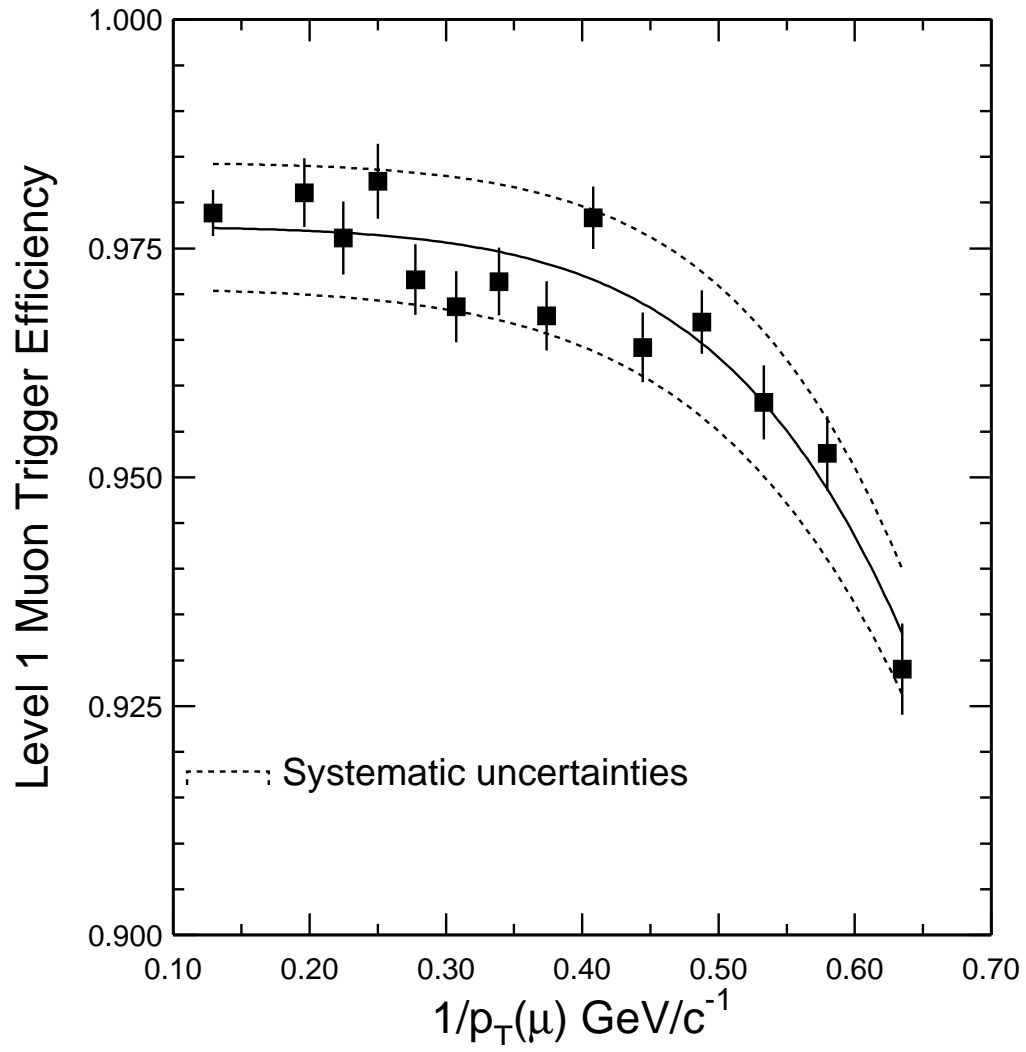
Figure 4.5: Fit to L1 CMU trigger efficiency data used in the cross-section measurement (solid line) and the range used to determine the uncertainty (dashed line).

Chapter 5

J/ψ cross section

For the J/ψ cross section measurement, the J/ψ yield in each p_T bin is weighted event-by-event to account for the measured efficiency and acceptance described in chapter 4.1. Each event is weighted using the Level 1 single muon efficiency $\epsilon_{\text{L1}}(p_T)$ and the efficiency of the track-stub matching criterion $\epsilon_{\chi^2}(p_T)$ applied to each of the two muons. The event is then corrected for the acceptance $\mathcal{A}(p_T^{J/\psi}, y^{J/\psi})$. The weight of each candidate event is given by:

$$1/w_i = \epsilon_{\text{L1}}(p_T^{\mu 1}) \cdot \epsilon_{\text{L2}}(p_T^{\mu 2}) \cdot \epsilon_{\chi^2 < 9}(p_T^{\mu 1}) \cdot$$

$$\epsilon_{\chi^2 < 9}(p_T^{\mu 2}) \cdot \mathcal{A}(p_T^{J/\psi}, y^{J/\psi}). \tag{5.1}$$

The invariant mass distributions of the weighted events are fitted, using the same shapes for signal and background as shown in Fig. 3.2, 3.3, 3.4 and 3.5. The number of signal events in each transverse momentum bin is determined from the

area under the signal mass peak.

The uncertainty on the weighted yield from the mass template fit, $N(p_T)_{\text{weighted}}$ is given by:

$$\delta(N(p_T)_{weighted}) = \sqrt{\sum_{i=0}^{i=N_s} (w_i)^2},\qquad(5.2)$$

where N_s is the raw number of signal events in each momentum bin before weighting. In a similar fashion, the di-muon p_T distribution in each bin is weighted. The weighed p_T distribution of the mass sideband subtracted events in the J/ψ mass signal region is used to determine the mean p_T value for each transverse momentum bin.

The J/ψ differential cross section is then calculated as follows:

$$\frac{d\sigma}{dp_T} \cdot Br(J/\psi \to \mu^+\mu^-) = \frac{N(p_T)_{\text{weighted}} \cdot (1 - \mathcal{A}')}{\epsilon_{\text{rec}} \cdot \int Ldt \cdot \Delta p_T},\qquad(5.3)$$

where $d\sigma/dp_T$ is the average cross section of inclusive J/ψ in that p_T bin integrated over $|y(J/\psi)| < 0.6$, $\mathcal{A}'$ is the correction factor for y smearing defined by Equation 4.2, ϵ_{rec} is the combined Level 3 and offline tracking and muon reconstruction efficiency, $\int \mathcal{L}dt$ dt is the integrated luminosity, and Δp_T is the size of the p_T bin. The cross-section values obtained with statistical and p_T-dependent uncertainties are listed in Table 5.1.

An uncertainty of +0.1% on the momentum scale is extracted by comparing the reconstructed J/ψ mass as shown in Fig. 5.1 to the world averaged value of 3.09688 ± 0.00004 GeV/c [29]. The 3 MeV/c^2 difference is attributed to an

$p_T(J/\psi)(\text{ GeV}/c)$	Mean p_T	Mean p_T^2	$\dfrac{d\sigma}{dp_T}\cdot\text{Br}[\text{nb}/(\text{ GeV}/c)]$	$\dfrac{d\sigma}{dp_T^2}\text{Br}[\text{nb}/(\text{ GeV}/c^2)]$
0.0 ± 0.25	0.15	0.027	$9.13 \pm 0.6\text{(stat)}\ ^{+1.1}_{-0.7}\text{(syst)}$	$36.5 \pm 2.4\text{(stat)}\ ^{+4.2}_{-2.6}\text{(syst)}$
0.25 ± 0.5	0.39	0.16	$28.1 \pm 1.5\ ^{+2.4}_{-1.6}$	$37.4 \pm 2.0\ ^{+3.1}_{-2.0}$
0.5 ± 0.75	0.64	0.42	$45.3 \pm 1.9\ ^{+3.0}_{-2.1}$	$36.2 \pm 1.5\ ^{+2.5}_{-1.8}$
0.75 ± 1.0	0.89	0.79	$59.3 \pm 2.0\ ^{+4.0}_{-2.9}$	$33.9 \pm 1.1\ ^{+2.3}_{-1.6}$
1.0 ± 1.25	1.13	1.29	$69.6 \pm 1.9\ ^{+3.6}_{-3.2}$	$31.0 \pm 0.8\ ^{+1.7}_{-1.5}$
1.25 ± 1.5	1.38	1.91	$73.4 \pm 1.7\ ^{+3.9}_{-3.5}$	$26.7 \pm 0.6\ ^{+1.4}_{-1.3}$
1.5 ± 1.75	1.63	2.66	$75.2 \pm 1.6\ ^{+3.8}_{-3.3}$	$23.2 \pm 0.5\ ^{+1.2}_{-1.0}$
1.75 ± 2.0	1.87	3.52	$72.9 \pm 1.4\ ^{+3.7}_{-3.3}$	$19.4 \pm 0.4\ ^{+0.9}_{-0.8}$
2.0 ± 2.25	2.13	4.53	$69.1 \pm 0.8\ ^{+3.3}_{-2.9}$	$16.3 \pm 0.2\ ^{+0.8}_{-0.7}$
2.25 ± 2.5	2.38	5.65	$67.3 \pm 1.0\ ^{+3.1}_{-2.8}$	$14.2 \pm 0.2\ ^{+0.7}_{-0.6}$
2.5 ± 2.75	2.62	6.89	$57.6 \pm 0.9 \pm 2.6$	$11.0 \pm 0.2 \pm 0.5$
2.75 ± 3.0	2.87	8.26	$52.0 \pm 0.8 \pm 2.4$	$9.04 \pm 0.13 \pm 0.41$
3.0 ± 3.25	3.12	9.76	$43.6 \pm 0.7 \pm 1.9$	$6.97 \pm 0.10 \pm 0.31$
3.25 ± 3.5	3.38	11.4	$37.3 \pm 0.6 \pm 1.6$	$5.53 \pm 0.08 \pm 0.24$
3.5 ± 3.75	3.62	13.1	$31.5 \pm 0.5 \pm 1.3$	$4.34 \pm 0.07 \pm 0.18$
3.75 ± 4.0	3.87	15.0	$26.2 \pm 0.4 \pm 1.2$	$3.38 \pm 0.05 \pm 0.15$
4.0 ± 4.25	4.12	17.0	$22.5 \pm 0.4 \pm 1.0$	$2.72 \pm 0.05 \pm 0.12$
4.25 ± 4.5	4.38	19.2	$18.7 \pm 0.3 \pm 0.8$	$2.13 \pm 0.04 \pm 0.09$
4.5 ± 4.75	4.62	21.4	$16.1 \pm 0.3 \pm 0.7$	$1.74 \pm 0.03 \pm 0.08$
4.75 ± 5.0	4.88	23.8	$13.3 \pm 0.3 \pm 0.6$	$1.37 \pm 0.03 \pm 0.06$
5.0 ± 5.5	5.24	27.5	$10.3 \pm 0.15 \pm 0.42$	$0.984 \pm 0.014 \pm 0.040$
5.5 ± 6.0	5.74	33.0	$7.28 \pm 0.12 \pm 0.29$	$0.633 \pm 0.010 \pm 0.025$
6.0 ± 6.5	6.24	38.9	$5.11 \pm 0.09 \pm 0.20$	$0.408 \pm 0.0069 \pm 0.016$
6.5 ± 7.0	6.74	45.5	$3.54 \pm 0.07 \pm 0.14$	$0.262 \pm 0.0052 \pm 0.010$
7.0 ± 8.0	7.45	55.7	$2.27 \pm 0.03 \pm 0.10$	$0.151 \pm 0.0019 \pm 0.006$
8.0 ± 9.0	8.46	71.6	$1.14 \pm 0.02 \pm 0.05$	$0.0668 \pm 0.0011 \pm 0.0028$
9.0 ± 10.0	9.46	89.5	$0.622 \pm 0.013 \pm 0.025$	$0.0327 \pm 0.0007 \pm 0.0013$
10.0 ± 12.0	10.8	118	$0.278 \pm 0.006 \pm 0.011$	$0.0126 \pm 0.0003 \pm 0.0005$
12.0 ± 14.0	12.8	165	$0.103 \pm 0.003 \pm 0.004$	$0.00398 \pm 0.00013 \pm 0.00015$
14.0 ± 17.0	15.2	233	$0.037 \pm 0.002 \pm 0.002$	$0.00120 \pm 0.00005 \pm 0.00006$
17.0 ± 20.0	18.3	336	$0.014 \pm 0.001 \pm 0.001$	$0.00037 \pm 0.00004 \pm 0.00002$

Table 5.1: The differential J/ψ cross section times the branching fraction Br $\equiv$ Br($J/\psi \to \mu\mu$) as a function of p_T for $|y(J/\psi)| < 0.6$. For each measurement, the first uncertainty is statistical and the second uncertainty is systematic. The systematic uncertainties shown are the p_T dependent uncertainties only. The fully correlated p_T independent systematic uncertainty in each bin is 7%.

underestimation of the energy loss in the silicon detector due to an incomplete accounting of the material at the time the data sample used in this analysis was processed. The +0.1% uncertainty from the momentum scale corresponds to an uncertainty on the differential cross section as $d(d\sigma/dp_T)/dp_T \times 0.1\%$. Using the values in Table 5.1, the first derivative of the differential cross section is calculated and the momentum scale uncertainty on the cross section in each bin estimated. The effect was found to be small, the largest negative deviation being -0.08% and the largest positive deviation being +0.7%.

Table 4.2 summarizes the different contributions to the systematic errors applied to the cross-section measurement from acceptance calculations using a Monte Carlo simulation, the mass line shapes used to determine the yield, the trigger and reconstruction efficiencies, and the luminosity measurement.

The differential cross-section results with systematic and statistical uncertainties are displayed in Fig. 5.2. The invariant cross section, $d\sigma/dp_T \cdot Br(J/\psi \to \mu\mu)$, with systematic errors is shown in Fig. 5.3. The results are also listed in Table 4.2.

To obtain the total J/ψ production cross section, the differential cross section is integrated over the p_T range. The integral J/ψ cross section times the branching

ratio $\mathrm{Br}(J/\psi \to \mu\mu)$ is found to be

$$\sigma[p\bar{p} \to J/\psi X, |y(J/\psi)| < 0.6] \cdot \mathrm{Br}(J/\psi \to \mu\mu)$$

$$= 240 \pm 1(\mathrm{stat})^{+21}_{-19}(\mathrm{syst}) \text{ nb.} \tag{5.4}$$

The p_T-dependent systematic uncertainties are summed and then added in quadrature with

$$\delta^{\mathrm{stat}}_{\mathrm{tot}\sigma\cdot\mathrm{rmBr}} = \sqrt{\sum_{i=1}^{N_{\mathrm{bins}}} \left(\delta^{\mathrm{stat}}_i\right)^2} = 1 \text{ nb,} \tag{5.5}$$

$$\delta^{\mathrm{syst}}_{\mathrm{tot}\sigma\cdot\mathrm{rmBr}} = \left\{\sum_{i=1}^{N_{\mathrm{bins}}} \delta^{\mathrm{syst}}_i(p_T)\right\} \oplus \pm16 =^{+21}_{-19} \text{ nb,} \tag{5.6}$$

the fully-correlated uncertainty of 6.9%: where N_{bins} is the total number of p_T bins, δ^{stat}_i is the statistical uncertainty in the cross-section measurement in the ith bin, $\delta^{\mathrm{syst}}_i(p_T)$ is the systematic uncertainty on the measurement in each p_T bin independent of the correlated systematic uncertainty of 6.9%, and $\oplus$ denotes addition in quadrature. After correcting for the $\mathrm{Br}(J/\psi \to \mu\mu) = 5.88 \pm 0.10\%$ [29], the cross section is found to be

$$\sigma[p\bar{p} \to J/\psi X, |y(J/\psi)| < 0.6]$$

$$= 4.08 \pm 0.02(\mathrm{stat})^{+0.36}_{-0.33}(\mathrm{syst}) \ \mu\mathrm{b.} \tag{5.7}$$

To compare with prior measurements where only the portion of the cross section for $p_T(J/\psi)$ exceeding 5 GeV/c was measured [41–43], the integrated cross

section of inclusive J/ψ with $p_T >5$ GeV/c and $|\eta| < 0.6$ at $\sqrt{s} =1960$ GeV is also measured. The cross section is found to be

$$\sigma[p\bar{p} \rightarrow J/\psi X, p_T(J/\psi) > 5.0 \text{ GeV}/c, |\eta(J/\psi)| < 0.6]$$

$$\cdot \text{BR}(J/\psi \rightarrow \mu\mu)$$

$$= 16.3 \pm 0.1(\text{stat})^{+1.4}_{-1.3}(\text{syst}) \text{ nb}. \tag{5.8}$$

The comparison of this result with earlier data is discussed in Chapter 7.
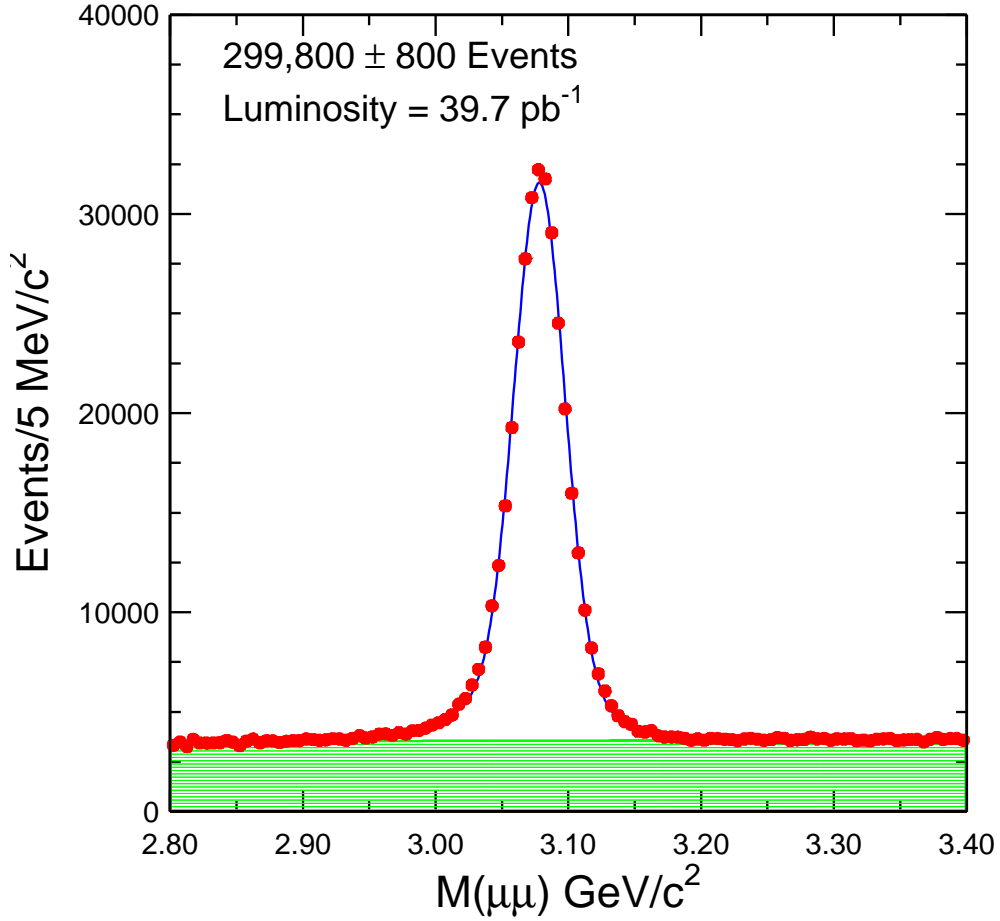
Figure 5.1: Invariant mass distribution of reconstructed dimuon J/ψ candidates. The points with error bars are data. The solid line is the fit to the signal shape using a double Gaussian and a linear fit for the background. The shaded histogram is the fitted background shape. The fit gives a signal of 299800 ± 800 J/ψ events with an averaged mass of 3.09391 ± 0.00008 GeV/c^2 obtained and an average width of 0.020 ± 0.001 GeV/c^2 mainly due to detector resolution. The uncertainties here are statistical only.
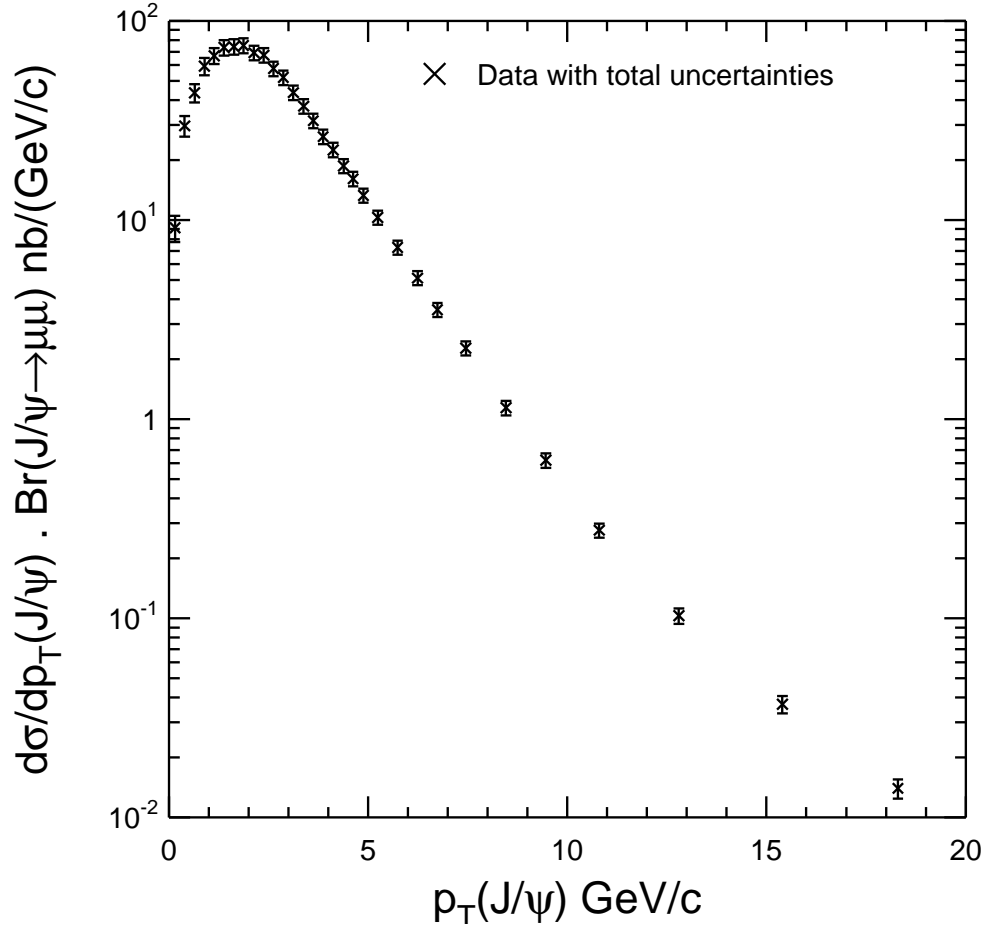
Figure 5.2: Inclusive J/ψ cross section, $d\sigma/dp_T \cdot Br(J/\psi \to \mu\mu)$, as a function of $J/\psi\, p_T$ integrated over the rapidity range $|y| < 0.6$. The differential cross section with systematic and statistical uncertainties added is plotted. This includes correlated uncertainties.
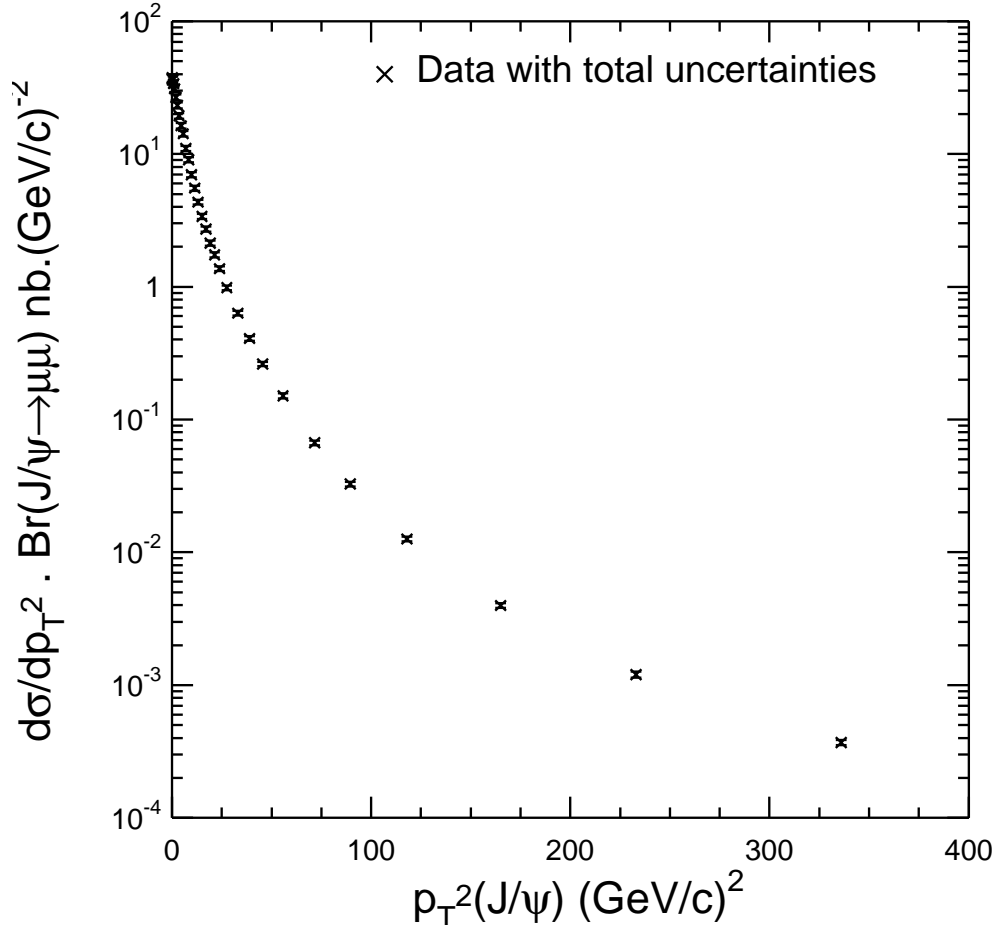
Figure 5.3: The invariant J/ψ cross section, $d\sigma/dp_T^2 \cdot Br(J/\psi \to \mu\mu)$, as a function of $J/\psi \, p_T^2$. The differential cross section with statistical and systematic uncertainties added is plotted. This includes correlated uncertainties.

Chapter 6

$H_b \rightarrow J/\psi$ FRACTION AND THE

b-HADRON CROSS SECTION

In general, the inclusive J/ψ cross section contains contributions from various sources:

- prompt production of J/ψ ,

- decays of excited charmonium states such as $\psi(2S), \chi_{c1}$ and χ_{c2},

- decays of b-hadrons.

The charmonium states decay immediately. In contrast, b-hadrons have long lifetimes that are on the order of pico seconds for the decay of the b-hadrons to the J/ψ mediated by weak interaction $b \rightarrow cW$. This implies that J/ψ events from the decays of b-hadrons are likely to be displaced from the beamline with measurable

size. This feature with precise vertex detector such as SVX II, make it possible to separate J/ψ of the decay products of b-hadrons from prompt charmonium states.

In the J/ψ cross section measurement, SVX II information is not needed and the tracks of the muons may or may not have it. On the other hand, an accurate vertex position where J/ψ is decayed, is needed to separate decay products of b-hadrons, and SVX II information is needed. For the J/ψ sample used for the measurement of the fraction, both muon tracks from the J/ψ decay must satisfy high quality COT-SVX II track requirement in addition to the requirements to the sample used in the J/ψ cross section measurement. The total number of hits expected in the five layers of the SVX II is determined from the number of functioning and powered silicon sensors intersected by the COT muon track. Tracks missing more than one expected hit in the SVX II are rejected. Both tracks are required to have a hit in the innermost layer of the SVX II and a hit in the second layer if the sensor intersected by the COT track is functioning. Corrections for energy loss in the SVX II are applied to the candidate muons based on a GEANT simulation of the material. Since the two muons are supposed to be the decay products of $J/\psi \rightarrow \mu^+\mu^-$, the two muon tracks are constrained to come from a common space point. The χ^2 probability of this 3-dimensional vertex fit is required to exceed 0.001. It is found that 139200 ± 500 events, or about half of the total J/ψ data sample, pass these criteria. While the data sample is reduced by the SVX II requirements, the momentum, angle, and vertex resolutions are

substantially improved.

The primary vertex, taken as the beam position in the $r - \phi$ plane, is assumed as the point where b-hadrons are produced. It is calculated on a run-by-run basis from a data sample taken using the inclusive jet trigger which has negligible contributions from charm and bottom decays so the beamline position can be calculated with no bias from detached decay vertices. The resolution of the primary vertex in the $r - \phi$ plane is limited by the ~30 μm rms spread in the size of the beam envelope.

6.1 Measurement of the Fraction of J/ψ Events from b-hadrons

Since b-hadrons have long life time, the J/ψ from the decay $H_b \rightarrow J/\psi X$ is likely to be displaced from the primary vertex where $p\bar{p}$ collision is happened. And the J/ψ is decayed immediately, the signed projection of the flight distance of J/ψ on its transverse momentum, "L_{xy}", is a good measurement of the displaced vertex and can be used as a variable to separate J/ψ of the H_b decay products from that of prompt decays. This method works well for events with high p_T J/ψ where the flight direction aligns well with that of the b-hadron. For events with very low p_T J/ψ, the non-negligible amount of J/ψ with large opening angle between its flight direction and that of the b-hadron will impair the separation ability. Monte Carlo

simulation shows that a reliable b-fraction can be extracted using this method for events with J/ψ p_T greater than 1.25 GeV/c.

The L_{xy} is calculated as

$$L_{xy}(J/\psi) = \vec{X} \cdot \vec{p}_T(J/\psi)/|p_T(J/\psi)|, \qquad (6.1)$$

where $\vec{X}$ is the vector from the primary vertex to the secondary vertex where the J/ψ decays to di-muon pair in the $r - \phi$ plane and $\vec{p}_T(J/\psi)$ is the transverse momentum vector. Another variable ct, called "proper decay length", which defined as

$$ct = L \cdot \frac{1}{\beta\gamma} = L_{xy}(b\text{-hadron}) \cdot M(b\text{-hadron})/p_T(b\text{-hadron}), \qquad (6.2)$$

is generally used for b-hadron lifetime measurement. However, $M(b\text{-hadron})$ and $p_T(b\text{-hadron})$ are unknown in this analysis. Instead of the ct, to reduce the dependence on the J/ψ transverse momentum bin size and placement, a new variable x, called "pseudoproper decay length", is used in this analysis and defined as

$$x = L_{xy}(J/\psi) \cdot M(J/\psi)/p_T(J/\psi), \qquad (6.3)$$

where the $M(J/\psi)$ is taken as the known J/ψ mass [29].

A distribution of the "pseudoproper decay length" of the J/ψ from b-hadron decay is unknown, and a Monte Carlo simulation is needed to model the distribution of $x(J/\psi)$ from b-hadron events. The Monte Carlo templates of the x distributions $X_{\mathrm{MC}}(x, p_T^{J/\psi})$ are generated for all J/ψ transverse momentum ranges, and

are directly convoluted with the value of the x resolution function measured in the data without allowing any of the parameters governing the shape of the Monte Carlo distributions to vary.

6.1.1   The Likelihood Function

An unbinned maximum likelihood fit is used to extract the b-fraction f_B, fraction of J/ψs which are decay products of b-hadron , from the data. The J/ψ pseudo-proper decay time x, its error σ, and the mass of the di-muon pair $m_{\mu\mu}$ are the input variables to the likelihood. The mass and lifetime of each event is simultaneously fitted by a log-likelihood function (ln$\mathcal{L}$) which is defined as

$$\ln \mathcal{L} = \sum_{i=1}^{N} \ln \mathcal{F}(x, m_{\mu\mu}), \qquad (6.4)$$

where N is the total number of events in the mass range $2.85 < m_{\mu\mu} < 3.35$ GeV/c^2.

The mass and pseudoproper decay time distribution is described by the following function,

$$\mathcal{F}(x, m_{\mu\mu}) = f_{\text{Sig}} \times \mathcal{F}_{\text{Sig}}(x) \times \mathcal{M}_{\text{Sig}}(m_{\mu\mu})$$

$$+ (1 - f_{\text{Sig}}) \times \mathcal{F}_{\text{Bkg}}(x) \times \mathcal{M}_{\text{Bkg}}(m_{\mu\mu}) \qquad (6.5)$$

where f_{Sig} is the fraction of signal J/ψ events in the mass region, $\mathcal{F}_{\text{Sig}}$ and $\mathcal{F}_{\text{Bkg}}$ are the functional forms describing the J/ψ pseudoproper decay time distribution for

the signal and background events respectively, and $\mathcal{M}_{\text{Sig}}$ and $\mathcal{M}_{\text{Bkg}}$ are the functional forms describing the invariant mass distributions for the signal and background events respectively. These components of the likelihood fit is described below in more detail below.

The function for modeling the J/ψ pseudoproper decay time signal distribution consists of two parts, the $H_b \rightarrow J/\psi X$ decay part which labeled $\mathcal{F}_B(x)$, and prompt decay part labeled $\mathcal{F}_P(x)$, respectively. Then $\mathcal{F}_{\text{Sig}}$ is expressed as

$$\mathcal{F}_{\text{Sig}}(x) = [f_B \cdot \mathcal{F}_B(x) + (1 - f_B) \cdot \mathcal{F}_P(x)], \tag{6.6}$$

where f_B is the fraction of J/ψ mesons originating in b-hadron decays. The x distributions $\mathcal{X}_{MC}$ of accepted events from a Monte Carlo simulation is used as templates for the x distribution of b-hadron events in data. The generated distributions are convoluted with a resolution function $R(x' - x, s\sigma)$ such that the $H_b \rightarrow J/\psi X$ signal shape is given by

$$\mathcal{F}_B(x) = R(x' - x, s\sigma) \otimes \mathcal{X}_{\text{MC}}(x') \tag{6.7}$$

where s is an overall error scale factor which represents the possible errors in determining the lifetime resolution and *otimes* denotes a convolution. Prompt J/ψ mesons are produced at the primary vertex, therefore their observed displacement is described only by the resolution function $\mathcal{F}_P = R(x, s\sigma)$. It is found that $R(x' - x, s\sigma)$ is best described by a sum of two Gaussian distributions centered at $x = 0$.

The background requires a more complicated parameterization to obtain a

good fit to the data outside the J/ψ signal region. The pseudoproper decay time background function is composed of four parts: the zero lifetime component, a positive slope exponential function, a negative slope exponential function, and a symmetric exponential function with both positive and negative slopes. The positive slope exponential function is chosen to model the background from other long lived b-hadron events that produce opposite sign muons such as $b \to c\mu^-\bar{\nu}X$, $c \to \mu^+\nu X$. The zero lifetime component is chosen to be the same shape as the resolution function. The symmetric and negative slope exponential functions are added to parameterize the remaining components of the background pseudoproper decay time distributions which are from unknown sources. The background exponential tails are also convoluted with the resolution function.

The background functional form is parameterized as follows:

$$\mathcal{F}_{\text{Bkg}}(x) = (1 - f_+ - f_- - f_{\text{sym}})R(x, s\sigma) \tag{6.8}$$

$$+ \frac{f_+}{\lambda_+} \exp\left(-\frac{x'}{\lambda_+}\right)\theta(x') \otimes R(x' - x, s\sigma)$$

$$+ \frac{f_-}{\lambda_-} \exp\left(\frac{x'}{\lambda_-}\right)\theta(-x') \otimes R(x' - x, s\sigma)$$

$$+ \frac{f_{\text{sym}}}{2\lambda_{\text{sym}}} \exp\left(-\frac{x'}{\lambda_{\text{sym}}}\right)\theta(x') \otimes R(x' - x, s\sigma)$$

$$+ \frac{f_{\text{sym}}}{2\lambda_{\text{sym}}} \exp\left(\frac{x'}{\lambda_{\text{sym}}}\right)\theta(-x') \otimes R(x' - x, s\sigma), \tag{6.9}$$

where $f_{\pm,\text{sym}}$ is the fraction of the background distribution in the positive, negative and symmetric exponential tails respectively, $\lambda_{\pm,\text{sym}}$ are the corresponding exponential slopes, and $\theta(x)$ is the step function defined as $\theta(x) = 1$ for $x \geq 0$ and

$\theta(x) = 0$ for $x < 0$. It should be kept in mind that the background strongly depends on p_T and $m_{\mu\mu}$, and that the likelihood function incorporates a global fit over the full mass window shown in Fig. 3.2, Fig. 3.3, Fig. 3.4 and Fig. 3.5, including the J/ψ peak and mass sidebands.

The mass resolution used in the likelihood fit is better than that shown in Figs. 3.2 - 3.5 because of the addition of SVX II hits to the tracks. For the likelihood fit, the di-muon mass shape $\mathcal{M}_{\text{Sig}}$ is chosen to be simply the sum of two Gaussian distributions. The means of the Gaussian distributions are allowed to float independently:

$$\mathcal{M}_{\text{Sig}}(m_{\mu\mu}) = G_1(m_{\mu\mu} - M, \sigma_M)$$
$$+ f_2 \cdot G_2[m_{\mu\mu} - (M + D), r_2\sigma_M]. \tag{6.10}$$

The mass fit parameters are the mean M of the mass distribution, the width σ_M of the first Gaussian distribution, the fraction f_2 of the second Gaussian distribution, the shift D in the mean of the second Gaussian distribution, and the ratio r_2 of the widths of the two Gaussian distributions. The mass background is modeled using a linear distribution. This fit is adequate for the SVX II constrained di-muon mass. The function used, normalized to unity over the mass range m^{min} to m^{max}, is

$$\mathcal{M}_{\text{Bkg}}(m_{\mu\mu}) = \frac{1}{m_{\mu\mu}^{\text{max}} - m_{\mu\mu}^{\text{min}}}$$
$$+ M_{\text{slope}} \left(m_{\mu\mu} - \frac{m_{\mu\mu}^{\text{max}} + m_{\mu\mu}^{\text{min}}}{2} \right), \tag{6.11}$$

where M_{slope} is the slope of the mass background distribution. The only fit parameter is M_{slope}.

6.1.2 The Fits and Systematic Uncertainties

The distribution of the J/ψ pseudoproper decay time and fits to the distributions in three J/ψ p_T ranges are shown in Fig. 6.1, Fig. 6.2 and Fig. 6.3. The distribution of the di-muon invariant mass correspond to these J/ψ p_T ranges without SVX II hits requirements are shown in Fig. 3.3, Fig. 3.4 and Fig. 3.5. Table 6.1 shows the b-fractions obtained from the fit in each J/ψ p_T bin from 1.25 - 1.5 GeV/c to 17.0 - 20.0 GeV/c, with statistical and systematic uncertainties. And the Fig. 6.4 shows the distribution of the distribution of the b-fraction as a function of J/ψ p_T. The inclusive b-hadron cross section is calculated from these fit results with the inclusive J/ψ cross section in Section 6.2

6.2 Measurement of the Inclusive b-hadron Cross Section

Since J/ψ mesons from decays of b-hadrons have a different average spin alignment than an inclusive sample of J/ψ mesons, an acceptance correction must be appied to account for this difference, while the J/ψ yields and efficiencies estimated for the J/ψ cross section are able to used for b-hadron cross section. In

$p_T(J/\psi)$	Fraction from	Acceptance
GeV/c	b-hadrons	$H_b \rightarrow J/\psi X$
1.25 - 1.5	$0.094 \pm 0.010 \pm 0.012$	0.01579 ± 0.00037
1.5 - 1.75	$0.092 \pm 0.006 \pm 0.010$	0.01981 ± 0.00029
1.75 -2.0	$0.085 \pm 0.006 \pm 0.009$	0.02433 ± 0.00034
2.0 - 2.25	$0.100 \pm 0.005 \pm 0.011$	0.02842 ± 0.00032
2.25 - 2.5	$0.091 \pm 0.005 \pm 0.010$	0.03335 ± 0.00038
2.5 - 2.75	$0.101 \pm 0.005 \pm 0.009$	0.03864 ± 0.00059
2.75 - 3.0	$0.099 \pm 0.005 \pm 0.008$	0.04376 ± 0.00072
3.0 - 3.25	$0.109 \pm 0.005 \pm 0.007$	0.04940 ± 0.00081
3.25 - 3.5	$0.112 \pm 0.005 \pm 0.008$	0.05619 ± 0.00093
3.5 - 3.75	$0.113 \pm 0.005 \pm 0.007$	0.0611 ± 0.0010
3.75 - 4.0	$0.133 \pm 0.005 \pm 0.007$	0.0666 ± 0.0016
4.0 - 4.25	$0.116 \pm 0.005 \pm 0.007$	0.0736 ± 0.0018
4.25 - 4.5	$0.126 \pm 0.006 \pm 0.007$	0.0815 ± 0.0020
4.5 - 4.75	$0.131 \pm 0.006 \pm 0.007$	0.0891 ± 0.0022
4.75 - 5.0	$0.147 \pm 0.007 \pm 0.008$	0.0960 ± 0.0024
5.0 - 5.5	$0.141 \pm 0.005 \pm 0.006$	0.1065 ± 0.0025
5.5 - 6.0	$0.156 \pm 0.006 \pm 0.007$	0.1198 ± 0.0029
6.0 - 6.5	$0.169 \pm 0.007 \pm 0.007$	0.1330 ± 0.0032
6.5 - 7.0	$0.182 \pm 0.007 \pm 0.008$	0.1476 ± 0.0037
7.0 - 8.0	$0.208 \pm 0.006 \pm 0.009$	0.1647 ± 0.0055
8.0 - 9.0	$0.227 \pm 0.009 \pm 0.007$	0.1813 ± 0.0062
9.0 - 10.0	$0.250 \pm 0.011 \pm 0.008$	0.1893 ± 0.0068
10.0 - 12.0	$0.279 \pm 0.012 \pm 0.008$	0.2022 ± 0.0064
12.0 - 14.0	$0.337 \pm 0.019 \pm 0.009$	0.2247 ± 0.0072
14.0 - 17.0	$0.397 \pm 0.025 \pm 0.009$	0.2462 ± 0.011
17.0 - 20.0	$0.464 \pm 0.045 \,^{+0.017}_{-0.011}$	0.2538 ± 0.0093

Table 6.1: The fraction of J/ψ events from decays of b-hadrons and the corresponding acceptance. The first uncertainty on the b-fraction is the statistical uncertainty from the unbinned likelihood fit and the second uncertainty is the combined systematic uncertainties on the measurement of the b-fraction. The uncertainty on the acceptance is the combined statistical uncertainty from Monte Carlo statistics and the systematic uncertainty on the acceptance measurement.

CDF Run I measurements, the effective value of the spin alignment parameter α_{eff} of J/ψ from b-hadron decays was measured to be $\alpha_{\text{eff}}[(p_T(J/\psi) > 4.0\text{GeV}/c] = -0.09 \pm 0.10$ [15], where α_{eff} is obtained by fitting $\cos\theta_{J/\psi}$, the angle between the muon direction in the J/ψ rest frame and the J/ψ direction in the lab frame, by the functional form $1 + \alpha_{\text{eff}} \cdot \cos^2\theta_{J/\psi}$. More recent measurement on the spin alignment was done by using $B \to J/\psi X$ events collected at the $\Upsilon(4S)$ resonance. The *BaBar* experiment measured $\alpha_B = -0.196 \pm 0.044$ for $p^* < 1.1$ GeV/c and $\alpha_B = -0.592 \pm 0.032$ for $p^* > 1.1$ GeV/c [44]. Here the decay angle of the J/ψ is measured in the $\Upsilon(4S)$ rest frame and p^* is the total J/ψ momentum measured in the $\Upsilon(4S)$ rest frame.

The more precise result from the *BaBar* experiment is chosen in this analysis for the acceptance calculations for $H_b \to J/\psi X$ events, assuming it is applicable to the CDF environment where b-hadrons are produced in fragmentation with a large momentum range instead of produced at a fixed momentum as in Υ decays [45]. First, Monte Carlo events are generated to have the J/ψ helicity angle distributions in the b-hadron rest frame predicted from α_B values according to their p^* values. Then, values of the spin alignment parameter α_{eff} for events in each J/ψ p_T bin are obtained by fitting the $\cos\Theta_{J/\psi}$ distributions of these Monte Carlo events. The systematic uncertainties on α_{eff} are obtained by varying the input values of α_B in the process according to measurement uncertainties. This process gives a result consistent with previous CDF measurement, albeit with smaller uncertainties. For

example, a new and more precise value of $\alpha_{\mathrm{eff}} = -0.13 \pm 0.01$ for the J/ψ events with $p_T(J/\psi) > 4.0$ GeV/c is obtained from this process. Finally, the acceptance values, as listed in Table 6.1, are calculated from the Monte Carlo events generated with the derived spin alignment parameters in each J/ψ p_T bin.

The differential b-hadron cross sections as a funtion of J/ψ p_T are calculated in a similar way as that for the inclusive J/ψ. The J/ψ yields in each p_T bin estimated for J/ψ cross section listed in Table 3.2 are multiplied with the b-fractions to obtain the corresponding $H_b \rightarrow J/\psi$ yields of J/ψs from b-hadron decays. The new acceptance values listed in Table 6.1 are used while the J/ψ reconstruction efficiencies and luminosity value stay the same. Most of the systematic uncertainties in the inclusive J/ψ cross section calculation carry over here without change except for those from the J/ψ spin alignment on the acceptance which are estimated using uncertainties on α_{eff}. In addition, the uncertainties from the b-fractions also must be included in the systematic uncertainties. The J/ψ from b-hadron inclusive cross section results with statistical and systematic uncertainties are listed in Table 6.2. The differential cross section with all statistical and systematic uncertainties added is shown in Fig. 6.5. A recent QCD theoretical calculation using a fixed order (FO) calculation with resummation of next-to-leading logs (NLL) [13] is overlaid for a comparison. The comparison with theoretical calculations is further discussed in Chapter 7.

An integration of the differential b-hadron cross section results in Table 6.2

$p_T(J/\psi)$	$\langle p_T(J/\psi) \rangle$	$\dfrac{d\sigma}{dp_T} \cdot \mathrm{Br(nb/\,GeV/}c)$	$\dfrac{d\sigma}{dp_T} \cdot \mathrm{Br(nb/\,GeV/}c)$
(GeV/c)	(GeV/c)	J/ψ from b	Prompt J/ψ
1.25 - 1.5	1.38	$6.60 \pm 0.70\text{(stat)} \, ^{+0.77}_{-0.67}\text{(syst}_{p_T})$	$66.8 \pm 1.5\text{(stat)} \, ^{+9.2}_{-9.1}\text{(syst}_{p_T})$
1.5 - 1.75	1.63	$6.62 \pm 0.44 \, ^{+0.71}_{-0.62}$	$68.6 \pm 1.5 \, ^{+8.2}_{-8.0}$
1.75 - 2.0	1.87	$5.93 \pm 0.38 \, ^{+0.62}_{-0.56}$	$67.0 \pm 1.3 \, ^{+7.9}_{-7.7}$
2.0 - 2.25	2.13	$6.58 \pm 0.34 \, ^{+0.67}_{-0.56}$	$62.5 \pm 0.7 \, ^{+7.5}_{-7.4}$
2.25 - 2.5	2.38	$5.83 \pm 0.30 \, ^{+0.57}_{-0.50}$	$61.5 \pm 0.9 \, ^{+7.3}_{-7.2}$
2.5 - 2.75	2.62	$5.50 \pm 0.26 \, ^{+0.51}_{-0.45}$	$52.1 \pm 0.8 \pm 5.2$
2.75 - 3.0	2.87	$4.86 \pm 0.23 \, ^{+0.44}_{-0.38}$	$47.1 \pm 0.7 \pm 4.4$
3.0 - 3.25	3.12	$4.50 \pm 0.20 \, ^{+0.25}_{-0.21}$	$39.1 \pm 0.6 \pm 3.0$
3.25 - 3.5	3.38	$3.94 \pm 0.17 \, ^{+0.23}_{-0.18}$	$33.4 \pm 0.5 \pm 2.8$
3.5 - 3.75	3.62	$3.34 \pm 0.15 \, ^{+0.21}_{-0.16}$	$28.2 \pm 0.4 \pm 2.1$
3.75 - 4.0	3.87	$3.28 \pm 0.14 \pm 0.16$	$22.9 \pm 0.3 \pm 1.6$
4.0 - 4.25	4.12	$2.45 \pm 0.11 \pm 0.15$	$20.1 \pm 0.4 \pm 1.5$
4.25 - 4.5	4.38	$2.22 \pm 0.10 \pm 0.11$	$16.5 \pm 0.3 \pm 1.2$
4.5 - 4.75	4.62	$1.99 \pm 0.09 \pm 0.10$	$14.1 \pm 0.3 \pm 1.0$
4.75 - 5.0	4.88	$1.84 \pm 0.08 \pm 0.10$	$11.5 \pm 0.3 \pm 0.8$
5.0 - 5.5	5.24	$1.38 \pm 0.05 \pm 0.06$	$8.92 \pm 0.13 \pm 0.52$
5.5 - 6.0	5.74	$1.07 \pm 0.04 \pm 0.05$	$6.21 \pm 0.10 \pm 0.37$
6.0 - 6.5	6.24	$0.817 \pm 0.031 \pm 0.038$	$4.29 \pm 0.07 \pm 0.24$
6.5 - 7.0	6.74	$0.610 \pm 0.025 \pm 0.026$	$2.93 \pm 0.06 \pm 0.17$
7.0 - 8.0	7.45	$0.447 \pm 0.014 \pm 0.022$	$1.82 \pm 0.02 \pm 0.11$
8.0 - 9.0	8.46	$0.246 \pm 0.009 \pm 0.010$	$0.894 \pm 0.015 \pm 0.047$
9.0 - 10.0	9.46	$0.149 \pm 0.007 \pm 0.006$	$0.473 \pm 0.010 \pm 0.024$
10.0 - 12.0	10.8	$0.074 \pm 0.003 \pm 0.003$	$0.204 \pm 0.004 \pm 0.010$
12.0 - 14.0	12.8	$0.034 \pm 0.002 \pm 0.001$	$0.069 \pm 0.002 \pm 0.003$
14.0 - 17.0	15.4	$0.0143 \pm 0.0009 \pm 0.0007$	$0.023 \pm 0.001 \pm 0.001$
17.0 - 20.0	18.3	$0.0062 \pm 0.0006 \pm 0.0004$	$0.0078 \pm 0.0006 \pm 0.0006$

Table 6.2: The inclusive $H_b \rightarrow J/\psi X$ and prompt J/ψ differential cross sections as a function of transverse momentum of the J/ψ with statistical and p_T dependent systematic uncertainties. The cross section in each p_T bin is integrated over the rapidity range $|y(J/\psi)| < 0.6$. The fully correlated systematic uncertainty, $\text{syst}_{fc} = 6.9\%$, from the measurement of the inclusive J/ψ cross section needs to combined with the p_T dependent systematic uncertainties.

gives the total cross section

$$\sigma(p\bar{p} \to H_b X, p_T(J/\psi) > 1.25 \text{GeV}/c, |y(J/\psi)| < 0.6)$$

$$\cdot \text{Br}(H_b \to J/\psi X) \cdot \text{Br}(J/\psi \to \mu\mu)$$

$$= 19.4 \pm 0.3(\text{stat})^{+2.1}_{-1.9}(\text{syst}) \text{ nb}. \tag{6.12}$$

The systematic uncertainty quoted includes the fully correlated uncertainty of 6.9% obtained from the inclusive J/ψ cross section measurement. The integrated cross section extracted above is corrected for the branching fraction $\text{Br}(J/\psi \to \mu\mu) = 5.88 \pm 0.10\%$ [29] to obtain

$$\sigma(p\bar{p} \to H_b, H_b \to J/\psi, p_T(J/\psi) > 1.25 \text{GeV}/c, |y(J/\psi)| < 0.6)$$

$$= 0.330 \pm 0.005(\text{stat})^{+0.036}_{-0.033}(\text{syst})\mu\text{b}. \tag{6.13}$$

Also, the prompt J/ψ cross section is extracted by subtracting the cross section of $H_b \to J/\psi X$ from the inclusive J/ψ cross section. This calculation is applied to all J/ψ with $p_T > 1.25$ GeV/c where it is able to extract the b-fraction. The results are shown in Table 6.2 and in Fig. 6.6. The systematic uncertainties on the prompt J/ψ cross section are taken to be the uncertainties on the inclusive cross section added in quadrature with the uncertainties on the measured b-fractions. The integrated cross section of prompt J/ψ is found to be:

$$\sigma(p\bar{p} \to J/\psi_p X, p_T(J/\psi) > 1.25 \text{GeV}/c, |y(J/\psi)| < 0.6)$$

$$= 2.86 \pm 0.01(\text{stat})^{+0.34}_{-0.45}(\text{syst})\mu\text{b}, \tag{6.14}$$

where J/ψ_p denotes a prompt J/ψ and where the $J/\psi \to \mu\mu$ branching fraction is corrected.

The differential b-hadron cross section as a function of $p_T(H_b)$ is extracted from the measured differential cross sections of $H_b \to J/\psi X$ by utilizing the decay kinematics of charmonium produced in b-hadron decays. The procedure starts with the calculation of contributions to the cross section of b-hadrons in a given $p_T(H_b)$ bin from J/ψ events in the range $1.25 < p_T(J/\psi) < 20$ GeV/c, where the fractions of J/ψ mesons from b decays is measured. Since b-hadrons with p_T as little as 0 GeV/c can decay to J/ψ with p_T as large as 2.0 GeV/c, it is possible to extract b-hadron differential cross section $p_T(H_b)$ down to 0 GeV/c from the p_T range of measured J/ψ cross section. In the ith $p_T(H_b)$ bin of the cross section as a function of $p_T(H_b)$, the total contribution from the $p_T(J/\psi)$ bins of measured cross section as a function of $p_T(J/\psi)$ in the range 1.25 to 20 GeV/c, is labeled as the raw cross section σ_i(raw), and given by

$$\sigma_i(\text{raw}) = \sum_{j=1}^{N} w_{ij}\sigma_j(J/\psi), \qquad (6.15)$$

where $\sigma_j(J/\psi)$ is the cross section of J/ψ mesons from H_b in the jth $p_T(J/\psi)$ bin and w_{ij} is the fraction of H_b events in the ith $p_T(H_b)$ bin relative to the total in the jth $p_T(J/\psi)$ bin. The sum of the weights w_{ij} in each $p_T(J/\psi)$ bin is normalized to 1. In some $p_T(H_b)$ ranges, not all the J/ψ from b-hadron decay have transverse momentum and rapidity in the measured range $1.25 < p_T(J/\psi) < 20$ GeV/c and $|y(J/\psi)| < 0.6$. Thus, the raw cross section is corrected for the acceptance due to

101

the limited J/ψ kinematic range to obtain the differential b-hadron cross section, $\sigma_i(H_b)$, in the ith $p_T(H_b)$ bin,

$$\sigma_i(H_b) = \frac{\sigma_i(\text{raw})}{f^i_\sigma} = \frac{\sum_{j=1}^{N} w_{ij}\sigma_j(J/\psi)}{f^i_\sigma}, \tag{6.16}$$

where f^i_σ is the fraction of bottom hadrons in the ith $p_T(H_b)$ bin that decays to a J/ψ with a transverse momentum in the range 1.25 to 20 GeV/c and rapidity in the range $|y(J/\psi)| < 0.6$. Monte Carlo simulations are used to calculate the weighting factors, w_{ij}, and acceptance correction factors, f^i_σ. In the simulation, the decay spectrum of $H_b \rightarrow J/\psi X$ obtained from references [44,46] is used. The calculation is repeated in an iteration process: at each pass the input production spectrum used in the Monte Carlo is the spectrum measured in the previous iteration and a χ^2 comparison is made between the input and output spectrums. The process terminates when the χ^2 comparison reach the precision limit. This procedure is found to be insensitive to the initial production spectrum shape.

The statistical uncertainty in each $p_T(H_b)$ bin is given by:

$$\delta_{\text{stat}}(\sigma_i(H_b)) = \frac{1}{f^i_\sigma}\sqrt{\sum_{j=1}^{N} w_{ij}\delta^2_{\text{stat}}(\sigma_j(J/\psi))}. \tag{6.17}$$

The systematic uncertainties are taken as just the simple weighted sum of the systematic uncertainties from the differential $H_b \rightarrow J/\psi$ cross sections measurements,

$$\delta_{\text{stat}}(\sigma_i(H_b)) = \frac{1}{f^i_\sigma}\sum_{j=1}^{N} w_{ij}\delta_{\text{syst}}(\sigma_j(J/\psi)). \tag{6.18}$$

The extracted differential cross section of b-hadrons over the b-hadron transverse momentum range from 0 to 25 GeV/c is shown in Fig. 6.7. The cross section has been corrected for the branching fractions, Br($H_b \rightarrow J/\psi X$) = 1.16 ± 0.10% and Br($J/\psi \rightarrow \mu\mu$) = 5.88 ± 0.10% [29], and divided by two to obtain the single b-hadron differential cross section. The differential cross section extracted above is integrated over the transverse momentum range to obtain the single b-hadron inclusive cross section. The total inclusive single b-hadron cross section is found to be

$$\sigma(p\bar{p} \rightarrow H_b X, |y| < 0.6) = 17.6 \pm 0.4(\text{stat})^{+2.5}_{-2.3}(\text{syst})\mu\text{b}. \qquad (6.19)$$

Figure 6.1: Fits to the *J/ψ* pseudoproper decay time in the range $1.25 < p_T(\mu\mu) < 1.5$ GeV/c to extract the fraction of events from long-lived *b*-hadron decays. The solid line is the fit to all the events in the mass window of 2.85 to 3.35 GeV/c^2, the dashed line is the fit to all signal events, the solid histogram is the fit to the portion of the signal events that are from *b*-hadron decays and the dot-dashed line is the fit to background events including events in the invariant mass sidebands.
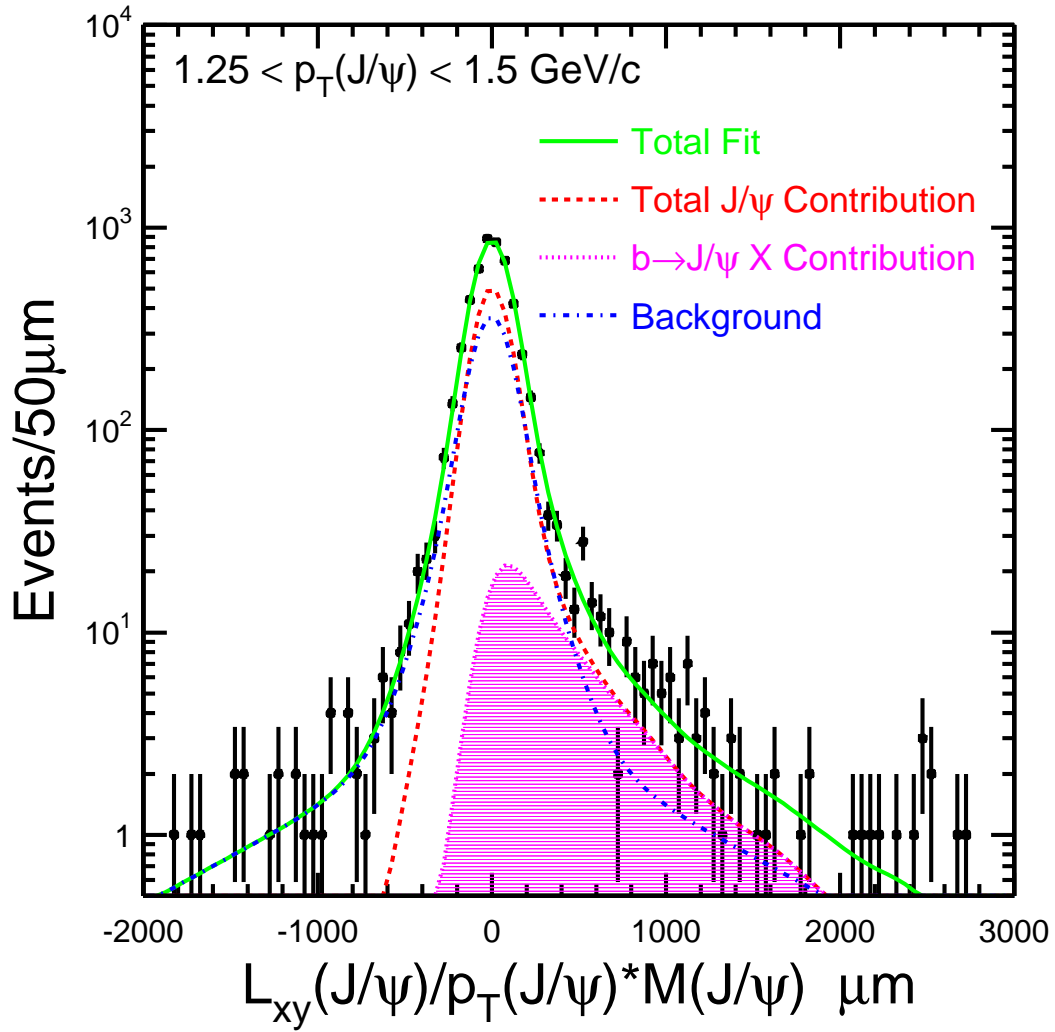
Figure 6.2: Fits to the *J/ψ* pseudoproper decay time in the range $5.0 < p_T(\mu\mu) <$ 5.5 GeV/*c* to extract the fraction of events from long-lived *b*-hadron decays. The solid line is the fit to all the events in the mass window, the dashed line is the fit to all signal events, the solid histogram is the fit to the portion of the signal events that are from *b*-hadron decays and the dot-dashed line is the fit to background events.
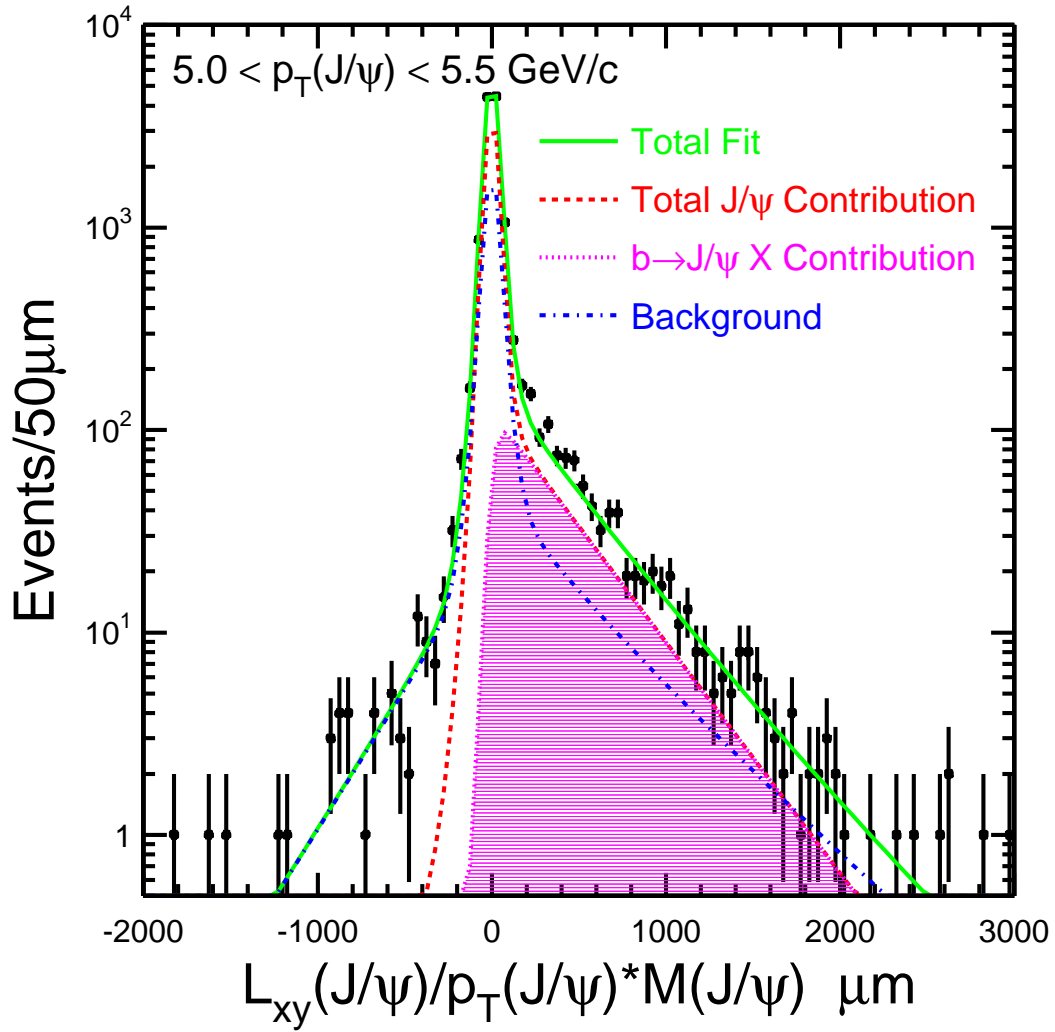
Figure 6.3: Fits to the *J/ψ* pseudoproper decay time in the range $12.0 < p_T(\mu\mu) < 14.0$ GeV/*c* to extract the fraction of events from long-lived *b*-hadron decays. The solid line is the fit to all the events in the mass window, the dashed line is the fit to all signal events, the solid histogram is the fit to the portion of the signal events that are from *b*-hadron decays and the dot-dashed line is the fit to background events.
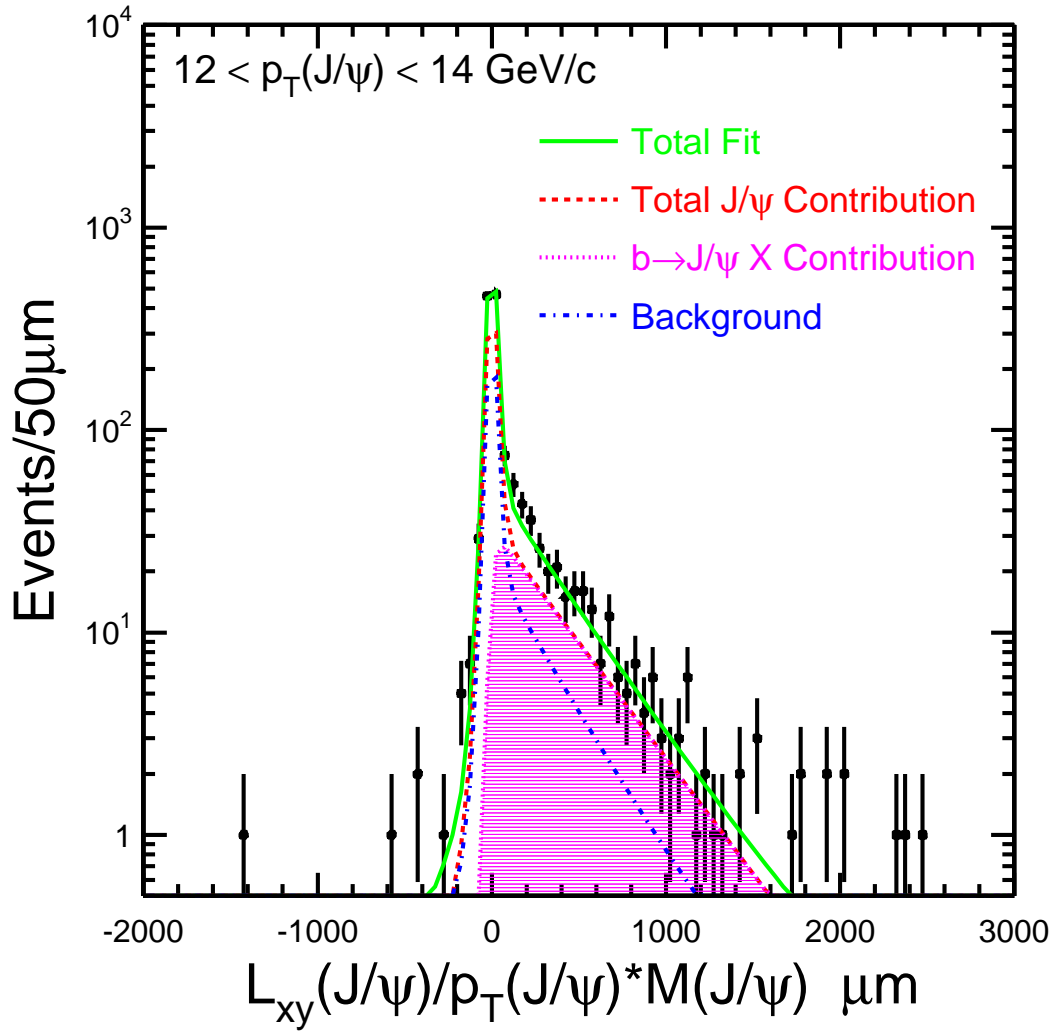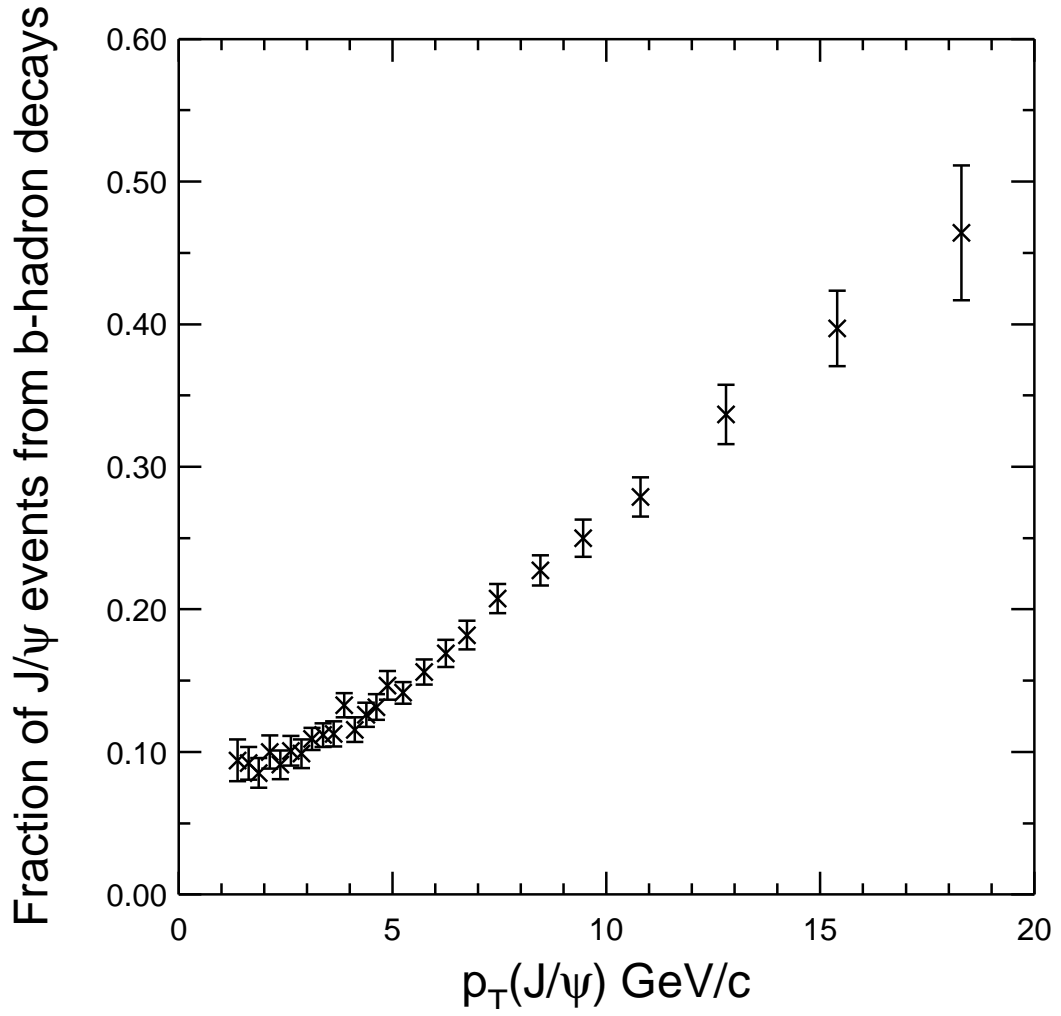
Figure 6.4: Fraction of *J/ψ* from *b*-hadron decays in the inclusive *J/ψ* events of Run-II data as a function of *J/ψ* transverse momentum. Error bars include both statistical and systematic errors.
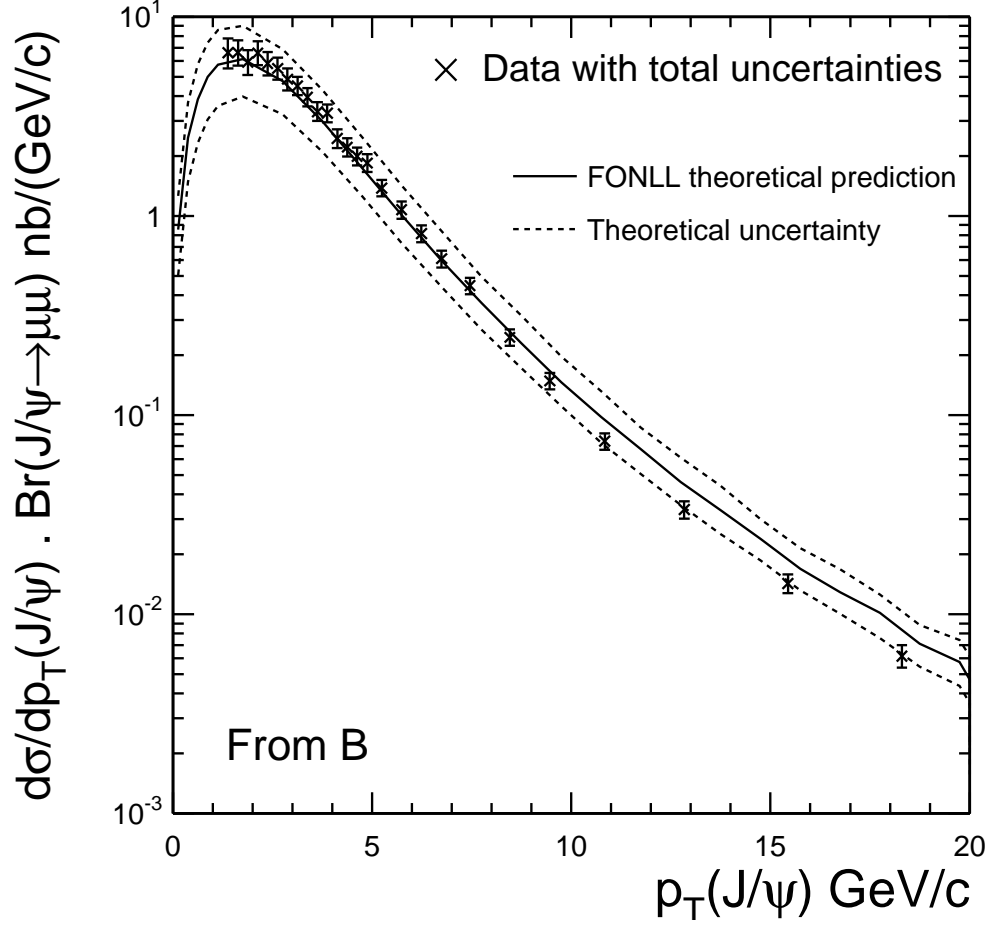
Figure 6.5: Differential cross-section distribution of J/ψ events from the decays of b-hadrons as a function of J/ψ transverse momentum integrated over the rapidity range $|y| < 0.6$. The crosses with error bars are the data with systematic and statistical uncertainties added including correlated uncertainties. The solid line is the central theoretical values using the FONLL calculations outlined in [13], the dashed line is the theoretical uncertainty.
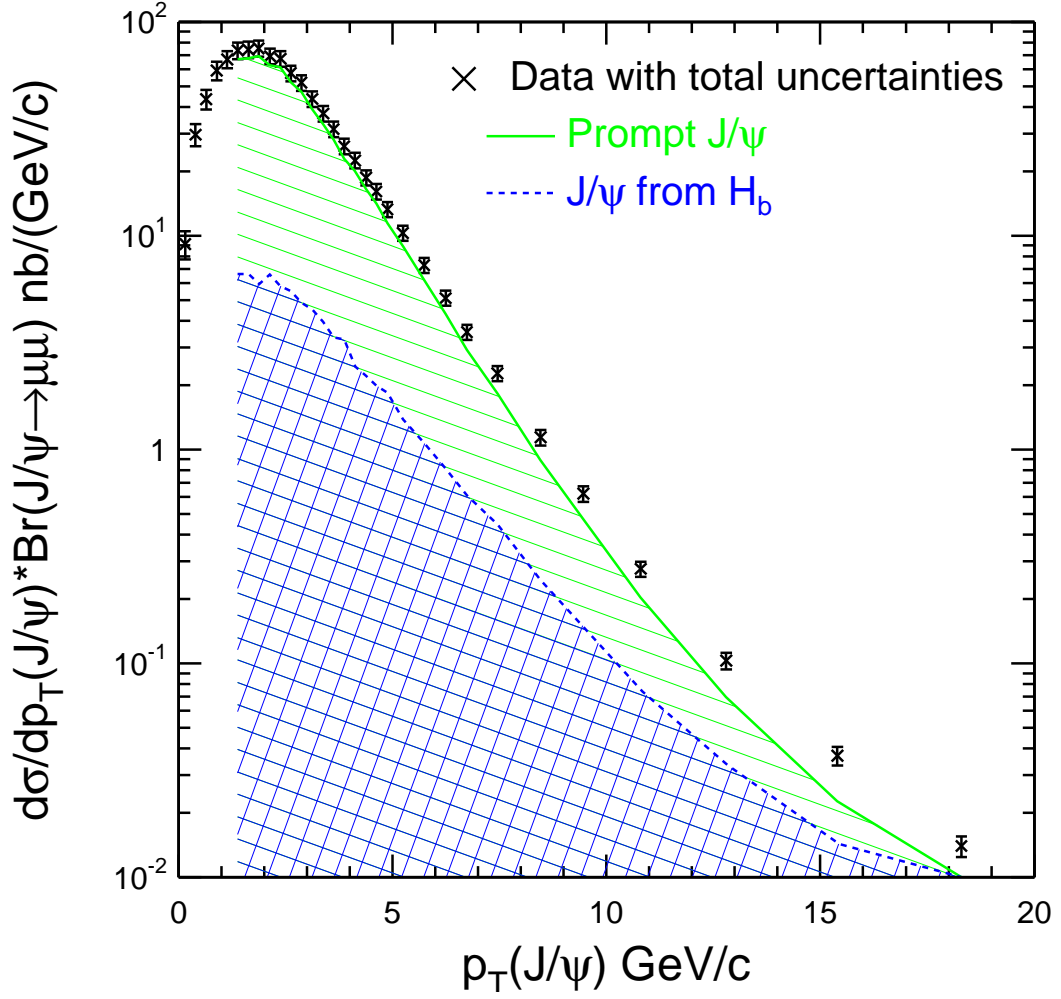
Figure 6.6: The inclusive J/ψ cross section as a function of J/ψ p_T integrated over the rapidity range $|y| < 0.6$ is plotted as points with error bars where all uncertainties have been added. The hatched histogram indicates the contribution to the cross section from prompt charmonium production. The cross-hatched histogram is the contribution from decays of b-hadrons.

Figure 6.7: Differential cross-section distribution of $\bar{b}$-hadron production as a function of b-hadron transverse momenta. The crosses with error bars are the data with systematic and statistical uncertainties added including correlated uncertainties. The solid line is the central theoretical values using the FONLL calculations outlined in [13], the dashed line is the theoretical uncertainty.
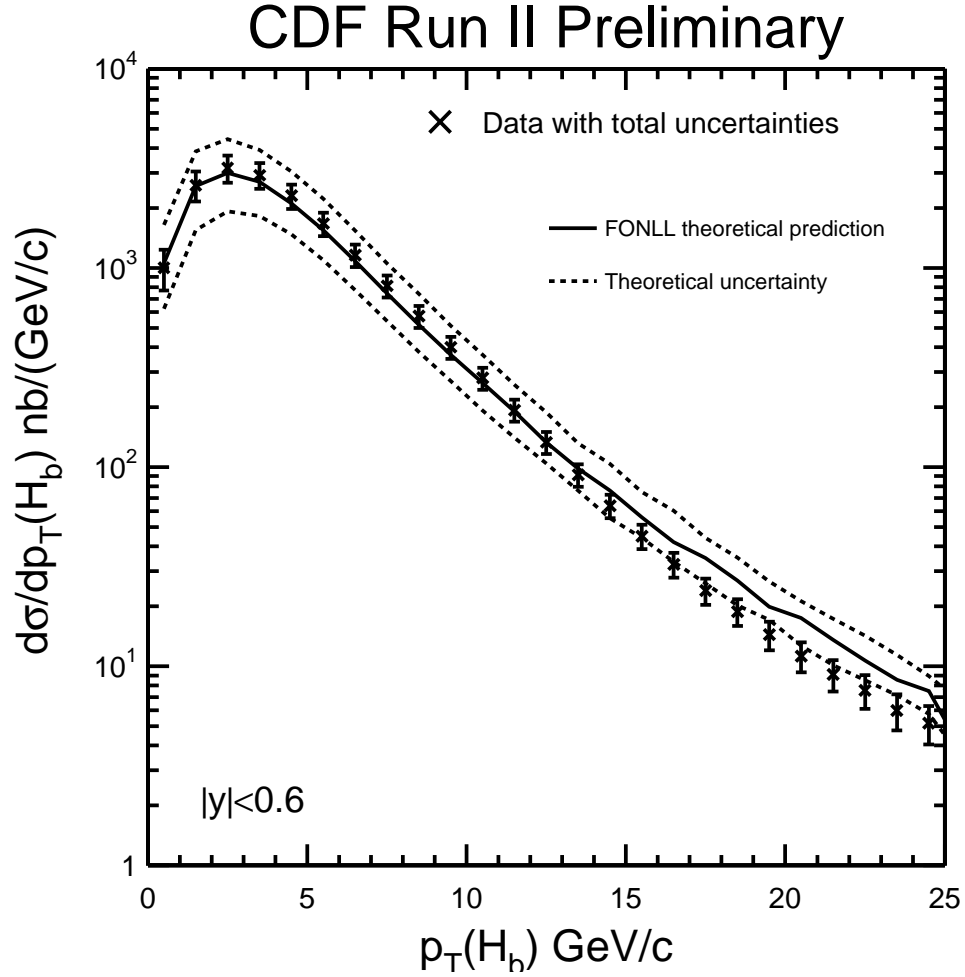
Chapter 7

Discussion

The inclusive J/ψ and b-hadron cross sections have been measured in $p\bar{p}$ interactions at $\sqrt{s} = 1960$ GeV in the central rapidity region of $|y| < 0.6$. The cross sections have been measured down to ~ 0 GeV/c transverse momentum ranges for the first time.

To compare with the CDF Run I measurements of the cross section at $\sqrt{s} = 1800$ GeV [41, 42], the cross section measurements in the range $p_T(J/\psi) > 5.0$ GeV/c and pseudo-rapidity $|\eta(J/\psi)| < 0.6$ is extracted from the measured cross section by this analysis. The extracted inclusive J/ψ cross section at $\sqrt{s} = 1960$ GeV is found to be

$$\sigma(p\bar{p} \rightarrow J/\psi X)_{1960} \cdot \mathrm{Br}(J/\psi \rightarrow \mu\mu)$$

$$= 16.3 \pm 0.1(\mathrm{stat})^{+1.4}_{-1.3}(\mathrm{syst})\mathrm{nb}, \tag{7.1}$$

while the CDF Run I measurement at $\sqrt{s} = 1800$ GeV was

$$\sigma(p\bar{p} \to J/\psi X)_{1800} \cdot \mathrm{Br}(J/\psi \to \mu\mu)$$

$$= 17.4 \pm 0.1(\mathrm{stat})^{+2.6}_{-2.8}(\mathrm{syst})\mathrm{nb}. \tag{7.2}$$

The cross section of J/ψ events from H_b decays with $p_T(J/\psi) > 5$ GeV/c and $|\eta(J/\psi)| < 0.6$ is found to be

$$\sigma(p\bar{p} \to H_b X)_{1960} \cdot \mathrm{Br}(H_b \to J/\psi X) \cdot \mathrm{Br}(J/\psi \to \mu\mu)$$

$$= 2.75 \pm 0.04(\mathrm{stat}) \pm 0.20(\mathrm{syst})\mathrm{nb}, \tag{7.3}$$

while equivalent Run I measurement [41, 42] was

$$\sigma(p\bar{p} \to H_b X)_{1800} \cdot \mathrm{Br}(H_b \to J/\psi X) \cdot \mathrm{Br}(J/\psi \to \mu\mu)$$

$$= 3.23 \pm 0.05(\mathrm{stat})^{+0.28}_{-0.31}(\mathrm{syst})\mathrm{nb}. \tag{7.4}$$

Since the center-of-mass energy is increased from 1.8 TeV to 1.96 TeV in Run II, the Run II J/ψ and b-hadron production cross section is expected to be higher than the cross section of Run I by approximately 10%. However, the Run I measurments and measurements of this analysis are consistent within measurement uncertainties. The ratio of the Run II to Run I differential b-hadron cross section measurements as a function of $p_T(J/\psi)$ is shown in Fig. 7.1. The ratios are allmost constant at around 0.86 for all transverse momentum range, and no difference between Run I and Run II in the shape of the cross section is observed.

In Fig. 7.2, the B^+ exclusive differential cross section previously measured by CDF Run I at $\sqrt{s} = 1800$ GeV in the range $|y| < 1.0$ [7], is shown with the cross section extracted from the measurement of this analysis of the inclusive b-hadron differential cross section at $\sqrt{s} = 1960$ GeV. For the purpose of this comparison, the measurement of b-hadron cross section of this analysis is multiplied by the fragmentation fraction of B^+ mesons, whcih is the result from LEP experiments is used [29]. In addition, b-hadron inclusive cross section of this analysis is scaled up by a factor of 1.67 to extend the measurement to $|y| < 1.0$, where the rapidity distribution is assumed to be uniform in the region $|y| < 1.0$. As shown in Fig. 7.2, good agreement is found between the extracted measurement of the b-hadron cross section of this analysis and the direct measurement of the B^+ cross section of CDF Run I.

In Fig. 6.5 and Fig. 6.7, the measurement is compared to a QCD calculation of the b-hadron cross section by Cacciari et al. [13]. This calculation, called FONLL, uses a Fixed-Order approach with a Next-to-Leading-Log resummation and a new technique to extract the b-hadron fragmentation function from LEP data [12, 13]. The comparisons show good agreement between the measurement of this analysis and the calculation, for all tranverse momentum ranges. The single b-hadron cross section from this FONLL calculation using the CTEQ6M parton distribution functions [47, 48, 48] is

$$\sigma^{\text{FONLL}}_{(|y|<0.6)} = 16.8^{+7.0}_{-5.0}\mu\text{b} \tag{7.5}$$

which is in good agreement with measurement of this analysis

$$\sigma(p\bar{p} \to \bar{b}X, |y| < 0.6) = 17.6 \pm 0.4(\text{stat})^{+2.5}_{-2.3}(\text{syst})\mu b. \qquad (7.6)$$

Also, this result is compared to the QCD calculation described in reference [27]. This calculation employs a factorization scheme where the mass of the quark is considered negligible and a different treatment of the b-hadron fragmentation function is used. The cross section calculation in [27] is repeated using $\sqrt{s} = 1960$ GeV/c and the MRST2001 parton distribution functions [49,50]. The central value of the calculated cross section integrated over the rapidity range $|y| < 0.6$ and $p_T(J/\psi) > 5.0$ GeV/c is

$$\sigma(p\bar{p} \to H_b X, |y| < 0.6) \cdot \text{Br}(H_b \to J/\psi X) \cdot \text{Br}(J/\psi \to \mu\mu) = 3.2\text{nb} \qquad (7.7)$$

which is in good agreement with result of this analysis

$$3.06 \pm 0.04(\text{stat}) \pm 0.22(\text{syst})\text{nb}. \qquad (7.8)$$
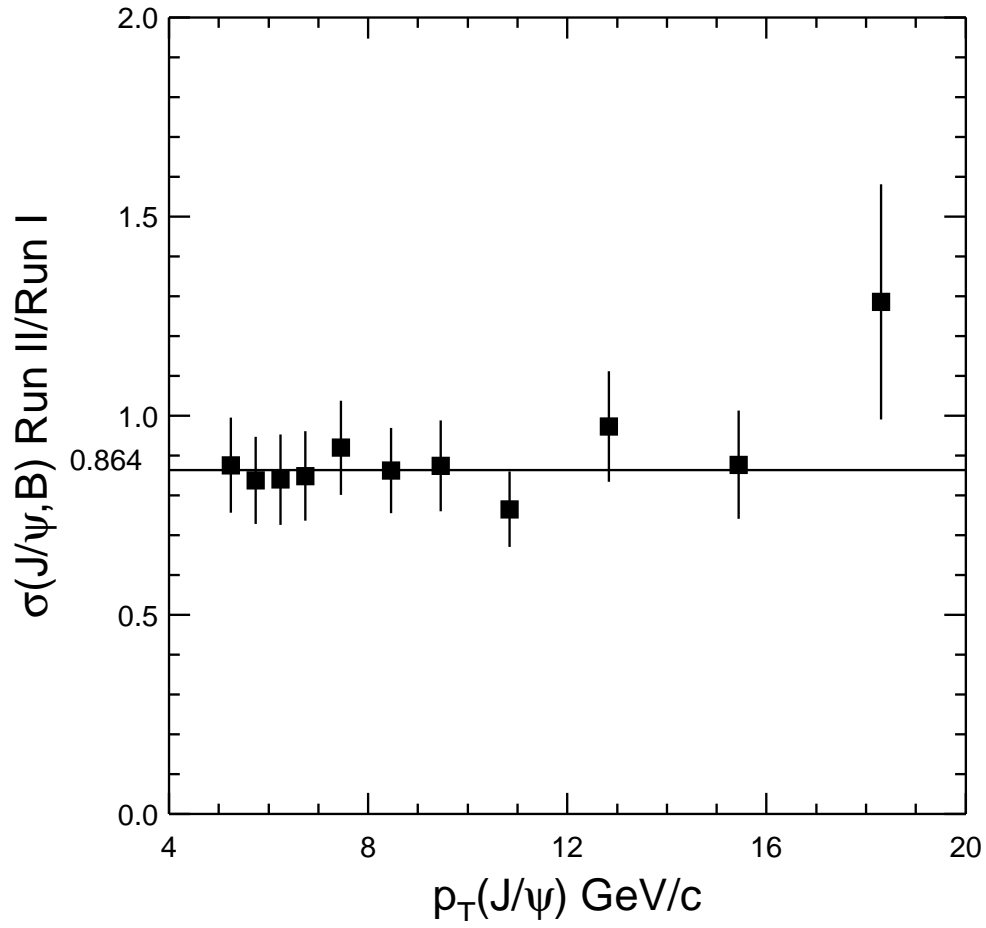
Figure 7.1: Ratio of the differential cross-section distributions of *J/ψ* events from the decays of *b*-hadrons as a function of *J/ψ* transverse momentum from CDF Run I and Run II.
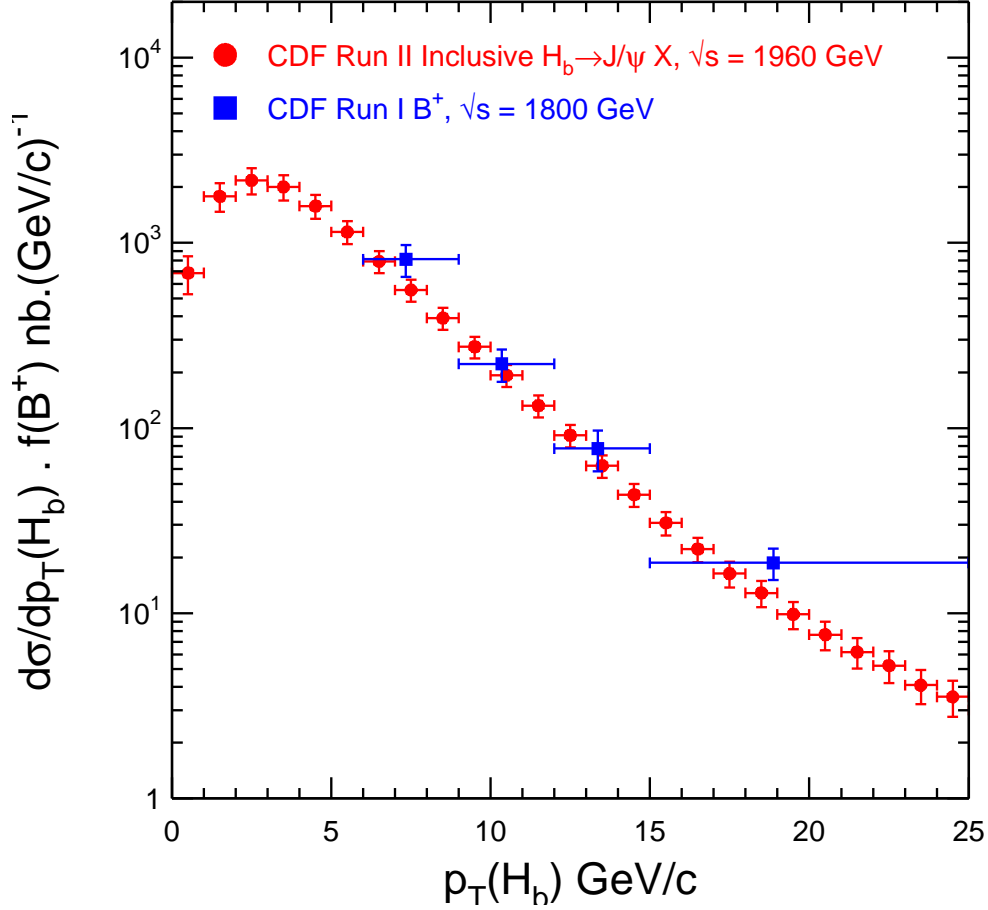
Figure 7.2: The differential cross-section distributions of *b*-hadrons as a function of *b*-hadron momentum from the measurement of the B^+ meson cross section in CDF Run I [7] and *b*-hadron inclusive cross section extracted in this analysis (Run II). For this comparison, the inclusive *b*-hadron cross section measured in Run II is multiplied by the expected fraction of B^+ mesons which is $f(B^+) = 40.96 \pm 0.81(stat) \pm 1.14(syst)\%$ [14]. The differential cross sections showed are integrated over the rapidity range $|y(H)_b| < 1.0$.

Chapter 8

Summary

In this analysis, the inclusive central J/ψ cross section has been measured in $p\bar{p}$ interactions at $\sqrt{s}$ = 1960 GeV in the range $|y| < 0.6$. The cross section has been measured over the full transverse momentum range for the first time. The integrated inclusive J/ψ cross section in the central rapidity range is found to be

$$\sigma[p\bar{p} \rightarrow J/\psi X, |y(J/\psi)| < 0.6]$$

$$= 4.08 \pm 0.02(\text{stat})^{+0.36}_{-0.33}(\text{syst})\mu\text{b}, \qquad (8.1)$$

after correcting for branching ratio Br($J/\psi \rightarrow \mu\mu$) = 5.88 ± 0.10% [29].

By utilizing the long lifetime of b-hadrons, the fraction of J/ψs which are decay products of b-hadrons has been estimated, and the cross section of b-hadron decays has been extracted from J/ψ cross section and the fraction for J/ψ transverse momenta range greater than 1.25 GeV/c. The integrated $H_b \rightarrow J/\psi X$

cross section, including both hadron and anti-hadron states, and correcting for the branching ratio $\text{Br}(J/\psi \to \mu\mu) = 5.88 \pm 0.10\%$ [29], is found to be

$$\sigma[p\bar{p} \to H_b, H_b \to J/\psi X, p_T(J/\psi) > 1.25\text{GeV}/c, |y(J/\psi)| < 0.6]$$

$$= 0.330 \pm 0.005(\text{stat})^{+0.036}_{-0.033}(\text{syst})\mu\text{b}. \tag{8.2}$$

J/ψs , from b-hadron decay which have transverse momenta greater than 1.25 GeV/c , include b-hadron transverse momenta down to zero. For the first time, the central b-hadron cross section as a function of b-hadron transverse momenta down to zero in $p\bar{p}$ collisions has been extracted. Comparion of the measured cross section to FONLL [13] calculation showed a good agreement for all b-hadron transverse momentum range. The total single b-hadron cross section integrated over all transverse momenta was found to be

$$\sigma[p\bar{p} \to H_b X, |y| < 0.6]$$

$$= 17.6 \pm 0.4(\text{stat})^{+2.5}_{-2.3}(\text{syst})\mu\text{b}, \tag{8.3}$$

which is in good agreement with FONLL [13] calculation. This agreement of this analysis to FONLL calculation solved long term problem, discrepancy between QCD calculation and measurements.

Bibliography

[1] CDF, F. Abe *et al.*, Phys. Rev. Lett. **71**, 500 (1993).

[2] CDF, F. Abe *et al.*, Phys. Rev. Lett. **71**, 2396 (1993).

[3] CDF, F. Abe *et al.*, Phys. Rev. Lett. **69**, 3704 (1992).

[4] P. Nason, S. Dawson, and R. K. Ellis, Nucl. Phys. **B327**, 49 (1989), Erratum-ibid.B335:260,1990.

[5] CDF, F. Abe *et al.*, Phys. Rev. Lett. **75**, 1451 (1995), hep-ex/9503013.

[6] M. L. Mangano, P. Nason, and G. Ridolfi, Nucl. Phys. **B373**, 295 (1992).

[7] CDF, D. Acosta *et al.*, Phys. Rev. **D65**, 052005 (2002), hep-ph/0111359.

[8] W. Beenakker, W. L. van Neerven, R. Meng, G. A. Schuler, and J. Smith, Nucl. Phys. **B351**, 507 (1991).

[9] A. D. Martin, W. J. Stirling, and R. G. Roberts, Phys. Lett. **B306**, 145 (1993).

[10] A. D. Martin, R. G. Roberts, W. J. Stirling, and R. S. Thorne, Eur. Phys. J. **C4**, 463 (1998), hep-ph/9803445.

[11] D0, B. Abbott *et al.*, Phys. Lett. **B487**, 264 (2000), hep-ex/9905024.

[12] M. Cacciari and P. Nason, Phys. Rev. Lett. **89**, 122003 (2002), hep-ph/0204025.

[13] M. Cacciari, S. Frixione, M. L. Mangano, P. Nason, and G. Ridolfi, JHEP **07**, 033 (2004), hep-ph/0312132.

[14] E. Ben-Haim, hep-ph **0310009** (2003).

[15] CDF, T. Affolder *et al.*, Phys. Rev. Lett. **85**, 2886 (2000), hep-ex/0004027.

[16] J. C. Collins, D. E. Soper, and G. Sterman, Nucl. Phys. **B263**, 37 (1986).

[17] UA1, C. Albajar *et al.*, Phys. Lett. **B186**, 237 (1987).

[18] UA1, C. Albajar *et al.*, Phys. Lett. **B256**, 121 (1991).

[19] P. Nason, S. Dawson, and R. K. Ellis, Nucl. Phys. **B303**, 607 (1988).

[20] CDF, F. Abe *et al.*, Phys. Rev. Lett. **68**, 3403 (1992).

[21] CDF, F. Abe *et al.*, Phys. Rev. **D50**, 4252 (1994).

[22] D0, S. Abachi *et al.*, Phys. Rev. Lett. **74**, 3548 (1995).

[23] D0, S. Abachi *et al.*, Phys. Lett. **B370**, 239 (1996).

[24] D0, B. Abbott *et al.*, Phys. Rev. Lett. **84**, 5478 (2000), hep-ex/9907029.

[25] D0, B. Abbott *et al.*, Phys. Rev. Lett. **85**, 5068 (2000), hep-ex/0008021.

[26] H. Jung, Phys. Rev. **D65**, 034015 (2002), hep-ph/0110034.

[27] B. A. Kniehl and G. Kramer, Phys. Rev. **D60**, 014006 (1999), hep-ph/9901348.

[28] E. L. Berger *et al.*, Phys. Rev. Lett. **86**, 4231 (2001), hep-ph/0012001.

[29] K. Hagiwara *et al.*, Phys. Rev. D **66** (2002).

[30] J. Cockcroft and E. Walton, Proc. Roy. Soc. , 136 (1932).

[31] J. Mariiner *et al.*, **See www document, http://www-bd.fnal.gov/lug/runII handbook/RunII index.html**.

[32] J. Elias *et al.*, Nucl. Instrum. Meth. **A441**, 366 (2000).

[33] CDF, D. Acosta *et al.*, Nucl. Instrum. Meth. **A461**, 540 (2001).

[34] D. Acosta *et al.*, Nucl. Instrum. Meth. **A494**, 57 (2002).

[35] Y. Gotra *et al.*, CDF internal Note **6162**.

[36] G. T. P. Avery, K. Read, 1985, CLEO Report No. CSN-212 1985, (unpublished).

[37] R. Brun *et al.*, CERN-DD-78-2-REV.

[38] C. Chen *et al.*, CDF internal note **6394** (2003).

[39] K. Bloome *et al.*, CDF internal Note **6017**.

[40] K. Bloome *et al.*, CDF internal Note **6347**.

[41] CDF, F. Abe *et al.*, Phys. Rev. Lett. **79**, 572 (1997).

[42] CDF, F. Abe *et al.*, Phys. Rev. Lett. **79**, 578 (1997).

[43] T. Daniels, Ph.D Thesis, Massachusetts Institute of Technology (1997), Ph.D Thesis.

[44] BABAR, B. Aubert *et al.*, Phys. Rev. **D67**, 032002 (2003), hep-ex/0207097.

[45] V. Krey and K. R. S. Balaji, Phys. Rev. **D67**, 054011 (2003), hep-ph/0209135.

[46] CLEO, S. Anderson *et al.*, Phys. Rev. Lett. **89**, 282001 (2002).

[47] J. Pumplin, D. R. Stump, and W. K. Tung, Phys. Rev. **D65**, 014011 (2002), hep-ph/0008191.

[48] D. Stump *et al.*, Phys. Rev. **D65**, 014012 (2002), hep-ph/0101051.

[49] A. D. Martin, R. G. Roberts, W. J. Stirling, and R. S. Thorne, Eur. Phys. J. **C23**, 73 (2002), hep-ph/0110215.

[50] A. D. Martin, R. G. Roberts, W. J. Stirling, and R. S. Thorne, Eur. Phys. J. **C35**, 325 (2004), hep-ph/0308087.